Ore Geology Reviews 195 (2026) 107405

Contents lists available at ScienceDirect

Ore Geology Reviews

journal homepage: www.elsevier.com/locate/oregeorev

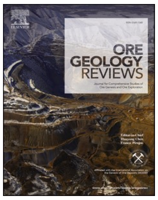

Progressive mantle melting and crust–mantle–fluid hybridization in fluorite-bearing Sn–Nb ± Mo-rich alkaline granites of the Jos Plateau, central Nigeria

Vandi Dlama Kamaunji [a], Hafizullah Abba Ahmed [b], Lian-Xun Wang [a,*], Ioan V. Sanislav [c], Musa Bala Girei [d], Yu-Xiang Zhu [a], Xin-xin Liang [a], Xin Chen [e], Mabrouk Sami [f,**]

[a] *State Key Laboratory of Geological Processes and Mineral Resources, School of Earth Sciences, China University of Geosciences, Wuhan 430074, PR China*
[b] *School of Physical Sciences, Department of Geology, Modibbo Adama University, Yola, P.M.B 2076, Yola, Adamawa State, Nigeria*
[c] *College of Science and Engineering, James Cook University, Economic Geology, Townsville, QLD 4811, Australia*
[d] *Department of Geology, Faculty of Earth and Environmental Sciences, Bayero University Kano, PMB 3011, Kano State, Nigeria*
[e] *State Key Laboratory of Geological Processes and Mineral Resources, School of Earth Resources, China University of Geosciences, Wuhan 430074, PR China*
[f] *Geosciences Department, College of Science, United Arab Emirates University, 15551 Al Ain, United Arab Emirates*

ARTICLE INFO

Keywords:
Crust-mantle-fluid hybridization
Within-plate alkaline granites
Sn-Nb-Mo mineralization
Jos-Plateau Tin Belt

ABSTRACT

Alkaline granites of the Jos Plateau Tin Belt (central Nigeria) host Sn-Nb-Mo mineralization. However, their petrogenesis, metal enrichment, and tectono-geodynamic evolution remain poorly constrained. This study integrates whole-rock geochemistry and Sr-Nd isotopes, amphibole-fluorite chemistry, and zircon U-Pb geochronology from the Buji, Jos-Bukuru (JBK), and Kigom (KGM) complexes. Zircon U-Pb ages reveal a north-to-south younging trend from Buji (~179 Ma) through JBK (~168 Ma) to KGM (~166 Ma). Buji barren granites exhibit the most negative ε_{Nd}(t) (–4.4 to –4.2), least radiogenic ^{87}Sr/^{86}Sr$_{(i)}$ (0.7065–0.7066), and highest Neodymium Crustal Index (NCI = 0.31), indicating an enriched mantle source with strong crustal input. JBK Sn–Nb biotite-amphibole granites show intermediate ε_{Nd}(t) (–3.3 to –3.0), NCI (0.25), and moderately radiogenic ^{87}Sr/^{86}Sr$_{(i)}$ (0.7066–0.7173), suggesting an enriched mantle source with moderate crustal input and selective hydrothermal overprint. KGM Mo–Nb arfvedsonite–riebeckite granites exhibit near-chondritic ε_{Nd}(t) (–1.1 to –0.4), lowest NCI (0.25), and most radiogenic ^{87}Sr/^{86}Sr(i)r (0.7139–0.7206), reflecting extreme fluid-mediated metasomatism on a mantle-dominated magma. Decoupled fO_2 distinguishes oxidized JBK Ca-amphiboles from reduced KGM Na-amphiboles hosting oxidized zircons. Mass balance modeling indicates ~40–50 vol% feldspar-dominated fractional crystallization coupled with ~30–40 vol% upper crustal assimilation. JBK granites show Sn-Nb enrichment (4–126 ppm; 37–910 ppm), while KGM granites exhibit high Nb with extreme Zn-Pb-Cu (≤1326, 1054, 845 ppm), consistent with Mo-enriched systems. Fluorite compositions (F = 52–56 wt%) record F-rich reducing fluids that promoted HFSE-REE-Sn-Nb-Mo mobility. A four-stage model explains Sn-Nb-Mo enrichment in JBK and KGM: (I) magmatic enrichment; (II) magmatic-hydrothermal transition; (III) hydrothermal veining and stockworks formation; (IV) supergene placer formation. Transtension triggered adiabatic melting of metasomatized mantle, generating alkaline magmas that ascended along shear zones to form shallowly emplaced (2.6–8.7 km) anorogenic alkaline complexes. Fertile global analogues share this convergence of transtensional shearing, crustal assimilation, and F-rich fluid flux.

1. Introduction

Anorogenic alkaline granites are important expressions of within-plate magmatism. They are increasingly recognized for their potential to host economically significant concentrations of high field strength elements (HFSEs; e.g., Nb, Zr, Ta) and rare (base) metals such as tin (Sn) and molybdenum (Mo) (Vasyukova and Williams-Jones, 2020; Beard et al., 2023). These granites typically exhibit high alkalis, fluorine,

---

* Corresponding author.
** Corresponding author at: Geosciences Department, College of Science, United Arab Emirates University, 15551 Al Ain, United Arab Emirates.
E-mail addresses: lianxunwang@cug.edu.cn (L.-X. Wang), mabrouksami@uaeu.ac.ae (M. Sami).

https://doi.org/10.1016/j.oregeorev.2026.107405
Received 18 July 2025; Received in revised form 13 June 2026; Accepted 19 June 2026

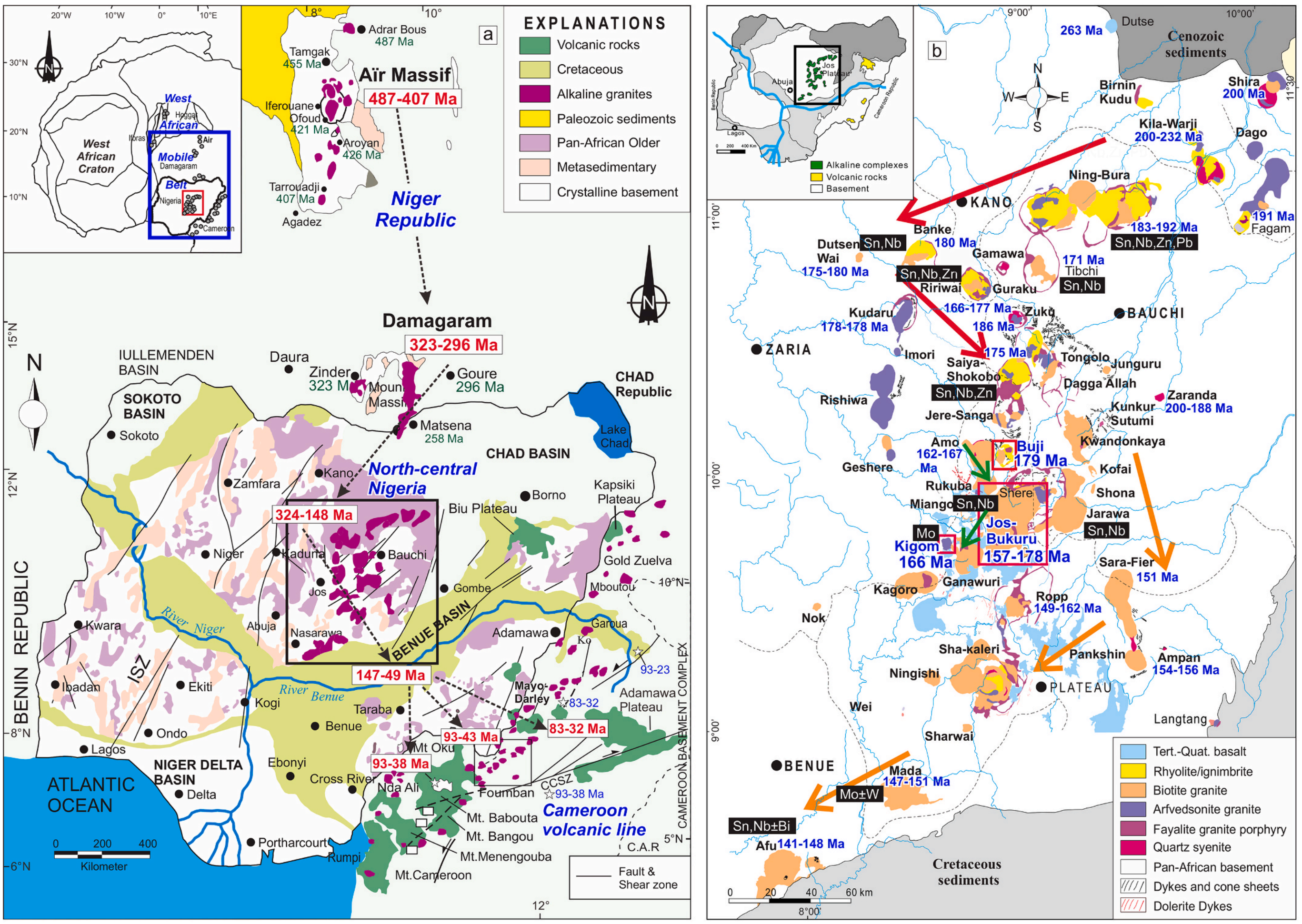

Fig. 1. (a). Geological map of Niger-Nigeria and Cameroun Younger Granite Province showing the age migration and distribution of Phanerozoic anorogenic ring complexes (Modified after Ngako et al., 2006). C.A.R.: Central African Republic; CCSZ: Central Cameroon Shear Zone.. Ages of Aïr and Damagaram in Niger Republic are based on Rb-Sr dating by Bowden et al., (1976). (b) Geological map of the Nigerian Younger Granite Province (after Kinnaird, 1981, 1985) showing the north-to-south age progression of alkaline ring complexes, with the location of the studied Buji, Jos-Bukuru, and Kigom complexes marked in the central Jos-Plateau Tin Belt. Arrows indicate the ENE-WSW migration direction of Mesozoic magmatic centers based on Rb-Sr isochron trends (Rahaman et al., 1984; Van Breemen et al., 1975; Dickin et al., 1991) and U–Pb zircon ages from this study are other recent works (Table 6). Red arrows indicate early peralkaline granitic suites in the northern sector based on previous studies, green arrows indicate the later-stage metaluminous to peraluminous granitic complexes in the central Jos Plateau (this study), and orange arrows indicate the southern weakly peraluminous biotite granites.

HFSE, and rare earth elements (REEs) as well as low CaO and MgO, and are commonly associated with A-type geochemical signatures (Loiselle and Wones, 1979; Eby, 1992; Dall'Agnol et al., 2012). While the economic importance of these granites is well established (Dostal, 2016), the processes controlling Sn, Nb, and Mo enrichment, including, including magma sources, crustal assimilation, redox evolution, and volatile complexing, remain complex and insufficiently understood (Siegel et al., 2018; Vasyukova and Williams-Jones, 2020; Vonopartis et al., 2021; Beard et al., 2023).

The Nigerian Younger Granite Province (NYGP), part of the West African Mobile Belt (Fig. 1a), is a classic example of within-plate alkaline magmatism. It comprises fifty-three Paleozoic–Mesozoic (ca. 324–141 Ma) silica-oversaturated syenite–granite ring complexes emplaced into the Pan-African basement of central Nigeria (Fig. 1b). The province hosts widespread Sn–Nb–Mo mineralization in both alluvial and primary forms. Primary mineralization occurs as greisen, stockwork, and disseminations (MacLeod et al., 1971; Kinnaird, 1985). Despite these deposits, the spatiotemporal evolution of magma sources, fluid regimes, redox conditions, and hybridization controlling metal enrichment remain incompletely understood. The Jos Plateau Tin Belt, characterized by highly mineralized, fluorine-rich granites, provides an ideal natural laboratory to investigate these processes. However, its petrological diversity, zoned metal distribution, and complex tectonomagmatic evolution require an integrated, multi-proxy research approach. Recent studies highlight the importance of mantle–crust interaction and fluid-driven metasomatism (Girei et al., 2020; Kamaunji et al., 2023). However, the nature of their magma source and mechanisms responsible for Sn, Nb, and Mo enrichment within this belt remain insufficiently understood. This study investigates three ring complexes in the Jos Plateau Tin Belt, the Buji, Jos-Bukuru (JBK), and Kigom (KGM) complexes, which show a southward-younging trend and progressive geochemical evolution. The Buji complex is dominated by barren biotite–arfvedsonite granite. In contrast, the JBK contains Sn–Nb-bearing, fluorite-rich biotite–amphibole granites, whereas KGM host Mo–Sn–Nb-enriched arfvedsonite–riebeckite granites. These complexes record increasing crustal assimilation and late-stage fluid interaction. Thus, they provide a natural laboratory to investigate how hybrid mantle-derived melts evolved through Rb-F-rich crustal inputs, and how redox and volatile conditions control rare-metal fertility. We integrate zircon U–Pb geochronology, amphibole/fluorite chemistry, whole-rock geochemistry, and Sr–Nd isotopes to: (1) constrain emplacement timing and magma sources; (2) quantify hybridization and fluid effects; and (3) assess controls on Sn–Nb–Mo enrichment. The results indicate that F-rich fluids prolonged melt evolution and enhanced metal

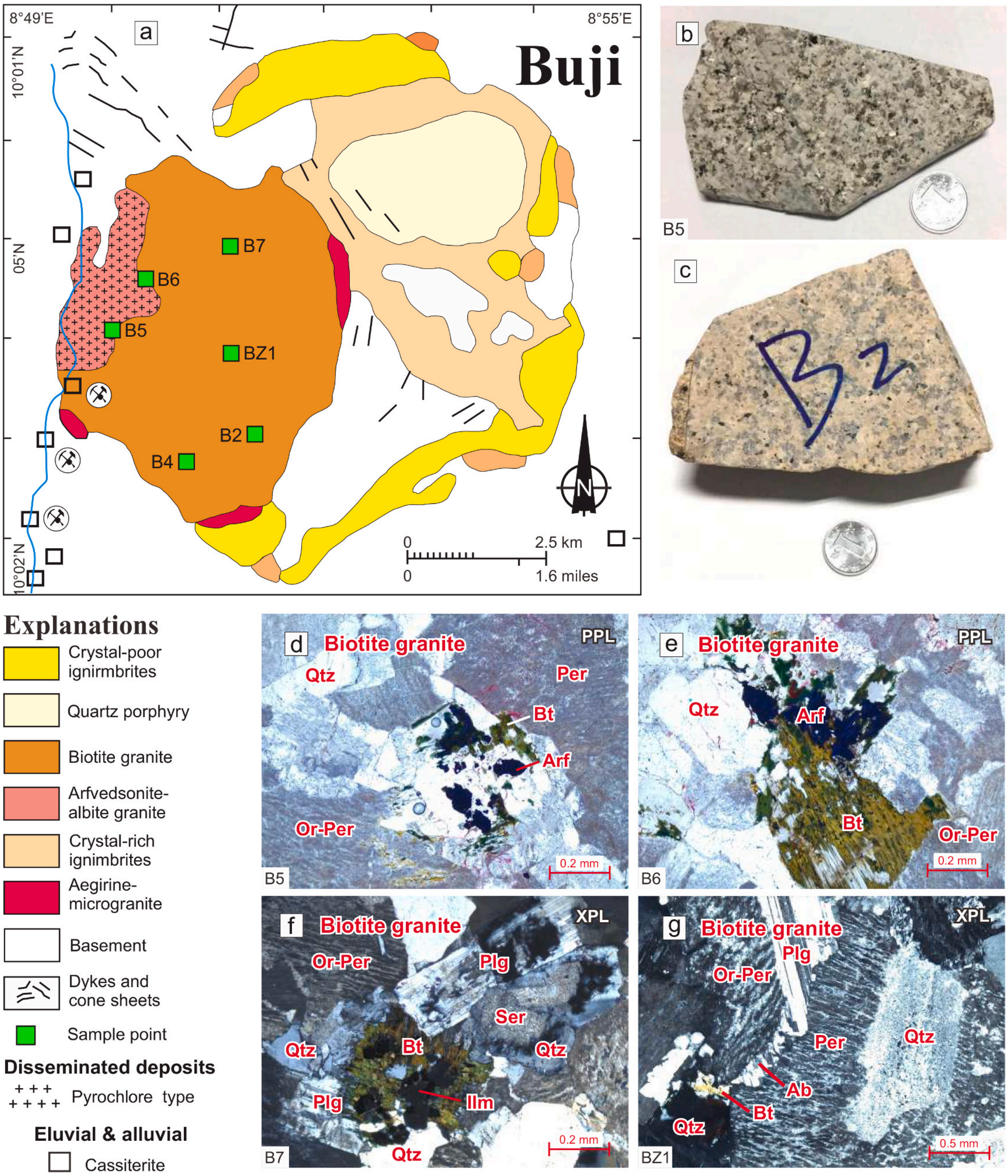

Fig. 2. (a) Geological map of Buji complex (extracted from Kinnaird, 1981), (b–c) Hand specimen of biotite granites from Buji complex, (d–g) Photomicrographs of biotite granites from the Buji complex. Fig. 2d is PPL; Figs. 2f–g are XPL. Bt = biotite; Qtz = quartz, Plg = plagioclase; Or = orthoclase; Or = orthoclase; Per = perthite; Arf = arfvedsonite; Ilm = ilmenite; Ser = sericite; Ab = albite.

transport. Furthermore, crust–mantle–fluid hybridization and polybaric differentiation controlled the transition from barren to mineralized systems. These findings define critical thresholds for rare-metal mineralization in intraplate alkaline settings.

2. Regional geological background and sample description

2.1. Nigerian alkaline province

The Nigerian alkaline province, part of the broader Niger–Nigeria alkaline province, comprises three sub-provinces—Aïr, Damagaram, and north-central Nigeria—hosting over 80 north–south age migrating Paleozoic–Mesozoic silica-oversaturated complexes (ca. 487–141 Ma) (Bowden et al., 1976, 1987) (Fig. 1a). The Nigerian sector contains 53 age-progressive syenite–granite ring complexes (ca. 324–148 Ma; Rahaman et al., 1984; Vincent et al., 2022b; Cao et al., 2024) distributed over a 400 × 160 km zone (Kinnaird, 1981) (Fig. 1b). This progression extends into the Benue sub-basin (ca. 141–49 Ma) and culminates in Cretaceous–Neogene magmatism (ca. 93–23 Ma) along the Cameroon volcanic line (Kinnaird and Bowden, 1987; Ngako et al., 2006) (Fig. 1b). The regional distribution of ring centers across Nigeria, Algeria, Mali, and Niger reflects reactivation of Pan-African basement structures, including N–S thrusts and NW–SE sinistral faults with subsidiary NE–SW dextral faults (Liégeois et al., 1994). In Nigeria, N–S, NNW–SSE, and ENE–WSW trending shear zones and deep transcurrent faults localized magmatism during late Pan-African deformation (Rahaman et al., 1984; Black et al., 1985).

Alkaline ring complexes in the NYGP intrude central and eastern Nigerian Pan-African basement rocks—migmatite-gneisses, metapelites, and granitoids (Ferré et al., 1998; Kamaunji et al., 2022b). The NYGP is

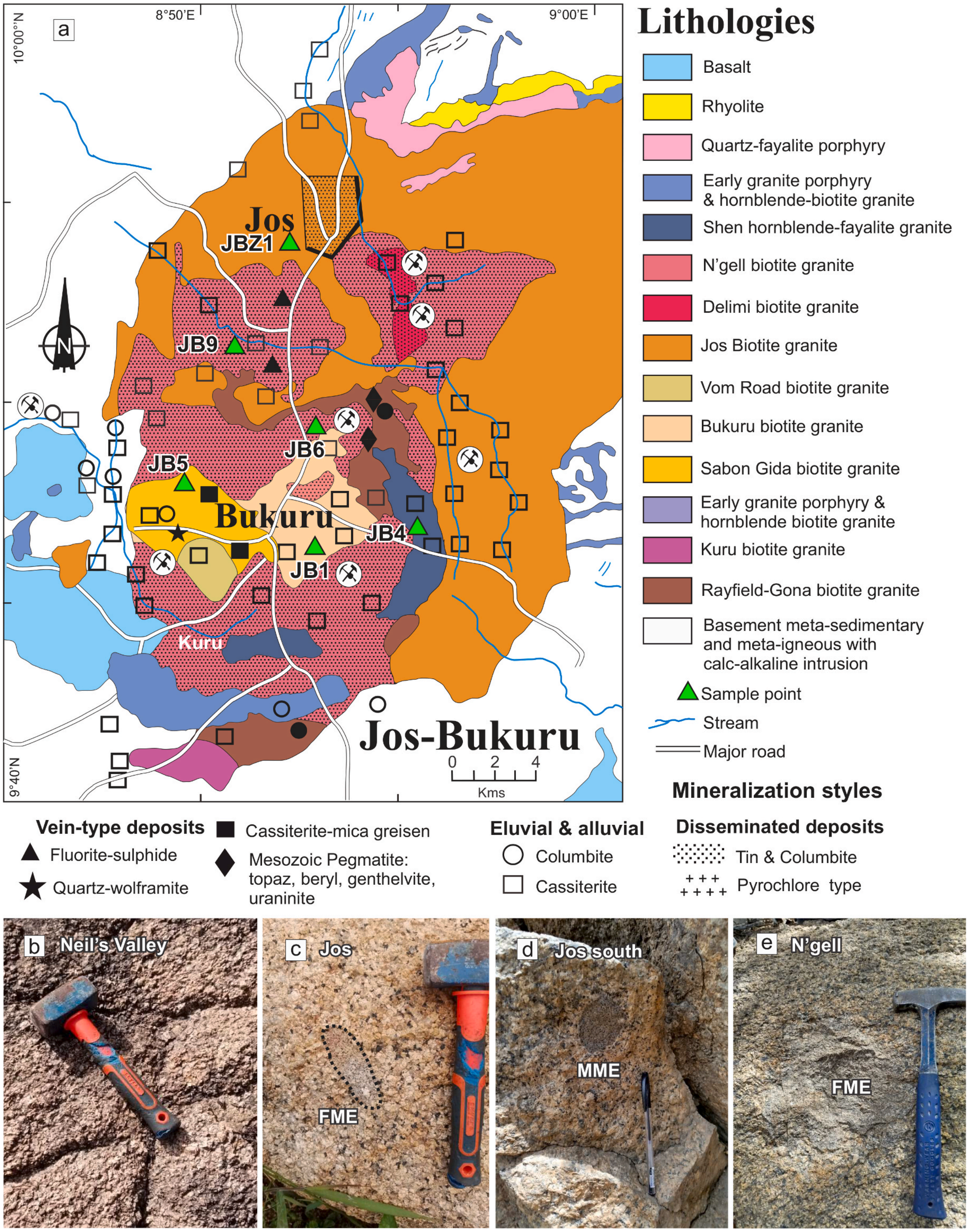

Fig. 3. (a) Geological map of the Jos-Bukuru Complex (modified after Kinnaird, 1981). (b–e) Field photographs of: (b) Neil's Valley granite porphyry, (c) Jos biotite-hornblende granite with felsic microgranular enclaves (FME), (d) Jos South hornblende-biotite granite hosting mafic microgranular enclaves (MME), and (e) N'gell biotite granite containing FME.

predominantly felsic, with granites-rhyolites making up ~90% of exposures (MacLeod et al., 1971). Mafic and intermediate rocks (<1% total) are more prominent in syenite-rich complexes (e.g., Shira, Kila-Warji, Zuku, and Zaranda, Fig. 1b). Magmatic activity began with rhyolite–ignimbrite eruptions and extrusion of mafic to intermediate lavas (Kinnaird and Bowden, 1987), followed by caldera collapse and the emplacement of syenitic and granitic porphyries (Turner, 1968). Fayalite–hedenbergite granite porphyries, often the oldest (except in syenitic centers), were succeeded by pyrochlore-bearing peralkaline arfvedsonite–albite granites and later weakly peraluminous biotite–hastingsite–hornblende granites, which form large plutons, in the Jos-Plateau (Bowden and Kinnaird, 1984; Bowden et al., 1987). These granites experienced prolonged cooling and multi-stage hydrothermal alteration, resulting in cassiterite, columbite, molybdenite, wolframite, and minor Pb–Zn–Cu sulfide mineralization (Kinnaird, 1985). Primary Sn ± Nb±(Mo, Zn, Cu, Pb) lodes occur in Ririwai, Tibchi, and Kigom

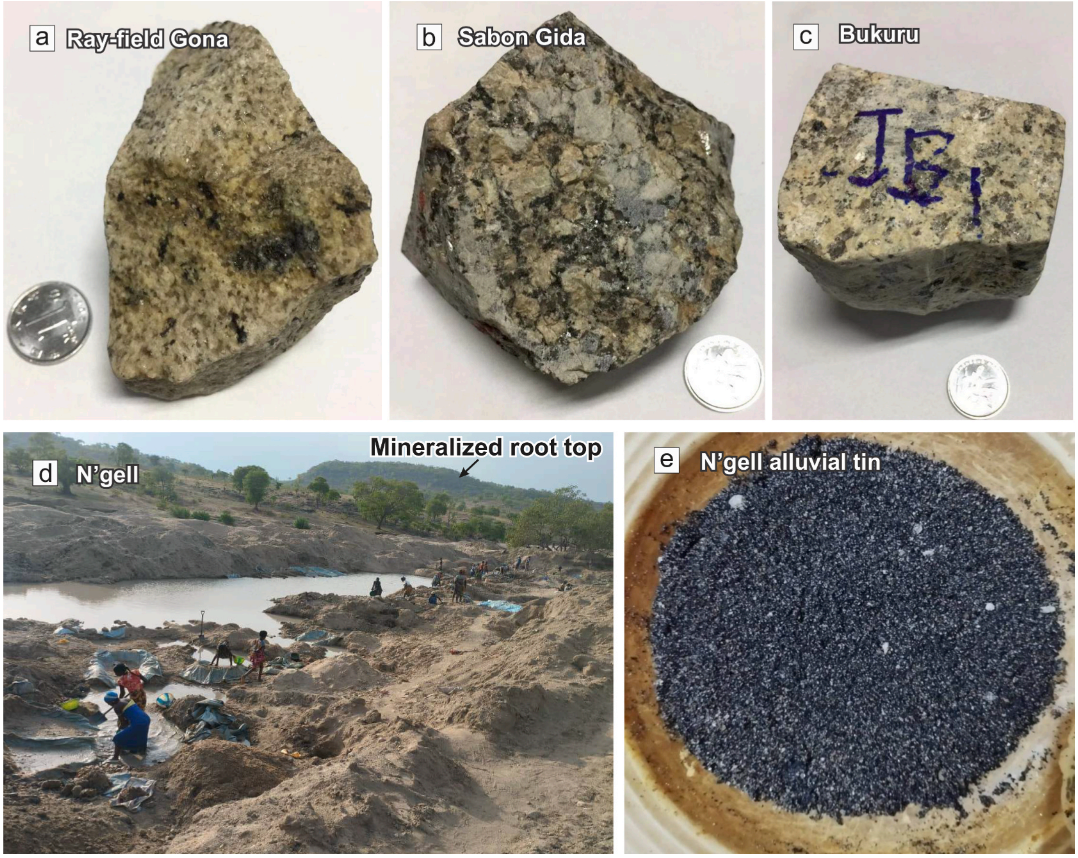

Fig. 4. (a-c) Hand specimen photographs of: (a) Rayfield hornblende-biotite granite, (b) Sabon Gida biotite granite, and (c) Bukuru biotite granite. (d) Field photograph of alluvial tin-columbite mining operations in N'gell, Jos-Bukuru Complex, showing the mineralized biotite granite pluton (foreground) with weathered roof zones that sourced the detrital tin and columbite now concentrated in adjacent river channels. (e) Recovered columbite concentrates from the N'gell alluvial site.

(Kinnaird et al., 2016), with subsequent erosion concentrating rare-metal ores in alluvial placers across the Jos-Plateau Tin Belt.

2.2. Buji complex: geology and petrography

The Buji Complex (~78 km^2), located adjacent to the Jos Plateau (Fig. 1b), forms a 10-km-wide quasi-circular structure (Fig. 2a) that records a complete magmatic evolution from early volcanism to final plutonism. Initial activity involved eruptions of rhyolites, tuffs, and agglomerates, followed by basic dykes and quartz–hedenbergite porphyries (Buchannan et al., 1971). This sequence is expressed as two ring structures: an older, volcanic-dominated eastern ring and a younger, granitic western ring (Fig. 2a). Plutonism progressed from early acid cone sheets to the emplacement of the major 8.1-km-wide Buji biotite granite, preceded by an aegirine–microgranite ring dyke that marks a phase of cauldron subsidence. The terminal intrusive phase was the arfvedsonite–albite granite.

The Buji biotite-arfvedsonite granite is whitish–gray, medium-grained, and composed of interlocking quartz, feldspar, and biotite (Fig. 2b, c). Thin sections reveal chloritized biotite associated with arfvedsonite, a groundmass of quartz, and perthitic orthoclase (Fig. 2d, e). It also contains dominant perthitic orthoclase with albite-twinned plagioclase, sericitized feldspar, quartz, and biotite with opaque inclusions (Fig. 2f). Large, cloudy perthitic orthoclase aggregates with albite lamellae, quartz inclusions, and minor albite rims and chloritized biotite are also present (Fig. 2g). This complex is petrogenetically distinct as a barren body. Its amphibole assemblage is dominantly sodic (arfvedsonite), and it is notably devoid of accessory fluorite, contrasting sharply with the mineralized complexes that follow.

2.3. Jos-Bukuru complex (JBK): geology and petrography

The JBK Complex (~430 km^2, Fig. 3a), centrally located within NYGP (Fig. 1b), is the largest and most mineralogically significant intrusive body, hosting Nigeria's richest Sn–Nb alluvial deposits (Buchannan et al., 1971). Bounded by ring fractures, the complex is characterized by a multi-stage evolution, beginning with extrusive rhyolitic lavas, pyroclastics, and felsite dykes of Neil's Valley (up to 0.9 km thick) (Buchannan et al., 1971). This is followed by two granite cycles followed: (1) an early phase with Neil's Valley granite-porphyry, Vom hornblende–biotite granite, and the extensive Jos biotite granite (~285 km^2) and N'gell granite, with localized Nb-bearing pegmatites in Kuru Stock; and (2) the central cycle with Shen hornblende–fayalite granite and Bukuru biotite granite (~23 km^2), a key Sn host. Terminal stages are marked by highly evolved, greisenized Sabon Gida granites. The granites exhibit varied textures. Neil's Valley porphyry is highly jointed, with visible feldspar phenocrysts (Fig. 3b). The Jos granite is pinkish, medium-grained, and contains hornblende with felsic enclaves (Fig. 3c), while its southern counterpart shows elongated hornblende and mafic enclaves (Fig. 3d). The N'gell granite is grayish with diffuse felsic enclaves (Fig. 3e). The Rayfield-Gona biotite granite has a grayish-green, sugary texture with greenish biotite (Fig. 4a), whereas the Sabon Gida granite is coarse-grained with chloritized biotite (Fig. 4b). The Bukuru granites are medium-grained with dark biotite and quartzofeldspathic aggregates (Fig. 4c).

Unlike the conspicuous tin mineralization in the Sn-bearing alkaline granites of Cameroon (Lavenir et al., 2023), the Sn–Nb mineralization at JBK is predominantly cryptic. This mineralization occurs primarily as microscopic inclusions within biotite, similar to occurrences reported in the Afu complex (Imeokparia, 1981). While primary lodes are rare in

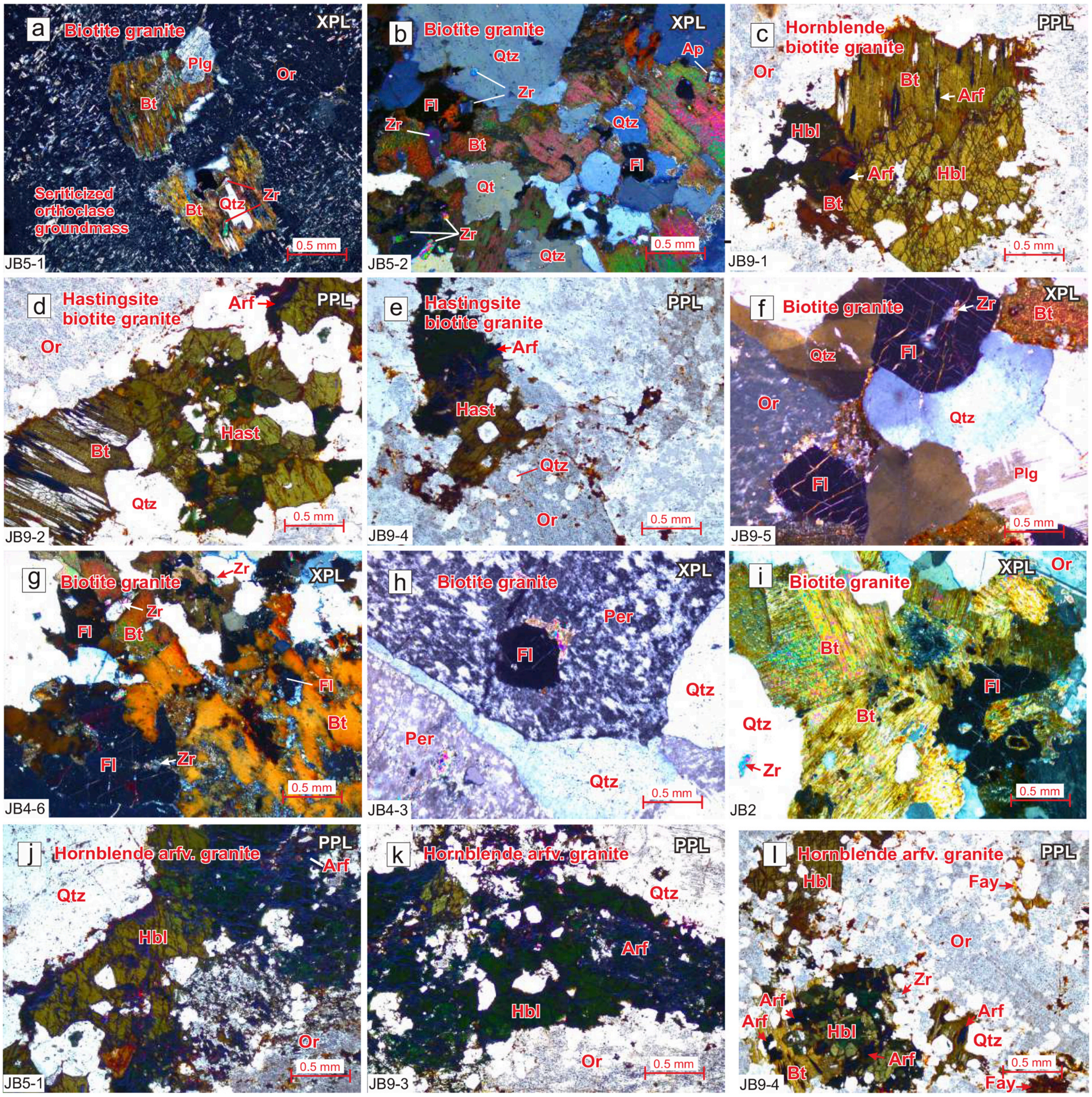

Fig. 5. (a–l) Photomicrographs of biotite granites from Jos-Bukuru complex. Figs. 5c-e and 5j-l are PPL; the remaining photomicrographs are XPL. Bt = biotite; Hbl = hornblende; Hast = hastingsite; Arf = arfvedsonite; Qtz = quartz, Fl = fluorite; Plg = plagioclase; Or = orthoclase; Ap = apatite; Zr = zircon.

JBK, Rayfield-Gona granite hosts high-grade cryptic tin and columbite zones (~50 acres), with >700 tons historically produced and >15,000 metric tons in reserves from 150 to 200 ft weathered profiles, yielding 2–7 lb/ton (avg. 2–3 lb/ton) (Buchannan et al., 1971). Sn–W mineralization occurs in greisenized N'gell and Sabon Gida granites, controlled by fractures and hydrothermal alteration. The N'gell and Sabon Gida granites are the most intensely greisenized phases in the complex, hosting narrow, fracture-controlled lodes where wolfram accompanies cassiterite. Beyond these greisen zones, the same granites contain finely disseminated cassiterite distributed throughout the rock mass, recoverable by panning even in areas lacking visible greisen alteration. Cassiterite–columbite occurs cryptically as fine particles in chloritized biotite, or migrates downward in weathered zones, forming dispersed secondary placer concentrations in surrounding drainages and river channels (Fig. 4d, f). This finely dispersed tin, though subeconomic in situ, has been extensively redistributed by supergene processes: detrital cassiterite migrates downward along joint planes in decomposed granite (documented to depths of 18 ft) and is further concentrated into rich alluvial placer deposits within the N'gell, Delimi, Bukuru, Shen, and Forum drainage systems. The bulk of alluvial cassiterite is derived specifically from the later granites (N'gell, Rayfield-Gona, and Sabon Gida), with the Rayfield-Gona phase additionally hosting disseminated columbite in albitized, decomposed zones. In thin section, chloritized biotite enclosing zircons, plagioclase, quartz, and opaque minerals are embedded in a sericitized orthoclase groundmass (Fig. 5a). The slide shows biotite sheets, greenish hornblende, and arfvedsonite inclusions, with quartz-rich orthoclase groundmass (Fig. 5b–e). Fluorite, sometimes containing zircon inclusions, occurs interstitially with biotite and quartz, occasionally with chlorite rims (Fig. 5f–i). The groundmass shows a porphyritic texture with large hornblende and hastingsite crystals enclosing arfvedsonite (Fig. 5j–l).

2.4. *Kigom complex (KGM): geology and petrography*

The KGM Complex, located ~26 km southwest of JBK (Fig. 2b), forms a ~36 km^2 circular intrusion (Imeokparia, 1984; Omada, 2000;

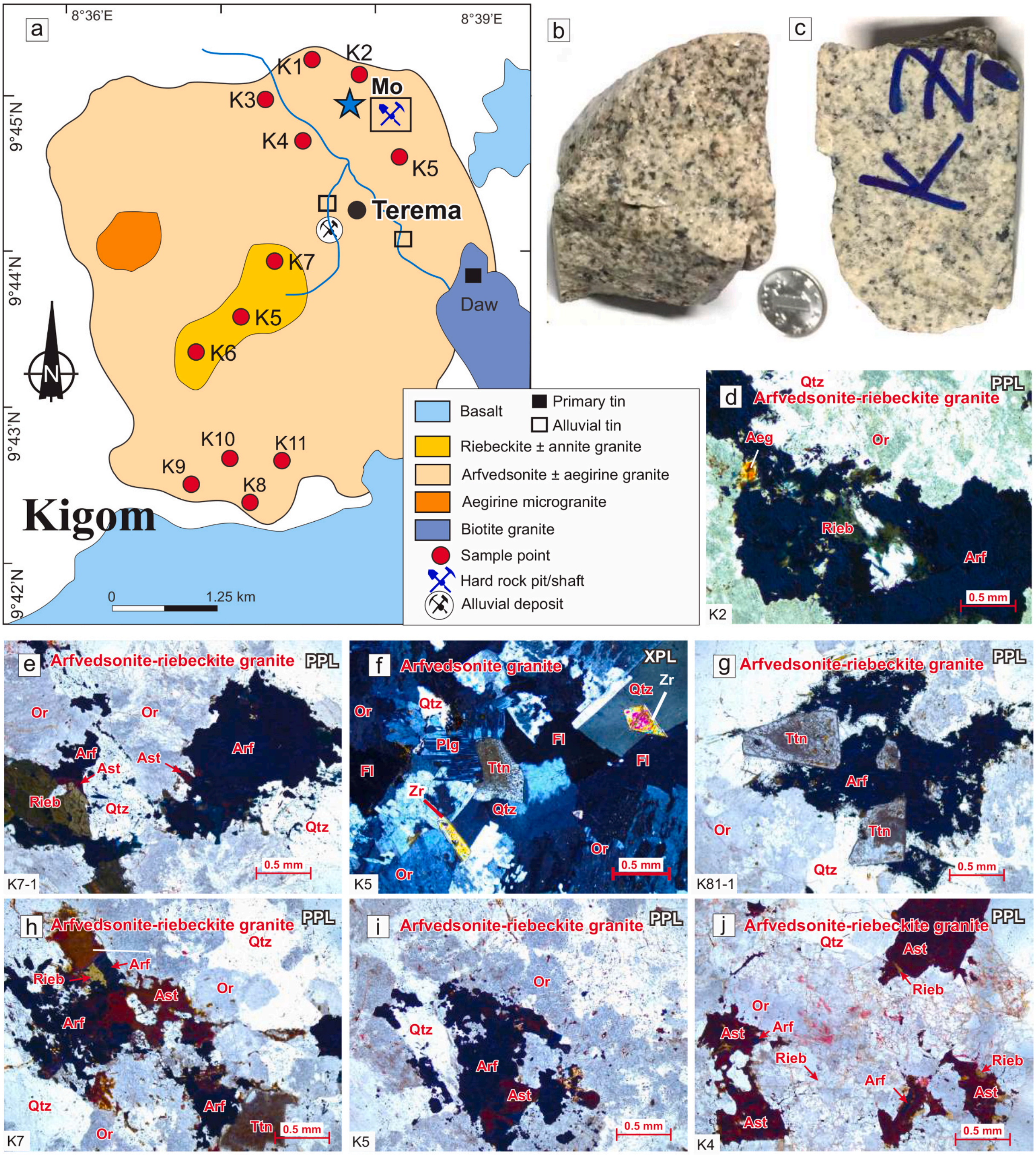

Fig. 6. (a) Geological map of Kigom complex (Extracted from Kinnaird, 1981), (b–c) Hand specimen samples of Kigom arfvedsonite-riebeckite granite, (d–j) Photomicrographs of Kigom arfvedsonite-riebeckite granite. Fig. 6f is XPL; the remaining photomicrographs are PPL. Qtz = quartz; Arf = arfvedsonite; Rieb = riebeckite; Ttn = titanite; Zr = zircon; Fe-Ti oxide = iron–titanium oxide; Aeg = aegirine; Or = orthoclase.

Fig. 6a). The earliest arfvedsonite granite occurs as a 3.2 km-long roof pendant within the dominant riebeckite granite (Buchannan et al., 1971; Omada, 2000; Omada et al., 2003), defining the complex's ring structure. Three textural variants are distinguished by arfvedsonite-riebeckite crystal habits. Contacts are leucocratic and equigranular (Fig. 6b–c). The cycle concludes with aegirine microgranite intruding the western hills, flooring a depression with scree-obscured contacts (Buchannan et al., 1971; Fig. 6a). The tin-bearing Daw granite (Ganawuri Complex) intrudes KGM's eastern margin near Terena (Fig. 6a). Thin sections document a peralkaline evolution: arfvedsonite precedes magmatic aegirine (Fig. 6d–e) and zircon in quartz/orthoclase; riebeckite → arfvedsonite replacement with astrophyllite borders (Fig. 6d); late fluorite + titanite with prismatic zircon (Fig. 6f) and arfvedsonite-titanite co-crystallization (Fig. 6g); subsolidus arfvedsonite-astrophyllite clusters (Fig. 6h–i); and final astrophyllite-dominated groundmass with riebeckite rims (Fig. 6j).

The KGM Hills contains minor sub-economic pyrochlore in riebeckite granite (Buchannan et al., 1971; Imeokparia, 1984; Omada et al., 2003). Mineralization manifests in three principal types: (1) silver-rich galena veins (>200 oz Ag/ton) in northern greisen (Omada et al., 2003), that follow an aplite dyke of Younger Granite origin, pinching and swelling to a maximum width of 8 in. over at least 70 yd in strike length; (2) molybdenite deposits at the granite's northern margin within poikilitic riebeckite facies (Omada, 2000). The molybdenum mineralization

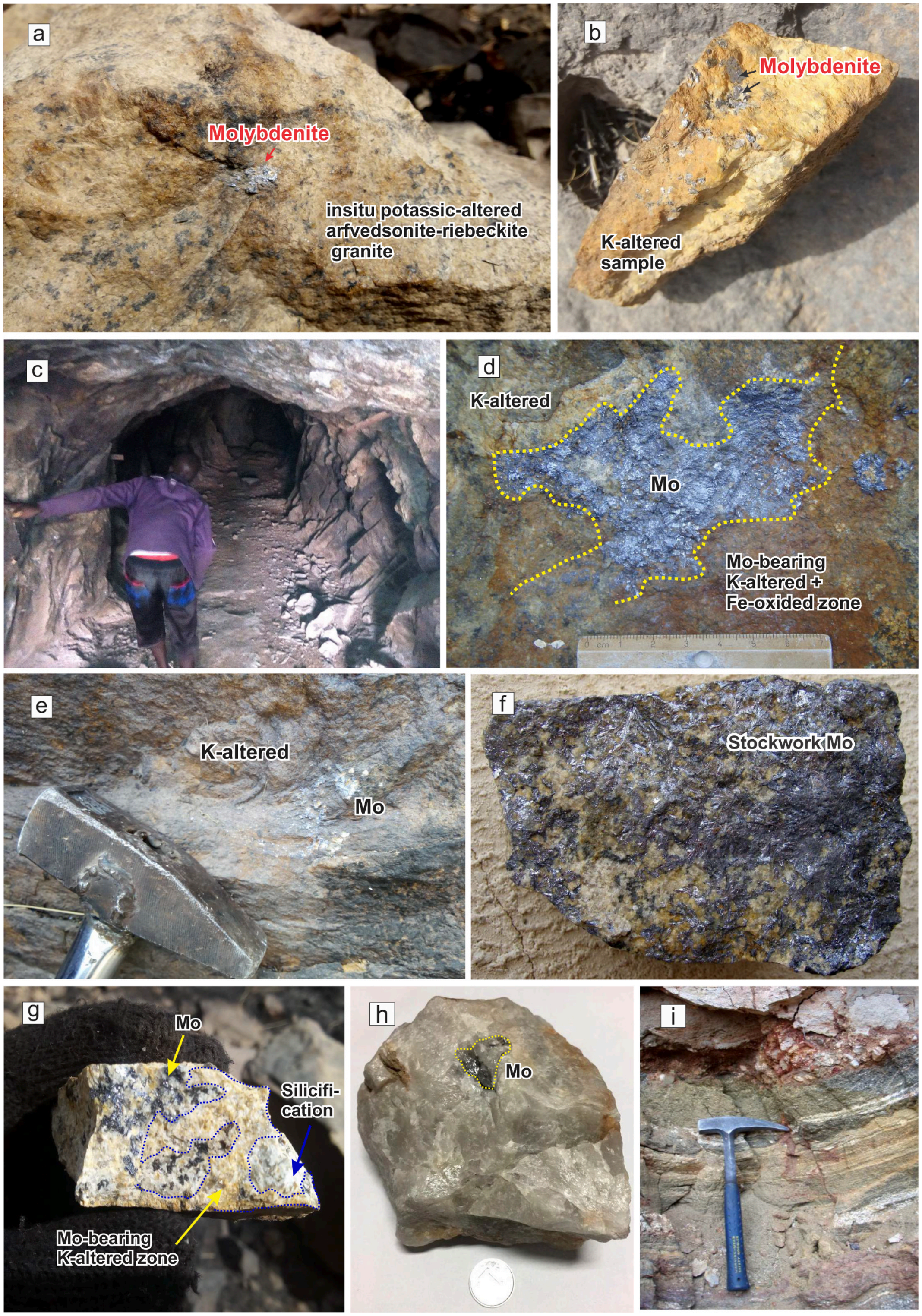

Fig. 7. Mo-Sn mineralization styles in Kigom complex (a) Molybdenite-bearing arfvedsonite-riebeckite granite outcrop; (b) Disseminated molybdenite in K-altered arfvedsonite-riebeckite granite; (c) Abandoned mine shaft in the Kigom complex. (d) Vertical profile of arfvedsonite-riebeckite granite showing K-altered zones, a molybdenite-rich layer, and Fe-oxide overprinting; (e) Localized disseminated molybdenite patches; (f) Stockwork molybdenite veinlets; (g) Patchy molybdenite in silicified K-altered granite; (h) Molybdenite associated with quartz crystals; (i) Cassiterite-bearing gravel layer in alluvial deposits west of Terema.

exhibits multiple styles within potassic-altered arfvedsonite-riebeckite granite, with vertical zonation from a Mo-bearing zone (7–10 cm wide) downward to a K-altered zone with Fe-oxide overprinting. These molybdenite deposits are expressed through veinlet-style mineralization (Fig. 7a–b), discrete patches within K-altered matrix, zonation from K-altered upper zones to Fe-oxide overprinted bases (Fig. 7d-e), pervasive stockworks where interconnected silvery platy molybdenite crystals form a dark bluish metallic sheen (Fig. 7f), lens-shaped silicified zones (Fig. 7g), clustered patchy zones within K-altered and silicified matrices, and isolated dark metallic quartz-hosted patches representing highly

Table 1
Compositions and formulae of the amphibole-group mineral of Jos-Bukuru and Kigom alkaline granites.

Spot no.	JB5-2-Amp1	JB5-2-Amp2	JB5-2-Amp3	JB5-2-Amp4	JB5-2-Amp5	K5-Amp3	K5-Amp4	K5-Amp5	K5-Amp6	K5-Amp7
Root name	Hornblende	Hastingsite	Hastingsite	Hastingsite	Hastingsite	Arfvedsonite	Arfvedsonite	Arfvedsonite	Arfvedsonite	Riebeckite
Subgroup	**Jos-Bukuru complex: Calcic amphibole**					**Kigom complex: sodic amphibole**				
SiO_2	40.61	40.62	40.67	40.56	40.46	50.99	50.86	50.87	50.97	50.89
TiO_2	0.99	0.96	1.07	1.22	1.09	0.09	0.72	0.75	0.77	0.22
Al_2O_3	7.33	7.67	7.49	7.54	7.48	0.49	0.55	0.56	0.54	0.52
Cr_2O_3	0.01	b.d.l	0.01	b.d.l	b.d.l	b.d.l	b.d.l	b.d.l	0.03	b.d.l
FeO_{tot}	32.02	31.95	32.18	31.80	31.71	36.62	35.85	36.00	35.58	35.84
MnO	0.62	0.65	0.66	0.63	0.68	0.67	0.43	0.41	0.47	0.75
MgO	1.61	1.60	1.69	1.65	1.73	0.11	0.17	0.21	0.15	0.09
CaO	9.99	10.13	9.86	9.93	9.98	0.10	b.d.l	b.d.l	b.d.l	0.15
Na_2O	0.27	1.44	1.67	1.06	2.80	7.12	7.16	7.28	7.09	6.89
K_2O	1.78	1.76	1.71	1.69	1.70	0.40	0.24	0.22	0.23	0.37
F	0.43	0.48	0.44	0.38	0.44	0.25	0.07	0.12	0.07	0.23
Total	95.66	97.26	97.45	96.46	98.07	96.84	96.05	96.42	95.9	95.95
H_2O_{calc}	1.40	1.44	1.43	1.42	1.51	1.79	1.80	1.77	1.81	1.81
Fe_2O_{3calc}	7.58	7.57	7.83	7.52	7.67	10.00	8.95	8.97	8.86	9.86
FeO_{calc}	25.20	25.14	25.13	25.03	24.81	27.63	27.79	27.93	27.61	26.97
Formulas based on 24 oxygen atoms										
T-Site										
Si	6.64	6.57	6.57	6.59	6.52	7.91	7.92	7.91	7.93	7.93
Al	1.38	1.44	1.44	1.42	1.49	0.06	0.05	0.06	0.03	0.05
Ti	b.d.l	b.d.l	b.d.l	b.d.l	b.d.l	0.01	0.03	0.03	0.03	0.02
C-Site										
Al	0.03	0.02	b.d.l	0.02	b.d.l	0.03	0.05	0.04	0.07	0.05
Ti	0.16	0.14	0.15	0.18	0.14	b.d.l	0.05	0.06	0.06	0.01
Fe^{3+}	0.93	0.92	0.95	0.92	0.93	1.17	1.05	1.05	1.04	1.16
Mn^{2+}	0.07	0.08	0.08	0.07	0.08	0.08	0.05	0.05	0.06	0.09
Mg	0.39	0.39	0.41	0.40	0.42	0.03	0.04	0.05	0.04	0.02
Fe^{2+}	3.15	3.20	3.18	3.15	3.22	3.44	3.46	3.47	3.45	3.38
B-Site										
Ca	1.76	1.76	1.72	1.74	1.73	0.17	b.d.l	b.d.l	b.d.l	0.19
Na	0.09	0.21	0.23	0.17	0.36	1.64	1.64	1.64	1.65	1.64
A-Site										
Na	b.d.l	0.24	0.30	0.17	0.51	0.51	0.52	0.55	0.49	0.44
K	0.36	0.36	0.35	0.34	0.34	0.10	0.06	0.06	0.06	0.09
W-Site										
OH^-	1.52	1.55	1.54	1.54	1.62	1.85	1.87	1.83	1.88	1.88
F^-	0.20	0.23	0.21	0.18	0.22	0.09	0.01	0.03	0.01	0.08
O_2–	0.28	0.22	0.25	0.28	0.16	0.06	0.12	0.13	0.11	0.04
Mg#	11.0	10.9	11.4	11.3	11.5	0.9	1.1	1.4	1.1	0.6
Thermobarometric estimations (Ridolfi et al., 2010; Schmidt, 1992)										
Temp (°C)	776	785	793	768	802	682	667	694	658	705
P (kbar)	2.52	2.68	2.74	2.45	2.87	1.12	0.98	1.23	0.87	1.34
Depth (km)	7.6	8.1	8.3	7.4	8.7	3.4	3.0	3.7	2.6	4.1

b.d.l.: below detection limit.

localized deposition along fluid pathways (Fig. 7h); and (3) a cassiterite-bearing quartz vein following a basaltic dike orientation 1.2 km north (Buchannan et al., 1971), with an abandoned mine shaft marking the most extensive Mo deposit (Fig. 7c). The mineralization suite also includes sphalerite, chalcopyrite, pyrite, genthelvite, and galena associated with trigonal molybdenite crystals (0.5 mm–4 cm).

Cassiterite deposits west of Terena (Fig. 6a) may have been derived from the weathered roof zone of the metasomatized, albite-rich Daw member of the Ganawuri biotite granite through alluvial reworking. Artisanal cassiterite occurrences imply a late Sn event postdating the main magmatic activity. In the central part of the intrusion, the contact characteristics of the Daw albite-rich metasomatize biotite with the KGM arfvedsonite-riebeckite granite exhibit significant diversity. Near the outer edges, boundaries are typically abrupt and clearly delineated. However, toward the interior, extensive assimilation and reactive processes have blurred the distinction between the two granites, resulting in a gradual, indistinguishable transition. Comparable hybridized contacts are also observed where certain subhorizontal intrusions of the JBK and Kwandonkaya complexes intersect.

3. Analytical methods

Detailed analytical procedures are provided in Supplementary Materials S1. Mineral compositions (amphibole, fluorite) were determined by EPMA (15 kV, 10–20 nA, 3–10 μm beam) at Northwest University, China. Amphibole formulae were calculated on an oxygen basis (Hawthorne et al., 2012; Locock, 2014). Whole-rock major elements were analysed by XRF (ALS Chemex, Guangzhou) and trace elements by ICP-MS (Agilent 7500a) after acid digestion at China University of Geosciences (Wuhan). Zircon U–Pb dating used LA-ICP-MS (193 nm, 25 μm spot) at Wuhan. Whole-rock Rb–Sr and Sm–Nd isotopes were measured by MC-ICP-MS (Neptune Plus) at Wuhan Sample Solution and Beijing Kehuizhi, respectively, with NIST SRM 987 and JNdi-1 as standards.

4. Analytical results

4.1. Amphibole and fluorite chemistry

Amphibole chemistry (Table 1) for JBK and KGM granites was calculated using 24-oxygen formulas (Hawthorne et al., 2012). Analyses

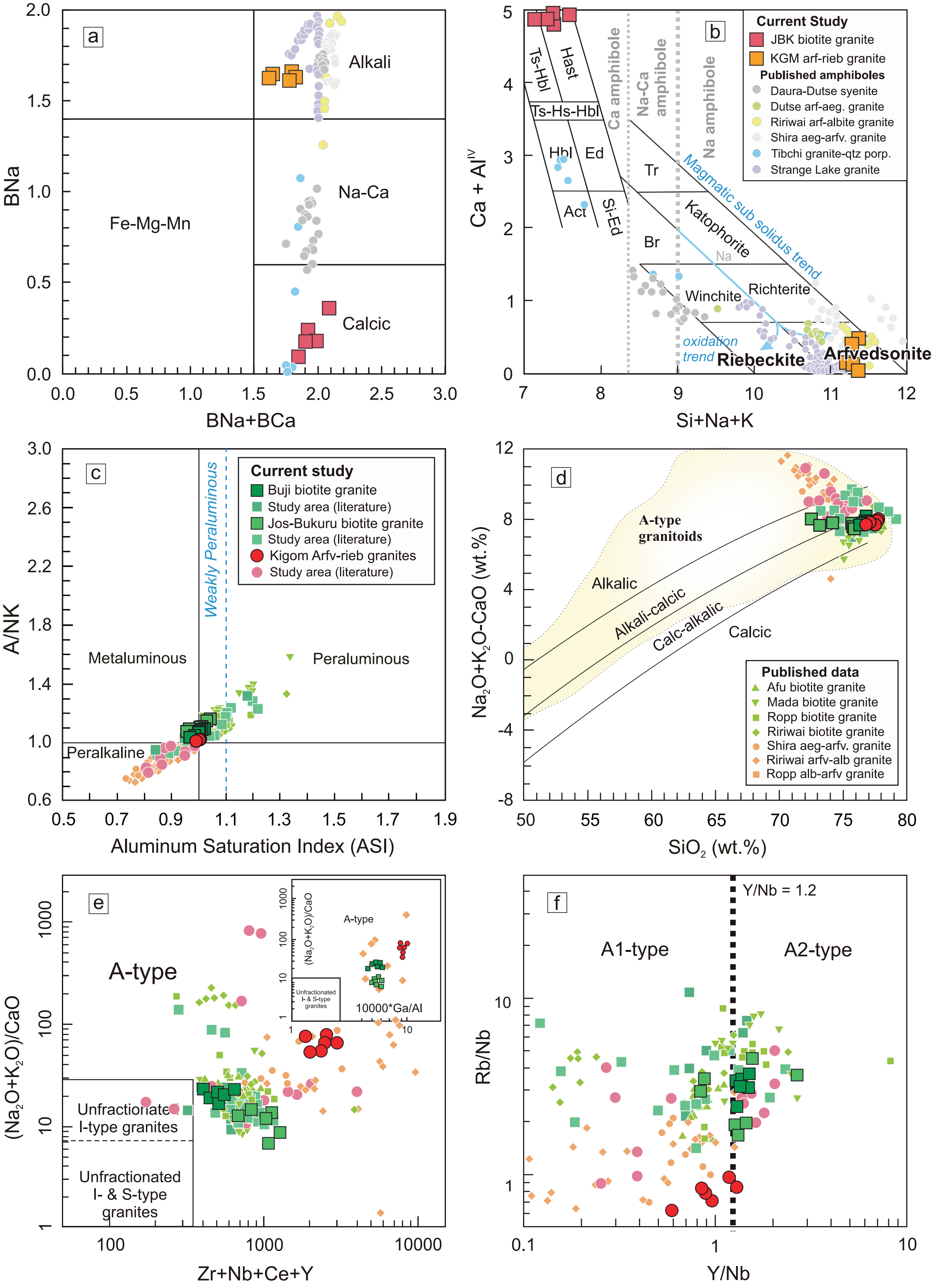

(caption on next page)

Fig. 8. (a) BNa + BCa vs. BNa amphibole classification diagram (after Leake et al., 1997), (b) Si + Na + K vs. Ca + Al^{IV} diagram for amphibole classification based on IMA (modified from Leake et al., 1997; Giret et al., 1980), (c) Whole rock Aluminum Saturation Index (ASI) vs. A/NK granite discrimination diagram (after Frost et al., 2001), (d) SiO_2 vs. $Na_2O + K_2O\text{-}CaO$ (wt.%) granite discrimination diagram (after Frost et al., 2001), (e) Zr + Nb + Ce + Y vs. $(Na_2O + K_2O)/CaO$ discrimination diagram for A-type granites (after Whalen et al., 1987). Inset shows $10^4 \times Ga/Al$ vs. $(Na_2O + K_2O)/CaO$ variation (Whalen et al., 1987). (f) Y/Nb vs. Rb/Nb classification diagram distinguishing A1- and A2-type granites (after Eby, 1992). Compositional comparison of amphiboles from published studies: Daura-Dutse syenite and arfvedsonite-aegirine granite (Vincent et al., 2022b); Ririwai arfvedsonite-albite granite (Kamaunji et al., 2023); Shira aegirine-arfvedsonite granite (Kamaunji et al., 2024); Tibchi granite quartz porphyry (Bennett et al., 1984); and Strange Lake peralkaline granites (Siegel et al., 2017). Nigerian Younger Granite Province comparison data include: Afu complex biotite granite (Cao et al., 2024); Mada complex biotite granite (Girei et al., 2020; Kamaunji et al., 2024); Ririwai complex biotite granite and arfvedsonite-albite granite (Ogunleye et al., 2006; Girei et al., 2019; Kamaunji et al., 2023); and Ropp complex biotite granite and albite-arfvedsonite granite (Amuda et al., 2020; Kamaunji et al., 2022a). Comparison data for biotite granite from the Buji complex (Batchelor and Bowden, 1986), biotite granite from the Jos-Bukuru complex (Imeokparia, 1980; Batchelor and Bowden, 1986), and arfvedsonite-riebeckite ± biotite granite from the Kigom complex (Imeokparia, 1984; Omada, et al., 2003).

Table 2
Compositions of fluorite in the biotite granite from Jos-Bukuru complex.

Spots/oxide	JB2-3	JB2-4	JB2-4	JB4-1	JB4-1	JB4-1	JB4-3	JB4-3
K_2O	b.d.l	b.d.l	b.d.l	b.d.l	b.d.l	0.025	0.003	0.001
P_2O_5	0.025	0.019	0.031	0.019	0.094	0.038	0.031	0.050
SiO_2	b.d.l	b.d.l	b.d.l	b.d.l	b.d.l	b.d.l	b.d.l	b.d.l
MgO	b.d.l	0.001	0.003				0.005	
FeO	b.d.l	b.d.l	0.042	0.020	b.d.l	0.061	b.d.l	b.d.l
MnO	b.d.l	b.d.l	b.d.l	0.034	b.d.l	b.d.l	b.d.l	0.034
TiO_2	0.091	0.012	b.d.l	b.d.l	0.057	b.d.l	b.d.l	b.d.l
CaO	66.22	67.84	68.36	69.32	70.77	69.74	68.16	68.09
Cl	b.d.l	0.007	b.d.l	0.009	0.008	0.001	b.d.l	0.008
SO_3	0.082	0.029	0.004	0.009	b.d.l	0.024	0.015	b.d.l
Na_2O	0.201	0.184	0.159	0.124	0.104	0.120	0.144	0.132
Al_2O_3	0.005	b.d.l	0.018	b.d.l	0.001	0.004	b.d.l	b.d.l
Oxide total	66.62	68.09	68.62	69.54	71.03	70.01	68.36	68.32
Fluorine	55.96	54.80	53.95	55.64	55.35	54.41	54.85	54.74

All elements are in wt.%; b.d.l.: below detection limit.
Note: Oxide totals exclude fluorine. Fluorite (CaF_2) contains F as an anion instead of oxygen; thus, summing F with oxides produces artificially high totals (>120 wt%) in raw EMPA data. The F values reported here are elemental F (wt.%) as measured. Oxide totals are provided separately for clarity and fall within expected ranges for fluorite.

followed IMA-2012 standards (Oberti et al., 2012). JBK amphiboles (Sn-Nb granite) have low B-site Na (0.09–0.36 apfu) and high Ca + Al^{IV} (>4 apfu), classifying as calcic (hastingsite ± hornblende) (Fig. 8a, b). KGM amphiboles (Mo-bearing granite) show high B-site Na (0.09–0.36 apfu) and Si + Na + K (>11 apfu), plotting as sodic (arfvedsonite), overlapping Strange Lake compositions (Fig. 8b) (Fig. 8a, b). Fluorite (Table 2) is CaF_2-dominant (CaO: 66.22–70.77 wt%, F: 53.95–55.96 wt %), with low Na_2O (0.104–0.201 wt%) and Cl (≤0.009 wt%). Calculated Mg# values $[Mg/(Mg + Fe^{2+}) \times 100]$ range from 10.9 to 11.5 in JBK calcic amphiboles and from 0.6 to 1.4 in KGM sodic amphiboles (Table 1).

4.2. Whole rock geochemistry

The granites are near-neutral (ASI ~ 0.94–1.04), metaluminous to weakly peraluminous (Fig. 8c; Frost et al., 2001), and plot from calc-alkalic to alkali-calcic, with KGM extending into alkalic (Fig. 8d). High HFSE (Zr, Nb, Y) and Ga/Al ratios confirm an A-type affinity (Fig. 8e; Whalen et al., 1987). The KGM granites, characterized by Y/Nb ratios <1.2, plot within the A1-type granite field, whereas all Buji granites and most JBK granites plot within the A2-type compositional field (Fig. 8f; Eby, 1992).

Trace element contents vary: JBK granites have moderate Cu, Zn, and Sn with enriched Nb and REEs; Buji granites have lower metals but comparable Nb and REE; KGM granites are notably enriched in Cu, Zn, Pb, Zr, Sn, Nb, and REE (Table 3). Primitive mantle-normalized spider diagrams show that JBK and KGM granites are generally more enriched in incompatible elements than Buji granites, with KGM characterized by higher Pb and HREE-related trace element levels, and JBK showing stronger enrichment in several LILE and LREE components (Fig. 9a). All suites display pronounced negative Ba, Sr, Eu, P, and Ti anomalies. The chondrite-normalized REE patterns confirm strong LREE enrichment, most pronounced in JBK, elevated and relatively flat HREE segments in KGM, and variable negative Eu anomalies across all suites, consistent with feldspar fractionation during magma evolution (Fig. 9b). Notable, the published Ririwai albite-arfvedsonite granites are enriched in most trace elements and REEs relative to the studied granites (Fig. 9a–b).

4.3. Zircon morphology, U-Pb ages, and trace element patterns

Cathodoluminescence (CL) images of zircon grains are shown in Fig. 9c–f. Zircons from Buji biotite-arfvedsonite granite (B9, Fig. 10a) are black to gray, ranging from elongated to equidistant. JBK biotite-amphibole granites (JB9 and JBZ1, Fig. 10b–c) contain euhedral to subhedral prismatic zircons showing concentric bands and pronounced core-rim contrasts. KGM arfvedsonite-riebeckite granite zircons (KZ1, Fig. 10d) are predominantly dark gray with lighter rims and display concentric to diffuse zoning.

Zircon U–Pb ages (Table 4, Fig. 11a–d) show Early Jurassic crystallization for Buji (179.3 ± 0.44 Ma, Th/U = 0.40–0.97) and JBK (JB9; 178.1 ± 0.58 Ma, Th/U = 0.37–1.67) granites. A younger Late Jurassic age is recorded for JBK (JBZ1; 157.5 ± 0.51 Ma, Th/U = 0.33–1.04), while KGM zircons yield a Middle Jurassic age (166.4 ± 6.8 Ma, Th/U = 0.46–1.71). Zircon REE patterns (Table S2) display characteristic magmatic signatures (Hoskin and Schaltegger, 2003), such as Low LREE, positive Ce anomalies, negative Eu anomalies, and HREE enrichment. KGM zircons show greater scatter and higher MREE-HREE than JBK, while Buji zircons define the most coherent patterns (Fig. 11e–f).

4.4. Whole rock Rb-Sr and Sm-Nd isotopes

Whole-rock Sr-Nd isotope data (Table 5, Fig. 12a–d) show systematic variations. KGM granites have highly radiogenic $^{87}Sr/^{86}Sr$ (0.71395–0.72062), near-chondritic $\varepsilon_{Nd}(t)$ (−0.41 to −1.07), and T^{C}_{DM2}

Table 3
Whole rock major and trace element compositions of alkaline granites from Buji, Jos-Bukuru and Kigom alkaline granites.

Rock types	Buji complex: Biotite granites						Jos-Bukuru complex: amphibole-rich Biotite granite						Kigom arfvedsonite-riebeckite biotite granite					
Elements	B1	B3	B6	B9	B10	BZ1	JB1	JB4	JB5	JB6	JB9	JBZ1	K2	K3	K5	K7	K8	KZ1
SiO_2 (wt%)	76.58	76.41	76.64	76.74	76.76	76.68	75.77	74.27	73.2	75.87	73.12	72.71	77.08	77.11	76.83	76.72	77.5	77.7
TiO_2	0.05	0.05	0.05	0.05	0.06	0.05	0.07	0.13	0.26	0.06	0.31	0.12	0.14	0.1	0.15	0.12	0.1	0.10
Al_2O_3	12.08	12.02	12.28	12.22	12.1	12.25	12.14	12.58	12.4	12.44	12.63	13.29	11.12	11.06	10.85	11	10.94	11.4
TFe_2O_3	1.46	1.42	1.52	1.42	1.69	1.42	1.84	2.44	3.83	1.98	4.23	2.5	2.9	2.65	3.04	2.76	2.83	2.78
MnO	0.02	0.02	0.02	0.02	0.03	0.02	0.03	0.03	0.08	0.02	0.09	0.04	0.01	0.01	0.03	0.01	0.03	0.02
MgO	0.04	0.04	0.04	0.05	0.03	0.04	0.04	0.08	0.1	0.06	0.13	0.07	0.01	0.02	0.02	0.02	0.02	0.03
CaO	0.46	0.46	0.46	0.49	0.4	0.47	0.59	0.76	0.94	0.66	1.02	0.79	0.14	0.13	0.12	0.13	0.12	0.12
Na_2O	3.84	3.77	3.85	3.94	4.22	3.84	3.84	3.53	3.74	3.65	3.63	3.6	4.25	4.28	4.29	4.24	4.28	4.22
K_2O	4.56	4.55	4.56	4.76	4.51	4.6	4.46	5.07	4.87	4.4	5.05	5.23	3.77	3.66	3.48	3.68	3.57	3.95
P_2O_5	0.01	0.01	0.01	0.01	0.01	0.01	0.01	0.01	0.04	0.01	0.05	0.01	0.01	0.01	0.01	0.01	0.01	0.01
LOI	0.4	0.4	0.38	0.3	0.25	0.33	0.54	0.63	0.42	0.59	0.47	0.82	0.23	0.24	0.18	0.19	0.19	0.12
Total	99.5	99.2	99.8	100	100.1	99.71	99.33	99.53	99.88	99.74	100.73	99.18	99.66	99.27	99	98.88	99.59	100.4
FeOt	1.3	1.3	1.4	1.3	1.5	1.3	1.7	2.2	3.4	1.8	3.8	2.2	2.6	2.4	2.7	2.5	2.5	2.50
$Na_2O + K_2O$	8.4	8.32	8.41	8.7	8.73	8.44	8.3	8.6	8.6	8.1	8.7	8.8	8.02	7.94	7.77	7.92	7.85	8.17
Mg#	6	6.16	5.78	7.58	3.97	6.16	4.82	7.1	5.74	6.6	6.68	6.13	0.8	1.73	1.51	1.66	1.62	2.45
ASI	1	1.01	0.98	0.96	1.01	1	1.04	1.05	1.01	1.1	1.03	1.08	0.99	0.99	0.99	0.99	0.99	1.00
Q	35.11	32.67	31.14	36.33	30.77	29.99	35.71	35.78	36.06	35.79	34.68	34.34	37.76	38.03	38.41	37.80	38.79	37.76
Or	26.36	29.96	28.78	26.00	29.84	30.91	27.19	26.95	26.89	26.95	28.13	26.65	22.28	21.63	20.57	21.75	21.10	23.34
Ab	32.49	29.87	31.65	30.89	30.72	30.46	32.49	32.49	31.90	32.58	33.34	35.71	35.96	36.22	36.30	35.88	36.22	35.71
DI	93.96	92.50	91.57	93.22	91.33	91.36	95.39	95.22	94.85	95.31	96.15	96.70	96.00	95.87	95.27	95.43	96.10	96.81
TZr (°C)	816	835	834	839	861	816	869	888	899	830	899	860	973	1018	1000	976	976	940
Tetrad	1.14	1.16	1.12	1.15	1.11	1.14	1.09	1.07	1.05	1.10	1.06	1.07	1.18	1.18	1.21	1.19	1.14	1.21
Li (ppm)	48.9	46.7	53.6	3.42	1.55	48.2	148	125	11	143	10.7	103	6.67	4.81	4.48	5.42	4.15	3.94
Be	6.84	6.79	7.36	8.97	9.83	6.57	11.3	20.7	7.29	30.1	6.93	24.6	5.14	5.72	5.36	4.97	5.6	7.72
Sc	0.54	0.54	0.56	0.5	0.42	0.55	0.87	1.15	3.05	0.77	3.38	1.18	0.34	0.52	0.45	0.34	0.35	0.29
V	0.95	0.83	1.49	1.23	1.01	0.91	1	1.83	2.71	0.92	4.02	1.66	0.61	0.66	0.44	1.9	0.75	0.58
Cr	13.5	11.6	12.3	21.4	38.2	12	15	16	13	14.3	11.8	17.5	16.8	24.3	19.6	22	21.6	21.2
Co	0.34	0.34	0.34	0.19	0.22	0.36	0.19	0.68	1.27	0.55	1.39	0.68	0.15	0.13	0.12	0.12	0.13	0.12
Ni	0.67	0.7	0.62	0.66	0.95	0.9	0.71	0.79	0.96	0.59	1.34	0.85	0.78	0.83	0.79	0.78	0.78	0.92
Cu	1.08	0.79	0.93	1.67	3.25	2.2	0.7	4.09	2.45	19.8	3.45	19.4	206	717	317	251	845	443
Zn	43.5	46	47.1	70.8	100	42.6	72	95.6	171	436	189	422	978	1326	654	949	1171	861
Ga	32.4	32.4	32.5	34.4	35.4	32.6	40.3	39	34.5	34.3	34.4	38.8	53.5	55.1	54.8	54	54.2	53.3
Rb	238	237	244	232	229	239	422	505	162	480	168	469	264	265	257	271	256	284
Sr	6.17	5.85	5.85	3.11	2.73	6.16	12	33	49.1	23.2	52.2	28.6	3.42	2.84	2.71	2.85	1.26	2.99
Y	111	111	118	133	124	109	189	136	127	178	140	141	366	420	249	328	325	292
Zr	119	145	147	159	205	119	224	318	430	148	460	259	971	1382	1198	992	983	719
Nb	73.5	81.4	85.3	103	112	76.9	133	156	87.4	114	106	170	382	324	422	367	276	345
Sn	4.4	4.49	6.31	7.72	11.8	4.25	20.4	17.9	20	19.6	20	22	20.9	14.9	15.4	24.4	10.5	14.4
Cs	1.89	2.01	2.01	0.73	1.23	2.08	4.36	6.37	2.39	11.2	2.94	5.18	1.76	1.4	1.76	1.7	1.79	1.54
Ba	23.4	20.9	21.7	5.11	6.12	23.9	98.1	155	321	47.2	324	149	1.58	1	1	1.34	0.94	2.71
La	27.4	28	28.1	23.1	44.7	28.1	67.6	113	122	70.2	153	107	34.3	33.8	37.9	39	56.1	39.8
Ce	67.8	69.8	68.3	60.9	100	71.1	136	201	247	135	305	192	101	98.4	112	114	145	116
Pr	8.27	8.59	8.32	7.75	11.6	8.61	14.9	19.9	28.8	14.6	37	19.7	14	13.6	15.2	15.8	20	15.6
Nd	32.2	32.9	33.6	31.7	43.1	33.1	54.4	65.5	111	50	133	65.2	58.9	57.7	61.8	65.6	85.6	63.4
Sm	10.6	10.5	11.2	11.7	12.9	10.4	13.3	13.6	24.9	12.6	28.3	14	25.6	25.2	25.1	27.5	35.2	25.2
Eu	0.13	0.12	0.11	0.057	0.11	0.13	0.6	0.79	1.43	0.35	1.58	0.78	0.53	0.55	0.5	0.55	0.72	0.55
Gd	13	12.5	13.7	14.1	14.2	12.6	14.1	12.1	22.6	12.7	24.7	13	34.3	36.9	30.3	34.2	44.3	32.3
Tb	2.67	2.67	2.84	3.05	2.86	2.57	3.22	2.54	3.9	3.06	4.21	2.74	7.33	8.23	6.67	7.25	8.96	7.52
Dy	17.7	17	18.5	20.6	19.2	17.2	23.2	17.8	23.6	22.4	25.3	19.1	47.8	54.9	43.1	46	55.1	51.8
Ho	3.49	3.33	3.73	4.16	3.92	3.57	5.36	4.02	4.49	5.3	4.94	4.29	9.41	11.1	8.31	8.94	10.4	10.3
Er	10.3	9.88	11	12	11.4	10.3	17.6	13.1	12.1	18.1	13.3	14	26.6	32	23.5	25	28.1	28.6
Tm	1.61	1.54	1.66	1.85	1.74	1.51	3.01	2.13	1.68	3.08	1.87	2.24	3.78	4.53	3.31	3.55	3.79	4.07

(*continued on next page*)

Table 3 (*continued*)

Rock types	Buji complex: Biotite granites						Jos-Bukuru complex: amphibole-rich Biotite granite						Kigom arfvedsonite-riebeckite biotite granite					
Elements	B1	B3	B6	B9	B10	BZ1	JB1	JB4	JB5	JB6	JB9	JBZ1	K2	K3	K5	K7	K8	KZ1
Yb	9.94	9.66	10.6	11.4	11.1	9.97	19.1	12.9	9.77	20.2	10.9	14.1	21.4	25.8	19.5	19.6	20.9	22.7
Lu	1.35	1.35	1.46	1.55	1.48	1.33	2.68	1.74	1.32	2.68	1.5	1.9	2.66	3.28	2.46	2.46	2.53	2.67
Hf	6.61	8.33	8.71	8.95	11.1	7.14	11.6	12	13.7	6.83	13.7	10.3	36	45.9	47.4	34.7	37.2	26.0
Ta	5.95	5.94	6.86	7.17	7.78	6.38	12.6	11.5	4.79	10.5	4.99	14.2	38.6	24.1	39.4	31.9	19.5	17.4
Tl	0.92	0.94	0.9	0.93	0.86	0.92	1.75	2.36	0.88	2.23	0.87	2.29	1.72	1.52	1.45	1.76	1.52	1.11
Pb	20.8	23	21.3	25.8	22	21.5	35.1	30.7	21.4	33.1	23.3	81.9	163	37	533	25	941	1054
Th	24.2	26.2	24.6	21.4	19.6	25.6	64.3	68.8	26.2	76.2	28.4	60.2	45.3	70.2	43.2	49.1	37.8	68.3
U	6.75	6.96	7.22	6.84	6.02	6.65	15.2	17.7	4.74	23.8	5.11	17.3	14.3	17.3	14.9	15.3	12.5	20.7
P	43.65	43.65	43.65	43.65	43.65	43.65	43.65	43.65	174.6	43.65	218.2	43.65	43.65	43.65	43.65	43.65	43.65	43.65
K	37,771	37,854	39,514	37,439	38,186	37,854	37,024	42,088	40,427	36,526	41,922	43,416	31,296	30,383	28,889	30,549	29,636	32,790
Ti	299.8	299.8	299.8	359.7	299.8	299.8	419.7	779.4	1559	359.7	1858	719.4	839.3	599.5	899.3	719.4	599.5	600
Y/Nb	1.51	1.36	1.38	1.29	1.11	1.42	1.42	0.87	1.45	1.56	1.32	0.83	0.96	1.30	0.59	0.89	1.18	0.85
Nb/Ta	12.35	13.70	12.43	14.37	14.40	12.05	10.56	13.57	18.25	10.86	21.24	11.97	9.90	13.44	10.71	11.50	14.15	19.81
Zr/Hf	18.00	17.41	16.88	17.77	18.47	16.67	19.31	26.50	31.39	21.67	33.58	25.15	26.97	30.11	25.27	28.59	26.42	27.65
ΣREE	207	208	213	204	278	210	375	480	615	370	744	469	388	406	389	409	517	
ΣLREE	286	413	535	283	657	398	151	146	150	150	135	213	235	229	252	263	343	260
δEu	0.01	0.01	0.01	0	0.01	0.01	0.04	0.06	0.06	0.03	0.06	0.06	0.02	0.02	0.02	0.02	0.02	0.02
$(La/Yb)_N$	1.98	2.08	1.89	1.45	2.9	2.02	2.54	6.3	8.92	2.49	10.03	5.42	1.15	0.94	1.39	1.43	1.93	1.26
$(Gd/Yb)_N$	1.08	1.07	1.06	1.02	1.06	1.04	0.61	0.78	1.91	0.52	1.88	0.76	1.32	1.18	1.28	1.45	1.76	1.18
$(La/Sm)_N$	1.67	1.72	1.62	1.27	2.24	1.74	3.28	5.37	3.15	3.6	3.48	4.9	0.86	0.86	0.98	0.91	1.03	1.02

ages (0.99–1.04 Ga). JBK granites have moderately radiogenic Sr (0.70661–0.71727), more depleted $\varepsilon_{Nd}(t)$ (−3.39 to −2.98), and T^{C}_{DM2} ages (1.20–1.24 Ga). Buji granites have the least radiogenic Sr (0.68773–0.70658) and most negative εNd(t) (−4.41 to −4.27), with T^{C}_{DM2} ages (1.31–1.32 Ga). Two samples (one each from KGM and JBK) have anomalously low initial $^{87}Sr/^{86}Sr$ (<BABI 0.69897; Walraven et al., 1990), indicating fluid alteration; these were excluded from Sr interpretations.

5. Discussion

5.1. *Zircon U–Pb chronology and regional age trends*

LA-ICP-MS U-Pb dating of magmatically zoned zircons from the granites constrains their emplacement during the Early–Late Jurassic (ca. 179–157 Ma).The Buji granites yield the oldest ages of ca. 179 Ma, followed by the JBK biotite-amphibole granites with ages of ca. 178–157 Ma (avg. ~168 Ma) and the KGM granites with ages of ca. 166 Ma. The JBK zircon U-Pb ages are consistent, within error, with previously published Rb-Sr whole-rock ages of ca. 161 Ma (Van Breemen et al., 1975) and ca. 164 ± 4 Ma (Dickin et al., 1991). Together with the adjacent southern Ropp complex, these ages define a clear north-to-south younging age trend across the Jos-Plateau tin belt: Buji (~179 Ma) → JBK (~168 Ma) → KGM (~166 Ma) → Ropp (~162 Ma; Kamaunji et al., 2022a; Fig. 1b). This progression extends southward to the Afu and Mada complexes (ca. 148–141 Ma), terminating the Jurassic anorogenic alkaline magmatism in central Nigeria (Girei et al., 2020; Cao et al., 2024; Etsu, 2025; Fig. 1b). The spatiotemporal trend is comparable to regional migration patterns (Rahaman et al., 1984; Table 6; Fig. 1b), reflecting magma source migration along reactivated shear zones (Black et al., 1985). ENE-WSW fractures localized emplacement, creating metallogenic zones.

5.2. *Progressive melting, mantle-crust-fluid hybridization*

To constrain magma sources, we integrated new Sr-Nd isotopic data from Buji, JBK, and KGM granites with regional analogues recalculated at ca. 170 Ma: Late Jurassic to Paleocene (ca. 147–59 Ma) Benue Trough (BT) basalts ($\varepsilon_{Nd}(t)$ = −2.22 to + 6.61; $^{87}Sr/^{86}Sr_{(i)}$ = 0.7025–0.7063; Coulon et al., 1996), Central/north-eastern Nigerian Neoproterozoic (ca. 633–550 Ma) Older Granites ($\varepsilon_{Nd}(t)$ = −22.35 to −9.37; $^{87}Sr/^{86}Sr_{(i)}$ = 0.7042–0.7723; Dickin et al., 1991; Dada et al.,1989, 1995; Ferré et al., 1998), and the central Nigerian Triassic–Early Cretaceous (ca. 232–141 Ma) alkaline-peralkaline granites and syenite ($\varepsilon_{Nd}(t)$ = −8.63 to + 3.84; $^{87}Sr/^{86}Sr_{(i)}$ = 0.7033–0.7220; Dickin et al., 1991; Girei et al., 2019; Kamaunji et al., 2020–2024; Ahmed et al., 2021; Cao et al., 2024; Etsu, 2025) (Table S3; Fig. 12a–b).The Early Jurassic (ca. 179 Ma) Buji barren biotite granites have the most negative $\varepsilon_{Nd}(t)$ values (−4.42 to −4.27) and the least radiogenic $^{87}Sr/^{86}Sr_{(i)}$ (0.7065–0.7066) among the three suites (Fig. 12a–b). Their Paleoproterozoic T^{C}_{DM2} ages (1.31–1.32 Ga) and elevated Neodymium Crustal Index (NCI = 0.31; Fig. 12c) indicate derivation from an enriched subcontinental lithospheric mantle (SCLM) source that experienced long-term crustal metasomatism. Negative *f*Sm/Nd values (−0.37 to −0.34; Fig. 12d) reflect a source with time-integrated LREE enrichment and prolonged crustal residence. The strongly negative $\varepsilon_{Nd}(t)$ values, intermediate between Benue Trough basalts and Pan-African Older Granites (Fig. 12b), point to significant crustal influence, either through source enrichment or assimilation. The low $^{87}Sr/^{86}Sr_{(i)}$ relative to more evolved suites suggests minimal hydrothermal Sr overprint. Buji lacks magmatic fluorite and F-rich assemblages, indicating it did not reach volatile saturation. Thus, Buji represents the most crustally influenced, least differentiated, and volatile-poor endmember.

Progressing to the Early-Late Jurassic (ca. 178–157 Ma, average = ~168 Ma) period, the JBK Sn-Nb biotite-amphibole granites exhibit isotopic decoupling: $\varepsilon_{Nd}(t)$ (−3.32 to −2.98) is less negative than Buji,

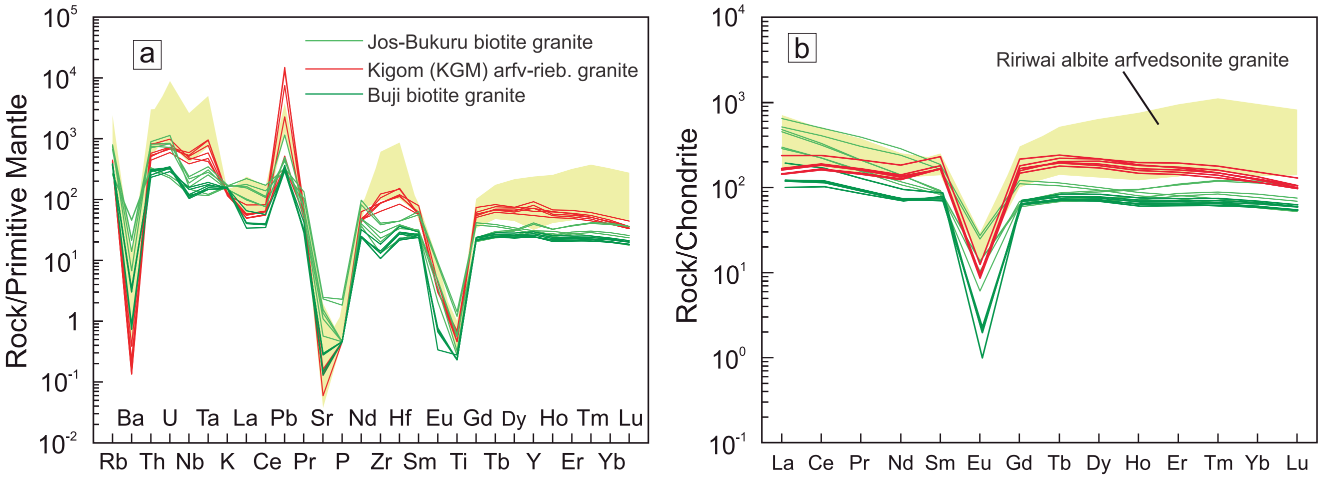

Fig. 9. (a). Primitive-mantle-normalized trace element spider diagrams, and (b) chondrite-normalized REE distributions. Normalization factors were taken from Sun and McDonough (1989). Comparison data of Ririwai albite-arfvedsonite granite were obtained from Girei et al. (2019) and Kamaunji et al. (2023).

indicating a greater mantle contribution, while $^{87}Sr/^{86}Sr_{(i)}$ (0.7066–0.7173) is more radiogenic (Fig. 12a–b). Their intermediate NCI values (0.25; Fig. 12c) and *f*Sm/Nd (–0.35 to +0.09) record a transitional position between the crustally influenced Buji and the mantle-dominated KGM (Fig. 12c–b). JBK contains both calcic amphiboles (hastingsite, hornblende) and sodic amphiboles (arfvedsonite, riebeckite). The preservation of magmatic calcic amphiboles (Fig. 13e) indicates that hydrothermal fluids did not recrystallize the entire amphibole assemblage but selectively affected the Rb-Sr system in fluid-susceptible minerals (feldspar, biotite). The co-existence of calcic and sodic amphiboles has important petrogenetic implications. Calcic amphiboles crystallize from metaluminous to weakly peralkaline melts under relatively oxidizing conditions (FMQ +0.5 to +2), whereas sodic amphiboles require peralkaline melt compositions and more reducing conditions (FMQ −1 to 0; Charles, 1975; Ernst, 1968). Their co-occurrence in JBK suggests that the magma system evolved from initially metaluminous, oxidized conditions toward peralkaline, more reduced conditions as differentiation progressed, driven by feldspar fractionation that increased the Na + K/Al ratio of the residual melt (Scaillet and Macdonald, 2003).

Petrographically, two distinct enclave types independently support this hybrid origin. Mafic microgranular enclaves (MMEs) originated as quenched basaltic intrusions that achieved textural equilibration with the felsic host, indicating mafic magma replenishment (Barbarin, 2005). Felsic microgranular enclaves (FMEs) represent hybridized melts formed through mechanical mixing and chemical exchange between felsic hosts and mafic injections (Alves et al., 2015). The co-occurrence of MMEs and FMEs documents a spectrum from early mafic replenishment to later mixing, consistent with experimental magma mingling models (De Campos et al., 2011; Zhang et al., 2016). Together, the co-existing calcic-sodic amphiboles and MME-FME population provide robust evidence that JBK records a transitional magma system where mantle-derived mafic melts interacted with crustally contaminated felsic melts.

The isotopic decoupling in JBK cannot result from bulk crustal assimilation alone, which would produce correlated Sr-Nd shifts (DePaolo, 1981; Baker et al., 1996). Instead, two processes operated: (1) melting of a mantle source with moderate crustal input (recorded by intermediate ε_{Nd} and T^{C}_{DM2} = 1.24–1.20 Ga), and (2) selective hydrothermal overprint elevating $^{87}Sr/^{86}Sr(i)$ without affecting the Sm-Nd system (Poitrasson et al., 1996; Tu et al., 2025). Thus, JBK records a hybrid signature: mantle-dominated Nd with hydrothermal Sr overprint, amphiboles recording progressive peralkalinity, and enclaves documenting magma mixing, all pointing to an intermediate crustal position between Buji and KGM.

. The Middle Jurassic (ca. 166 Ma) KGM Mo-arfvedsonite-riebeckite granites have the least negative $\varepsilon_{Nd}(t)$ (–1.07 to –0.41), approaching chondritic values, with low NCI (0.14) and positive *f*Sm/Nd (+0.06 to + 0.33) (Fig. 12a–d), confirming a juvenile mantle source with minimal crustal input. However, KGM exhibits the most radiogenic $^{87}Sr/^{86}Sr_{(i)}$ (0.7139–0.7206). This extreme decoupling, near-chondritic ε_{Nd} with radiogenic Sr, cannot result from bulk crustal assimilation (DePaolo, 1981; Dickin et al., 1991). Instead, it records fluid-mediated Sr metasomatism of a mantle-derived magma, supported by extensive hydrothermal assemblages (fluorite, astrophyllite, molybdenite stockworks). KGM shows only the first effect of bulk assimilation: radiogenic Sr accompanied by the least negative εNd, lowest NCI, positive fSm/Nd, and low Y/Nb (0.59–1.30; Fig. 12f). In contrast to JBK's transitional amphibole assemblage, KGM is dominated by sodic amphiboles (arfvedsonite, riebeckite), reflecting fully peralkaline, reduced conditions and a terminal-stage, fluid-saturated differentiate. We therefore interpret KGM Sr isotopes as a post-magmatic overprint on a mantle-dominated, weakly crustally modified magma.

Despite mantle-dominated Nd, KGM samples are metaluminous to slightly peraluminous (ASI = 0.99–1.0; Fig. 8c), contrasting with published peralkaline arfvedsonite granites from the same complex (Imeokparia, 1984; Omada et al., 2003). This can be explained by: metaluminous and peralkaline rocks co-existing along alkaline differentiation trends; crystal accumulation or open-system processes modifying alumina-alkali indices (Zen, 1986; Frost and Frost, 2011; Romano et al., 2003; Andersen and Elburg, 2025); less evolved magmas remaining metaluminous before fractionating to peralkaline residuals (Macdonald and Scaillet, 2006; Marshall et al., 2009); crustal contamination driving peralkaline melts toward metaluminous compositions (DePaolo, 1981; Peccerillo et al., 2003); or alkali feldspar accumulation buffering peralkalinity indices (Romano et al., 2003; Andersen and Elburg, 2025). Critically, sodic amphiboles can crystallize from local peralkaline melt domains while feldspars buffer the bulk composition to metaluminous values (Schönenberger et al., 2006; Marks et al., 2011). Thus, amphibole chemistry, confirming KGM amphiboles as arfvedsonite (Fig. 8b), provides a more direct record of melt peralkalinity than whole-rock composition.

The markedly lower Mg# of KGM sodic amphiboles (0.6–1.4) relative to JBK calcic amphiboles (10.9–11.5; Table 1) records extreme Fe-enrichment and higher magma differentiation, consistent with KGM as a terminal-stage, fluid-saturated differentiate. This is reflected in amphibole chemistry (higher Si^{IV}, moderate Na + K + Ca; Fig. 13e), plotting KGM amphiboles in the late- to post-magmatic field. Late-magmatic crystallization is evidenced by arfvedsonite preceding aegirine and arfvedsonite-titanite co-crystallization (Fig. 6d–g). Post-magmatic processes are supported by riebeckite replacement by

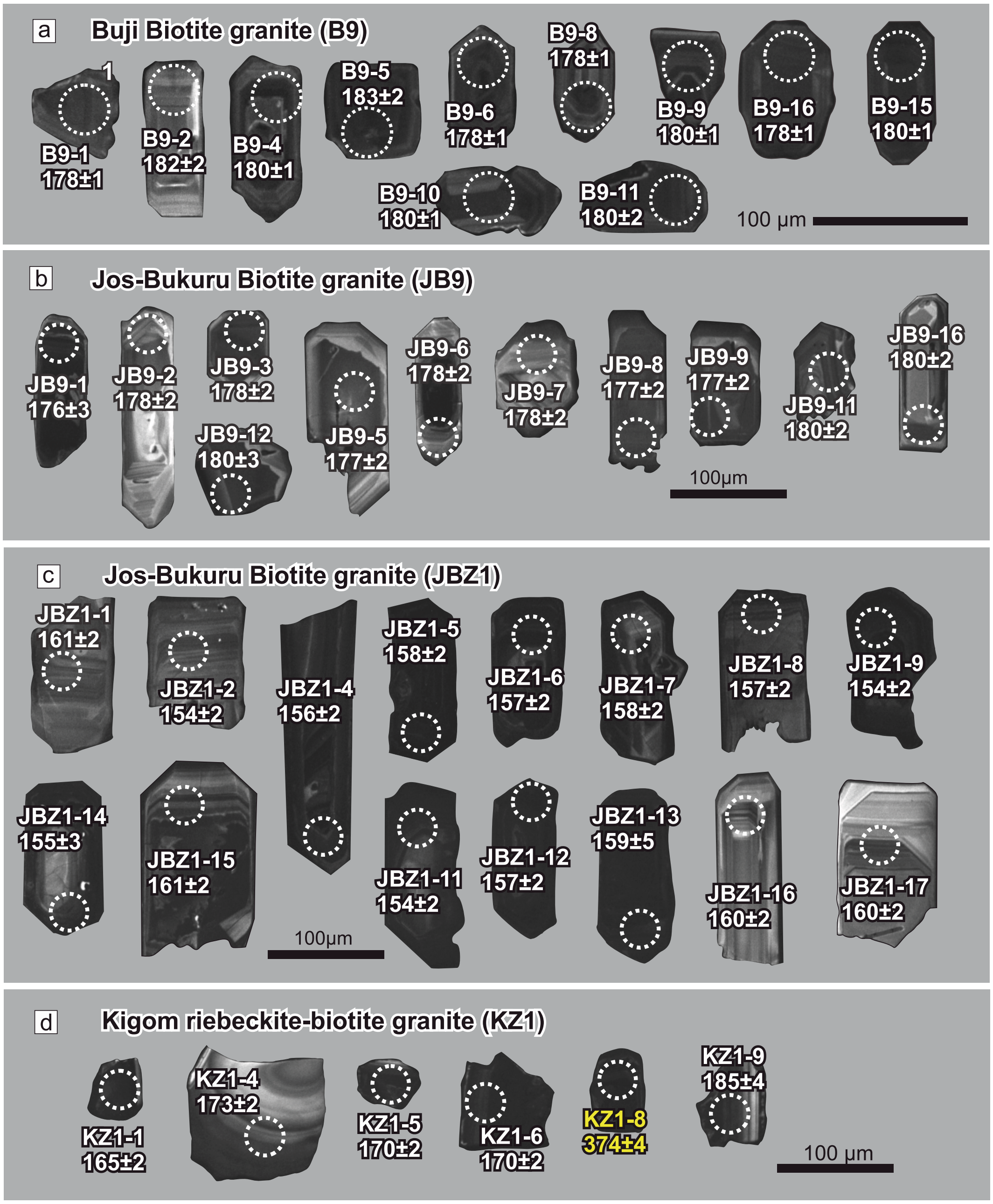

Fig. 10. (a-d) Cathodoluminescence (CL) image of zircons extracted from the studied alkaline granites. Note. KZ1-8 (374 ± 4) is an inherited zircon.

arfvedsonite with astrophyllite borders, subsolidus arfvedsonite-astrophyllite clusters, crystallization within astrophyllite-dominated groundmass, and late fluorite-titanite-zircon assemblages (Fig. 6d, 6f–j), all indicating open-system fluid-rock reaction. Amphibole textures (honeycomb arfvedsonite in hornblende, hastingsite–arfvedsonite rims; Fig. 5d, 5j–k) indicate incomplete equilibration between Na-rich melts and Ca-F-rich fluids. These relationships indicate that while some arfvedsonite crystallized from late-stage melts, much formed during subsolidus alteration, consistent with fluid-mediated Sr metasomatism.

Sr is mobile during alteration of feldspar- and biotite-bearing domains, disturbing the Rb-Sr system (Ma and Liu, 2001; Glodny and Grauert, 2009). In contrast, the Sm-Nd system is less readily reset because Nd is hosted in REE-rich accessory minerals (apatite, monazite, allanite, titanite, xenotime) that retain Nd at the thin-section scale (Bea, 1996; Su et al., 2023). The KGM data are therefore best explained by selective Rb-Sr re-equilibration along late fluid pathways, while $\varepsilon_{Nd}(t)$, NCI, and *f*Sm/Nd preserve the primary source signal. The ε_{N}d, NCI, and fSm/Nd define a coherent north-to-south trend (Fig. 12a, c–d). Buji (ε_{Nd} = –4.4; NCI = 0.31; negative *f*Sm/Nd) is the most crustally influenced; JBK is intermediate (ε_{Nd} = –3.3; NCI = 0.25; positive *f*Sm/Nd); KGM (ε_{Nd} = –0.4; NCI = 0.14; positive fSm/Nd) is the most mantle-dominated. Y/Nb ratios provide independent support: Buji (1.1–1.5) > JBK (0.8–1.6) > KGM (0.6–1.3), with values >1.2 indicating crustal input (Eby, 1992; Fig. 12f). The overlap between JBK and Buji reflects source heterogeneity, not systematic assimilation.

We interpret isotope systematics at two levels. ε_{Nd}, NCI, *f*Sm/Nd, Y/Nb, and Nb-Ta are source-sensitive indicators of mantle vs. crustal contribution (DePaolo et al., 1992; Eby, 1992; Green, 1995). Radiogenic Sr in JBK and KGM is alteration-sensitive, decoupled from ε_{Nd} (Li et al., 2022a,b and coincident with petrographic evidence for late fluid activity. This separation explains why KGM is the most mantle-dominated in Nd isotope space yet records the strongest Sr disturbance. Comparable Sr-Nd decoupling occurs in mineralized peralkaline systems such as the Ilímaussaq Complex (Greenland) and Damara orogen (Namibia), where

Table 4
LA-ICP-MS U-Pb isotope analytical results of zircon grains extracted from Buji, Jos-Bukuru and Kigom alkaline granites.

Samples	Elements		Ratio	Isotopic ratios							Isotopic ages (Ma)						Conc.
Spot no.	Th	U	Th/U	$^{207}Pb/^{206}Pb$	1σ	$^{207}Pb/^{235}U$	1σ	$^{206}Pb/^{238}U$	1σ	rho	$^{207}Pb/^{206}Pb$	1σ	$^{207}Pb/^{235}U$	1σ	$^{206}Pb/^{238}U$	1σ	
Buji biotite granite (sample B9)																	
B9-1	411	678	0.61	0.0499	0.0016	0.1931	0.0060	0.0280	0.00023	0.27	191	72	179	5	178	1	99%
B9-2	487	785	0.62	0.0506	0.0014	0.2006	0.0057	0.0287	0.00024	0.29	220	67	186	5	182	2	98%
B9-4	1096	1636	0.67	0.0502	0.0011	0.1963	0.0045	0.0283	0.00021	0.33	211	54	182	4	180	1	98%
B9-5	464	1159	0.40	0.0503	0.0013	0.1999	0.0050	0.0289	0.00036	0.50	209	92	185	4	183	2	99%
B9-6	565	1224	0.46	0.0497	0.0012	0.1925	0.0044	0.0280	0.00020	0.30	189	56	179	4	178	1	99%
B9-8	306	593	0.52	0.0492	0.0015	0.1897	0.0056	0.0280	0.00024	0.29	167	75	176	5	178	1	99%
B9-9	727	1222	0.59	0.0497	0.0012	0.1925	0.0046	0.0280	0.00023	0.35	189	56	179	4	178	1	99%
B9-10	548	960	0.57	0.0490	0.0013	0.1920	0.0050	0.0283	0.00022	0.30	146	63	178	4	180	1	99%
B9-11	726	1289	0.56	0.0498	0.0012	0.1951	0.0046	0.0283	0.00026	0.38	183	56	181	4	180	2	99%
B9-15	659	1139	0.58	0.0500	0.0013	0.1959	0.0049	0.0283	0.00020	0.29	195	27	182	4	180	1	99%
B9-16	713	1262	0.56	0.0509	0.0012	0.1969	0.0045	0.0280	0.00019	0.30	235	49	183	4	178	1	97%
Jos-Bukuru biotite granite (sample JB9)																	
JB9-1	189	447	0.42	0.0505	0.0018	0.1910	0.0068	0.0277	0.00047	0.48	217	85	177	6	176	3	99%
JB9-2	120	322	0.37	0.0504	0.0020	0.1925	0.0073	0.0280	0.00029	0.27	213	93	179	6	178	2	99%
JB9-3	217	285	0.76	0.0502	0.0024	0.1935	0.0092	0.0280	0.00036	0.27	211	111	180	8	178	2	99%
JB9-5	208	551	0.38	0.0482	0.0015	0.1858	0.0058	0.0279	0.00025	0.29	109	79	173	5	177	2	97%
JB9-6	217	310	0.70	0.0491	0.0022	0.1891	0.0085	0.0279	0.00030	0.24	150	107	176	7	178	2	99%
JB9-7	218	379	0.57	0.0497	0.0019	0.1917	0.0073	0.0280	0.00028	0.26	189	89	178	6	178	2	99%
JB9-8	389	310	1.25	0.0481	0.0033	0.1899	0.0165	0.0279	0.00039	0.16	106	156	177	14	177	2	99%
JB9-9	785	576	1.36	0.0499	0.0021	0.1926	0.0082	0.0279	0.00034	0.28	191	94	179	7	177	2	99%
JB9-11	195	514	0.38	0.0516	0.0020	0.2007	0.0072	0.0282	0.00028	0.28	333	82	186	6	180	2	96%
JB9-12	115	126	0.91	0.0510	0.0033	0.1942	0.0113	0.0283	0.00049	0.30	243	148	180	10	180	3	99%
JB9-13	248	669	0.37	0.0523	0.0017	0.2018	0.0066	0.0280	0.00028	0.31	298	76	187	6	178	2	95%
JB9-16	315	420	0.75	0.0532	0.0020	0.2066	0.0071	0.0283	0.00028	0.29	339	83	191	6	180	2	94%
JB9-18	238	242	0.99	0.0628	0.0039	0.2388	0.0137	0.0284	0.00047	0.29	702	133	217	11	180	3	81%
Jos-Bukuru biotite granite (Sample JBZ1)																	
JBZ1-15	167	162	1.03	0.0507	0.0031	0.1732	0.0096	0.0253	0.00034	0.24	233	143	162	8	161	2	99%
JBZ1-1	111	302	0.37	0.0474	0.0020	0.1653	0.0067	0.0254	0.00028	0.28	77.9	91	155	6	161	2	96%
JBZ1-17	155	388	0.40	0.0526	0.0021	0.1811	0.0068	0.0252	0.00024	0.25	322	123	169	6	160	2	94%
JBZ1-7	156	465	0.33	0.0486	0.0025	0.1679	0.0082	0.0249	0.00030	0.25	128	72	158	7	158	2	99%
JBZ1-5	128	348	0.37	0.0486	0.0025	0.1677	0.0077	0.0249	0.00029	0.25	132	125	157	7	158	2	99%
JBZ1-6	126	344	0.37	0.0490	0.0027	0.1686	0.0089	0.0247	0.00029	0.22	150	128	158	8	157	2	99%
JBZ1-8	121	329	0.37	0.0484	0.0030	0.1658	0.0096	0.0246	0.00033	0.23	120	141	156	8	157	2	99%
JBZ1-12	144	326	0.44	0.0492	0.0029	0.1679	0.0093	0.0246	0.00033	0.24	154	145	158	8	157	2	99%
JBZ1-4	239	229	1.04	0.0485	0.0031	0.1653	0.0104	0.0245	0.00031	0.20	120	144	155	9	156	2	99%
JBZ1-2	183	487	0.38	0.0492	0.0018	0.1650	0.0057	0.0242	0.00027	0.33	167	81	155	5	154	2	99%
JBZ1-11	222	229	0.97	0.0495	0.0036	0.1648	0.0111	0.0241	0.00036	0.22	169	176	155	10	154	2	99%
JBZ1-9	126	193	0.66	0.0486	0.0039	0.1622	0.0121	0.0241	0.00039	0.21	128	178	153	11	154	2	99%
JBZ1-10	122	373	0.33	0.0483	0.0033	0.1624	0.0105	0.0241	0.00034	0.22	122	211	153	9	154	2	99%
JBZ1-13	87.6	110	0.80	0.0500	0.0035	0.1696	0.0104	0.0250	0.00084	0.55	195	165	159	9	159	5	99%
JBZ1-16	162	431	0.38	0.0536	0.0022	0.1858	0.0077	0.0251	0.00030	0.29	354	93	173	7	160	2	92%
JBZ1-14	72.7	117	0.62	0.0551	0.0039	0.1793	0.0119	0.0244	0.00047	0.29	417	157	167	10	155	3	92%
Kigom arfvedsonite-riebeckite granite (sample KZ1)																	
KZ1-1	458	1001	0.46	0.0493	0.0015	0.1766	0.0054	0.0260	0.00035	0.44	165	66	165	5	165	2	99%
KZ1-4	994	1344	0.74	0.0552	0.0016	0.2071	0.0057	0.0272	0.00029	0.39	420	58	191	5	173	2	90%
KZ1-5	888	768	1.16	0.0519	0.0013	0.1921	0.0050	0.0267	0.00025	0.36	283	53	178	4	170	2	94%
KZ1-6	812	476	1.71	0.0508	0.0019	0.1859	0.0067	0.0268	0.00035	0.37	232	90	173	6	170	2	98%
KZ1-9	1138	812	1.40	0.0471	0.0060	0.1799	0.0214	0.0290	0.00071	0.21	58	287	168	18	185	4	90%
KZ1-8	270	344	0.79	0.0548	0.0017	0.4504	0.0129	0.0597	0.00062	0.37	467	67	378	9	374	4	98%

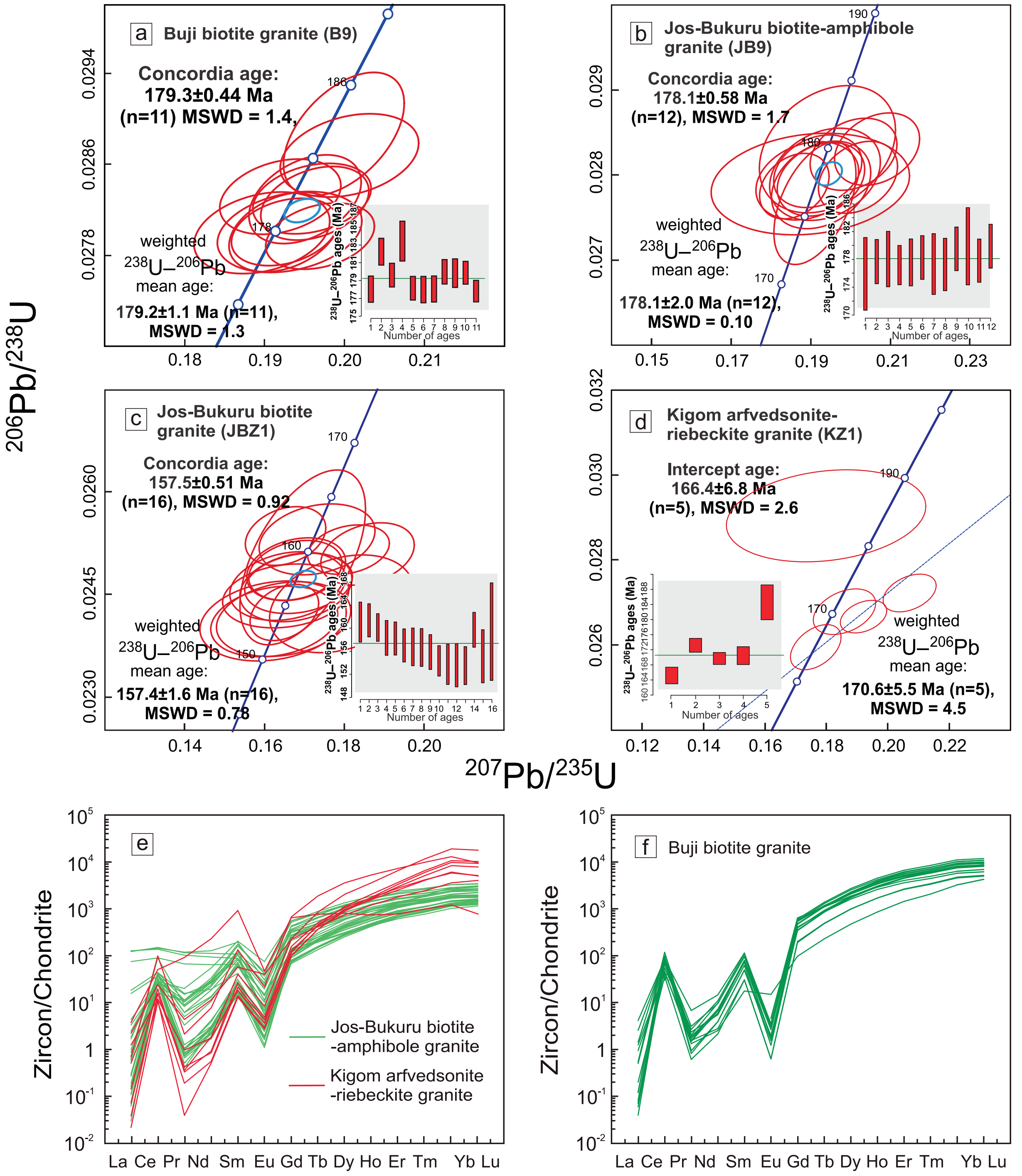

Fig. 11. (a–d). LA-ICP-MS zircon U-Pb age concordia plots of (a) Buji biotite granite, (b–c) Jos-Bukuru biotite granites, (d) Kigom arfvedsonite-riebeckite granite, (e–f) Zircon Chondrite-normalized REE patterns for the zircons extracted from studied alkaline granites.

Sm-Nd remains robust while Rb-Sr records fluid modification (Marks et al., 2003; Jung et al., 2014; Borst et al., 2019).

Synthesizing these lines of evidence, the Buji → JBK → KGM progression records a coherent evolution from crustally enriched, volatile-poor Buji, through transitional JBK with co-existing calcic-sodic amphiboles and MME-FME populations documenting magma mixing, to mantle-dominated, fluid-overprinted, sodic-amphibole-only KGM. This progression is primarily an isotopic and source-evolution trend, not a simple spatial increase in volatile enrichment. Buji lacks magmatic fluorite, indicating it did not reach a volatile-saturated stage. In contrast, volatile involvement is recorded in JBK and especially KGM by fluorite-bearing assemblages, sodic amphiboles, astrophyllite, late fluorite-titanite-zircon associations, greisenized zones, molybdenite stockworks, and selective Rb-Sr disturbance. In KGM, decoupling between peralkaline mineralogy and metaluminous whole-rock compositions (Fig. 8c) provides additional evidence for complex post-magmatic modification involving limited crustal assimilation and extensive fluid metasomatism. This model reconciles the isotopic, geochemical, mineralogical, and petrographic evidence for decreasing crustal influence and increasing fluid-mediated overprinting along the Buji–JBK–KGM magmatic spectrum.

Table 5

Whole rock Rb-Sr and Sm-Nd isotopic compositions of granites from Kigom, Jos-Bukuru, and Buji complexes, north-central Nigeria.

Complex	Rock ID and type		Rb ppm	Sr ppm	Age (Ma)	$^{87}Rb/^{86}Sr$	$^{87}Sr/^{86}Sri$	$\varepsilon_{Sr}(t)$	Sm ppm	Nd ppm	$^{147}Sm/^{144}Nd$	$^{143}Nd/^{144}Nd$	$\varepsilon_{Nd}(t)$	T^{C}_{DM2} (Ga)	fSm/Nd
Kigom	KZ1	Arfvedsonite-riebeckite granite	3.41	269	166	238	0.7206	232	23.73	68.51	0.2096	0.51240	−0.41	0.99	0.06
	K3	Arfvedsonite-riebeckite granite	3.12	253	166	248	0.7139	137	24.57	56.72	0.2621	0.51237	−1.07	1.04	0.33
	K5	Arfvedsonite-riebeckite granite	2.74	242	166	271	*0.6858	262	24.21	61.14	0.2396	0.51237	−1.07	1.04	0.21
Jos-Bukuru	JBZ1	Biotite granite	29.7	441	157	43.2	0.7128	121	13.69	64.86	0.1954	0.51228	−3.12	1.20	−0.01
	JB1	Biotite granite	13.1	418	157	94.4	0.7173	184	13.22	54.56	0.2151	0.51228	−3.12	1.20	0.09
	JB5	Biotite granite	52.8	160	178	8.75	0.7066	32.8	25.01	116.4	0.1989	0.51224	−3.39	1.24	0.01
	JB9	Biotite granite	55.5	162	178	8.44	0.7067	34.2	27.93	136.2	0.1277	0.51226	−2.98	1.21	−0.35
Buji	BJZ1	Biotite granite	6.29	223	179	94.4	*0.6877	235	9.73	30.12	0.1466	0.51218	−4.38	1.32	−0.26
	BJ9	Biotite granite	3.27	222	179	8.75	0.7065	31.1	11.70	32.90	0.1301	0.51219	−4.27	1.31	−0.34
	BJ6	Biotite granite	6.20	229	179	8.44	0.7066	32.5	10.40	31.62	0.1240	0.51218	−4.41	1.32	−0.37

The $^{87}Sr/^{86}Sri$ values of *0.6858 and *0.6877 for the Kigom and Jos-Bukuru granite samples are below the basaltic achondrite best initial (BABI) standard (0.69897 ± 3, Walraven et al., 1990), suggesting fluid disturbances. These samples were therefore excluded from the Sr isotopic interpretations.

5.2.1. *Quantifying crust-mantle hybridization through Sr-Nd mixing models*

To further quantify this hybridization and evaluate source contributions, DePaolo's (1979) conceptual framework was used to construct Sr–Nd isotope mixing models. In this framework, mixing trajectories in Nd–Sr space trace source contributions and the degree of crustal assimilation during magma evolution. Our model supports a two-stage process involving three end-members: Benue Trough OIB basalt, high-$^{87}Sr/^{86}Sr_{(i)}$, low-$\varepsilon_{N}d(t)$ upper crust, and a moderate-$^{87}Sr/^{86}Sr_{(i)}$, highly negative-$\varepsilon_{Nd}(t)$ lower crust (Table S3; Fig. 12b). Phase 1 involved ~10% assimilation of crustal component 1 by the OIB parent melt, generating a syenitic hybrid, followed by Phase 2, where the hybrid melt incorporates up to 30–40 vol% of a plagioclase-rich crustal contaminant (Fig. 12b). The moderately negative $\varepsilon_{Nd}(t)$ values of Benue Trough basalts (–2.22 to –1.50; Coulon et al., 1996) and of the Shira syenite (–4.75; Kamaunji et al., 2024), all recalculated to ca. 170 Ma (Table S3), support crustal overprinting of mantle-derived precursors.

5.2.2. *Trace element constraints on petrogenesis*

In the Buji barren biotite granites, Low Sr (4.98 ppm) and Ba (16.9 ppm) coupled with high Rb/Sr (53) reflect extensive feldspar fractionation, as both elements are strongly partitioned into plagioclase and K-feldspar (Dorado et al., 2023). This interpretation is supported by the low Sr/Y ratio (0.04), which indicates plagioclase-dominated fractionation at shallow crustal levels (Drake and Weill, 1975). Moderate REE concentrations (LREE = 158 ppm; HREE = 62 ppm) and a low La/Yb ratio (2.86) suggest minimal LREE/HREE fractionation and only weak crustal interaction (Moyen, 2009). Collectively, these trace-element characteristics identify Buji as the earliest and least hybridized stage, where mantle-derived alkaline melts underwent efficient feldspar fractionation but experienced minimal crustal input.

JBK has high Rb (368 ppm) and extreme Rb/Sr (11.1) coupled with very low Sr (33 ppm) and Ba (182 ppm). These values reflect extensive feldspar fractionation, which removes Sr and Ba while concentrating Rb in the residual melt (Imeokparia, 1981; Henderson and Pierozynski, 2012). However, such extreme Rb/Sr cannot be achieved by fractional crystallization alone from a mantle-derived melt; it requires assimilation of Rb-rich upper crust (Jain et al., 2024). This interpretation is supported by elevated Th/U (4.3), Y/Yb (10.84), and LREE/HREE (5.43), all signatures of upper continental crust (Rudnick and Gao, 2003). Thus, JBK records two-stage evolution: mantle-derived melts underwent significant crustal assimilation and feldspar-dominated AFC, acquiring elevated LREE, Th, and Y/Yb through crustal contamination, not direct mantle extraction.

The KGM a terminal-stage, fluid-saturated differentiate signature. Extreme Rb/Sr (110) and ultralow Sr (2.68 ppm) and Ba (1.43 ppm) reflect exhaustive feldspar fractionation, (Icenhower and London, 1996; Dorado et al., 2023). The ultralow Sr/Y (<0.01) indicates shallow, plagioclase-stable conditions (Moyen, 2009; Ni et al., 2025). This geochemistry records terminal-stage fluid metasomatism (Bénard and Ionov, 2013) from the crystallizing melt, which evolved into a peralkaline fluid. This is evidenced by the system's highest Y/Yb (15.23) and lowest LREE/HREE (1.68), signifying strong HREE enrichment driven by volatile/fluid complexing (Bau, 1996; Salvi and Williams-Jones, 2005; Kovalenko et al., 1995). Progressive LREE/HREE decrease (5.43 → 1.68) and Y/Yb increase (10.84 → 15.23) define a spectrum from melt-assisted crustal transfer (JBK) to fluid-dominated redistribution (KGM; Migdisov et al., 2009). JBK records melt-dominated crustal hybridization (intermediate ε_{Nd}, NCI, moderately radiogenic Sr); KGM records mantle-dominated Nd overprinted by late fluid-assisted Sr redistribution. Localized crustal assimilation in KGM (hybridized contacts, xenocrystic components) did not dominate the Nd isotope budget. Nb/Ta ratios (10–21; avg. 14) overlap with BSE (~17) and OIB-MORB (~15) values (Pfänder et al., 2007), suggesting low-degree melting of metasomatized SCLM with conservative Nb-Ta behavior preserving near-BSE signatures. Transitional OIB-like syenites (sodic, Na_2O = 3.96–7.32 wt%; HFSE-enriched, Zr ≤ 3764 ppm,

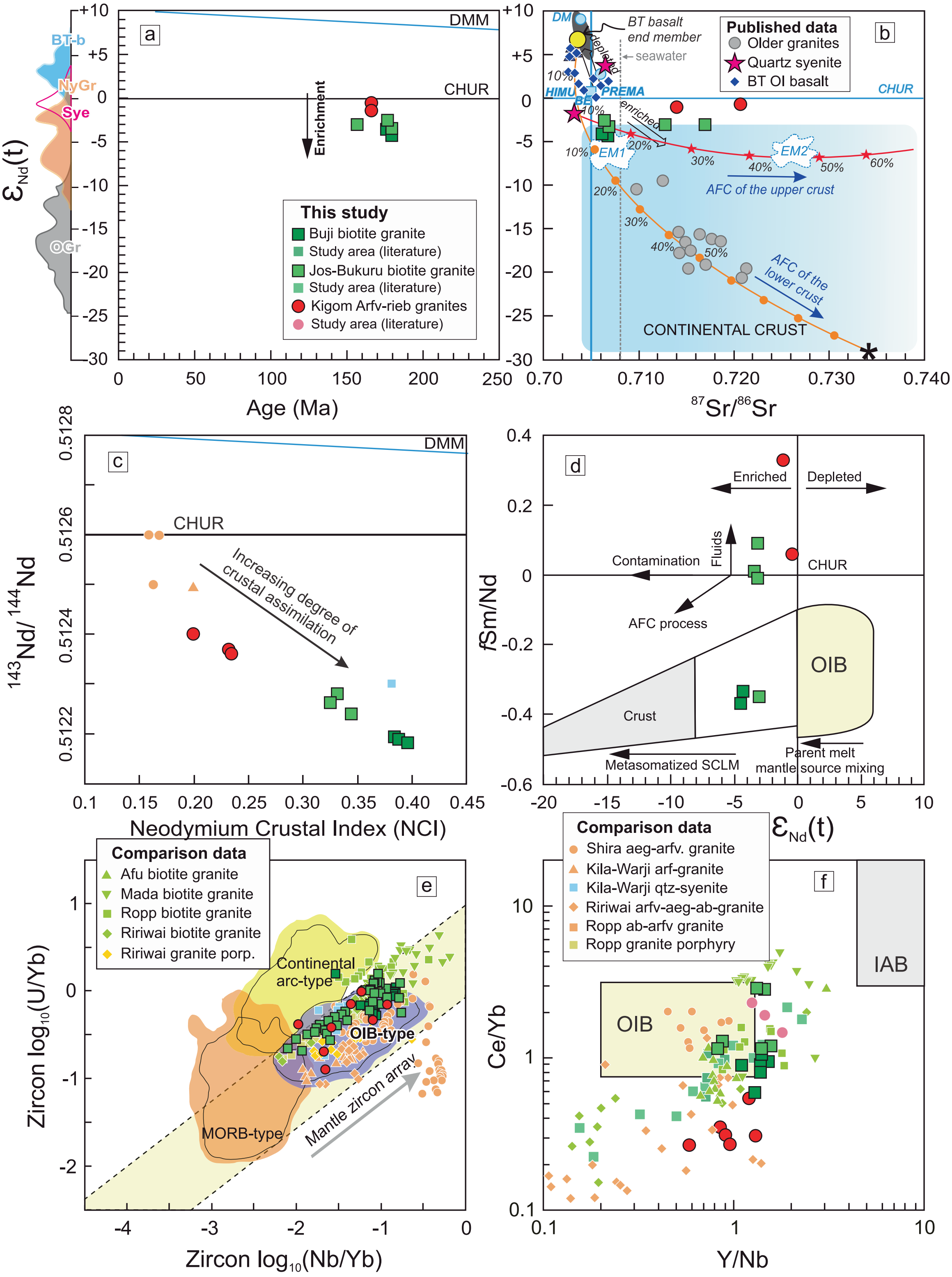

Fig. 12. (a) Age vs. whole rock $\varepsilon_{Nd}(t)$ diagram showing kernel density estimates of Benue Trough (BT-b), Nigerian Younger Granite (NyG) and syenite (Sye), and Neoproterozoic Older granites recalculated at ca. 170 Ma (See Table S3 for references); (b) $^{87}Sr/^{86}Sr$ vs. $\varepsilon_{Nd}(t)$ showing two-stage mixing model and oceanic reservoirs. These include the depleted mantle (DM), bulk silicate Earth (BE), enriched mantle (EM1, EM2), high-μ (U/Pb) (HIMU), the 'prevalent mantle' (PREMA) compositions (Data compiled from Zindler and Hart (1986) and Jackson and Dasgupta (2008); (c) Neodymium Crustal Index (NCI) vs. $^{143}Nd/^{144}Nd$ diagram (NCI = ε_{Nd}(Rock) – ε_{Nd}(MC)/ ε_{Nd}(CC) – ε_{Nd}(MC; DePaolo et al., 1992). NCI calculation was performed using averages of endmember compositions recalculated at 170 Ma (See Table S3); Rock = Nd isotope of the studied granites; MC = mantle component represented by the Benue Trough basalt (Coulon et al., 1996); CC = crustal component represented by the Neoproterozoic Older granites (Dada et al., 1989; Dickin et al., 1991; Ferré et al., 1998); (d) Whole rock $\varepsilon_{Nd}(t)$ vs. fSm/Nd; (e) $\log_{10}$(Nb/Yb) vs. $\log_{10}$(U/Yb) diagram of zircons (after Grimes et al., 2015); (f) Whole rock Y/Nb vs. Ce/Yb (after Eby, 1992). Whole rock comparison data is the same as in Fig. 8.

Table 6
Age distribution of alkaline complexes and associated mineralization in the Niger-Nigerian Younger Granite Province.

Province	Complex	Age	Dating method and reference	A-type granite-hosted mineralization
Niger Younger Granite Province (NgYGP) (Paleozoic)				
Aïr Massif (northern Niger)	Adrar Bous & Ofoud	487 ± 5 Ma 430 ± 15 Ma	Rb-Sr whole rock isochron (Karche and Vachette, 1978) Rb–Sr whole rock (Bowden et al., 1976)	Sn-Nb-Zn, Be (Perez, 1985)
Aïr Massif (northern Niger)	Tamgak	429 ± 4 Ma 455 ± 19 Ma	Single Rb/Sr whole-rock isochron (Karche and Vachette, 1978) Rb–Sr whole rock Isochron age (Moreau et al., 1994)	No reported ore deposits
Aïr Massif (northern Niger)	Ofoud and Meuguer-Meuguer	414 ± 9 Ma 409 ± 12 Ma	Rb/Sr Isochron age from 5 rocks (Moreau et al., 1994)	No reported ore deposits
Aïr Massif (northern Niger)	Abontorok	399 ± 10 Ma	Rb-Sr whole rock isochron (Karche and Vachette, 1978)	No reported ore deposits
Aïr Massif (northern Niger)	Goundaï and Bilet	373 ± 5 Ma	Rb-Sr whole rock isochron (Bonhomme and Pacquet, 1977)	U, Th (Moreau et al., 1994)
Aïr Massif (northern Niger)	Egalah	435 ± 8 Ma	Single Rb/Sr whole-rock isochron (Karche and Vachette, 1978)	No reported ore deposits
Aïr Massif (northern Niger)	Aroyan and Azambaradan-Tamoelet	426 ± 6 Ma	Single Rb/Sr whole-rock isochron (Karche and Vachette, 1978)	No reported ore deposits
Aïr Massif (northern Niger)	Iskou	427 ± 20 Ma	Single Rb/Sr whole-rock isochron (Karche and Vachette, 1978)	No reported ore deposits
Aïr Massif (northern Niger)	Taghouaji	407 ± 6 Ma 401 ± 5 Ma	Rb-Sr whole rock (Karche and Vachette, 1978) Single Rb-Sr whole-rock isochron (Karche and Vachette, 1978)	Sn-W, Pb-Zn, REE (Perez, 1985, Demaiffe et al., 1991)
Damagaram-Mounio Centre (Southern Niger)	Mounio and Gouré	302 ± 5 Ma 302 ± 9 Ma	Whole rock Rb/Sr Isochron (Bowden et al., 1976)	No reported ore deposits
Damagaram-Mounio Centre (Southern Niger)	Tchouni-Zarniski	330 ± 3 Ma	Rb/Sr syenite and granite whole-rock isochron (Karche and Vachette, 1978)	No reported ore deposits
Damagaram-Mounio Centre (Southern Niger)	Zinder	330 ± 6 Ma	Whole rock Rb/Sr Isochron (Bowden et al., 1976)	No reported ore deposits
Nigerian Younger Granite Province (NYGP): Paleozoic-Mesozoic				
Northern zone	Matsena	258 ± 5 Ma 213 ± 7 Ma	Rb-Sr isochron on arfvedsonite granite (Rahaman et al., 1984) Rb-Sr isochron on aegirine arfvedsonite granite (Rahaman et al., 1984)	No reported ore deposits
Northern zone	Daura	324 ± 2 Ma 322 ± 7 Ma 307 ± 13 Ma	Zircon U-Pb on amphibole syenite (Vincent et al., 2022b) Zircon U-Pb on biotite granite (Vincent et al. (2022b) Rb-Sr isochron on quartz syenite (Rahaman et al., 1984)	No reported ore deposits
Northern zone	Dutse	232 ± 1 Ma 263 ± 3 Ma 230 ± 5 Ma 213 ± 7 Ma	Zircon U-Pb on fayalite syenite (Vincent et al., 2022b) Zircon U-Pb on porph. arfvedsonite aegirine granite (Vincent et al., 2022b) Zircon U-Pb on arfvedsonite aegirine granite (Vincent et al., 2022b) Rb-Sr whole rock on aegirine arfvedsonite granite (Rahaman et al., 1984)	No reported ore deposits
North-eastern zone	Shira	200 ± 1 Ma 199 ± 1 Ma 186 ± 5 Ma	Zircon U-Pb on aegirine arfvedsonite granite (This study) Zircon U-Pb on aegirine arfvedsonite granite (This study) Rb-Sr isochron on aegirine arfvedsonite granite (Rahaman et al., 1984)	No reported ore deposits
North-eastern zone	Kila Massif	232 ± 1 Ma 202	Zircon U-Pb on cpx-amphibole quartz syenite (This study) Zircon U-Pb on	No reported ore deposits

(*continued on next page*)

Table 6 (*continued*)

Province	Complex	Age	Dating method and reference	A-type granite-hosted mineralization
		± 1 Ma	aegirine granite (This study)	
North-eastern zone	Fagam	191 ± 3 Ma	Rb-Sr whole rock on biotite granite	No reported ore deposits
Northern zone	Ningi-Burra	186 ± 2 Ma 192 ± 5 Ma 190 ± 2 Ma 188 ± 1 Ma 192 ± 1 Ma 191 ± 3 Ma 183 ± 7 Ma	Zircon U-Pb on biotite granite (Vincent et al., 2021) Zircon U-Pb on biotite granite (Vincent et al., 2021) Zircon U-Pb on altered granite (Vincent et al., 2021) Zircon U-Pb on altered granite (Vincent et al., 2021) Zircon U-Pb on Zn-bearing quartz vein (Vincent et al., 2021) Zircon U-Pb on Pb-bearing granite (Vincent et al., 2021) Rb-Sr isochron on riebeckite annite granite (Rahaman et al., 1984)	Pb-Zn-Sn (Vincent et al., 2021)
Northern zone	Tibchi	171 ± 3 Ma	Rb-Sr isochron on biotite granite (Rahaman et al., 1984)	Sn-Nb (Kinnaird, 1985)
Northern zone	Banke	173 ± 2 Ma 180 ± 1 Ma	Rb-Sr isochron on biotite granite (Rahaman et al., 1984) Zircon U-Pb on granite porphyry (Vincent et al., 2022a)	Sn-W (Kinnaird, 1981; Vincent et al., 2022a)
Northern zone	Dutsen Wai	173 ± 2 Ma 177 ± 3 Ma 175 ± 3 Ma 178 ± 1 Ma	Rb-Sr isochron on biotite granite (Rahaman et al., 1984) Rb-Sr isochron on biotite granite (Rahaman et al., 1984) Zircon U-Pb on biotite granite (Amuda et al., 2020) Zircon U-Pb on biotite granite (Vincent et al., 2022a)	Nb-Sn (Kinnaird, 1981, Amuda et al., 2020; Vincent et al., 2022a)
Northern zone	Kudaru	175 ± 3 Ma 173 ± 3 Ma 180 ± 1 Ma 178 ± 1 Ma 185 ± 1 Ma	Rb-Sr isochron on biotite granite (Rahaman et al., 1984) Rb-Sr isochron on biotite granite (Rahaman et al., 1984) Zircon U-Pb on fayalite granite porphyry (Kamaunji et al., 2020) Zircon U-Pb on arfvedsonite granite (Kamaunji et al., 2020) Zircon U-Pb on biotite granite (Kamaunji et al., 2020)	Minor Sn (Bain, 1934)
Northern zone	Zaranda	190 ± 10 Ma 186 Ma 203 ± Ma	Rb/Sr Isochron on syenite (Bowden et al., 1976) Rb/Sr Isochron on syenite (Dickin et al., 1991) Zircon U-Pb on aegirine syenite (Ahmed et al., 2021)	
Northern zone	Ririwai	175 ± 5 Ma 176 ± 5 Ma 171 ± 2 Ma 176 ± 2 Ma 171 ± 1 Ma 169 ± 1 Ma 172 ± 2 Ma 181 ± 4 M 188 ± 7 Ma 182 ± 1 Ma 178 ± 5 Ma 179 ± 5 Ma 174 ± 2 Ma	Rb/Sr isochron on arfvedsonite granite (Van Breemen et al. 1975) Rb/Sr isochron on albite riebeckite granite (Van Breemen et al., 1975) Rb/Sr isochron on biotite granite (Van Breemen et al., 1975) Zircon U-Pb on biotite granite (Girei et al., 2019) Zircon U-Pb on biotite granite (Girei et al., 2019) Zircon U-Pb on biotite microgranite (Girei et al., 2019) Zircon U-Pb on arfvedsonite albite granite (Girei et al., 2019) Zircon U-Pb on fayalite granite porphyry (Kamaunji et al., 2023) Zircon U-Pb on arfvedsonite granite (Kamaunji et al., 2023)	Sn-Nb-W-(Pb-Cu-Zn) mineralization (Kinnaird, 1985; Ogunleye et al., 2006; Girei et al., 2019; Kamaunji et al., 2023; Zhu et al., 2024)

(*continued on next page*)

Table 6 (*continued*)

Province	Complex	Age	Dating method and reference	A-type granite-hosted mineralization
			Zircon U-Pb on biotite granite (Kamaunji et al., 2023) Rb-Sr isochron on granite porphyry (Van Breemen et al., 1975) Rb-Sr isochron on albite-riebeck. granite (Van Breemen et al., 1975) Rb-Sr isochron on biotite granite (Van Breemen et al., 1975)	
Northern zone	Guraku	227 ± 2	Zircon U-Pb on porp. arfvedsonite granite (Vincent et al., 2022a)	Barren with potential
Northern zone	Zuku	186 ± 3 Ma	Zircon U-Pb on arfvedsonite granite (Vincent et al., 2022a)	Barren with potential
Central-Jos Plateau	Amo	165 ± 3 Ma 162 Ma 167 ± 3 Ma	Rb-Sr isochron on riebeckite-arfvedsonite granite (Van Breemen et al., 1975) Rb/Sr isochron on biotite granite (Dickin et al., 1991) Rb-Sr isochron on riebeck. biotite granite (Van Breemen and Bowden, 1973)	Nb mineralization (Kinnaird, 1981).
Central-Jos Plateau	Buji	179 ± 0.4 Ma	Zircon U-Pb on arfvedsonite granite (**This study**)	Barren with potential
Central Jos-Plateau	Jos-Bukuru	164 ± 4 161 Ma 178 ± 1 Ma 157 ± 1 M	Rb/Sr isochron on biotite granite (Van Breemen et al., 1975) Rb/Sr isochron on biotite granite (Dickin et al., 1991) Zircon U-Pb on biotite granite (**This study**) Zircon U-Pb on biotite granite (**This study**)	Sn-Nb mineralization (Jacobson et al., 1958; Buchannan et al., 1977; Kinnaird, 1985, this study)
Central-Jos Plateau	Kigom	166 ± 7 Ma	Zircon U-Pb on biotite granite (**This study**)	Mo ± Sn ± Nb (Imeokparia, 1984; Omada, 2000), this study
Central Jos-Plateau	Shere	160 Ma 161 Ma 165 ± 2 Ma	Rb/Sr isochron on arfvedsonite granite (Dickin et al., 1991) Rb/Sr isochron on fayalite granite (Dickin et al., 1991) Rb/Sr isochron on biotite granite (Van Breemen et al., 1975)	Sn-Nb deposits (Kinnaird, 1987)
Central Jos-Plateau	Ropp	162 ± 5 Ma 162 ± 2 Ma 161 ± 2 Ma 149 ± 2 Ma	Zircon U-Pb on biotite granite (Kamaunji et al., 2023) Zircon U-Pb on aegirine biotite granite (Kamaunji et al., 2023) Zircon U-Pb on riebeckite biotite granite porphyry (Kamaunji et al., 2023) Zircon U-Pb on biotite granite (Amuda et al., 2020)	Sn mineralization (Amuda et al., 2020; Kamaunji et al., 2023; Buchannan et al., 1971)
Central Jos-Plateau	Pankshin	151 Ma 151 Ma 154 ± 4 Ma 156 ± 4 Ma	Rb/Sr isochron on biotite granite (Dickin et al., 1991) Rb/Sr isochron on syenite (Dickin et al., 1991) Rb/Sr isochron on syenite (Van Breemen et al., 1975) Rb/Sr isochron on biotite granite (Van Breemen and Bowden, 1973)	–
Southern zone	Mada	145 ± 4 Ma 150 ± 2 Ma 152 ± 1 Ma 160 ± 1 Ma 155 ± 2 Ma	Rb-Sr isochron on biotite granite (Rahaman et al., 1984) Rb-Sr isochron on biotite granite (Rahaman et al., 1984) Zircon U-Pb on biotite granite (Girei et al., 2020) Zircon U-Pb on biotite granite (Girei et al., 2020) Zircon U-Pb on biotite granite (Kamaunji et al., 2024)	Mo-Sn mineralization (Abaa, 1985; Girei et al., 2020; Kamaunji et al., 2024)
Southern zone	Afu	144 ± 2 Ma 149 ± 1 Ma 148 ± 1 Ma	Rb-Sr isochron on biotite granite (Bowden et al., 1976) Zircon U-Pb on biotite granite (Cao et al., 2024) Zircon U-Pb on biotite albite	Sn–W, Zn–Pb–Cu–Mo, Nb–Ta (Imeokparia, 1981; Olade, 1980; Cao et al., 2024)

(*continued on next page*)

Table 6 (*continued*)

Province	Complex	Age	Dating method and reference	A-type granite-hosted mineralization
			granite (Cao et al., 2024)	

Nb ≤ 1910 ppm) are plausible parental melts.

5.3. Physicochemical controls on magma evolution and magma fertility

Zircon saturation thermometry (TZr = 816–1018°C; Crisp and Berry 2022) confirms A-type affinities (>839°C; King et al. 1997; Fig. 13a), with thermal from KGM (940–1018°C) to JBK (830–899°C) to Buji (816–861°C). This gradient reflects sequential melt extraction from metasomatized mantle with crustal cooling during ascent (Bonin, 2007). Polybaric fractional crystallization of Mg-rich olivine, calcic pyroxene, calcic amphibole, feldspars, and Fe-Ti oxides subsequently depleted MgO, CaO, and TiO_2, as shown by inverse SiO_2-MgO/CaO/TiO_2 correlations (Fig. S1a-h).

Zircon fO_2 (Smythe and Brenan 2016) and Ce^{4+}/Ce^{3+} (Ballard et al. 2002; Fig. 13b–c) reveal redox contrasts: JBK zircons ($\log fO_2$ = –25.9 to –11.2; Table S2) span HM-NNNO-FMQ buffers (Fig. 13b–d), while KGM's reduced amphiboles (ΔFMQ = –1) host oxidized zircons ($\log fO_2$ = –18.9 to –15.1), stabilizing sodic amphiboles in ilmenite-series conditions (Anderson and Smith 1995; Fig. 13d). Amphibole classification further distinguishes JBK primary magmatic phases from KGM late-stage growth (Fig. 13e; Czamanske and Wones, 1973). This redox gradient correlates with T-P conditions and emplacement depths, estimated using appropriate geothermobarometric models (Schmidt, 1992; Ridolfi et al., 2010). The JBK calcic amphiboles formed at mid-crustal levels (768–802°C; 2.45–2.87 kbar), while the KGM sodic amphiboles crystallized at shallower depths (658–705°C; 0.87–1.34 kbar) (Table 1), reflecting progressive adiabatic decompression. Crustal interaction modulated differentiation trends, as evidenced by increasing differentiation indices from Buji to KGM (Fig. 13f). Trace element fractionation and progressive magmatic evolution are evident in the studied suites. Ba-Rb-Sr ternary systematics (Fig. 14a) illustrate progressive fractionation along the differentiation spectrum, with plagioclase removal driving Al_2O_3 depletion and negative Eu anomalies. The transition from silica-undersaturated to silica-saturated compositions likely involved AFC processes (Sparks, 1986), with crustal assimilation bridging the thermal divide between silica-undersaturated and silica-saturated compositions (Rogers, 2015).

Late-stage fluid influx in the KGM granites is recorded by the transition from calcic to sodic amphiboles (Fig. 13e; Czamanske and Wones, 1973), interstitial fluorite in the JBK granites, late fluorite-titanite assemblages in KGM, and associated deuteric alteration textures including chloritized biotite, sericitized feldspar, greisenization, and chlorite rims on fluorite (Agemar et al., 1999; Gamal-Adeen et al., 2023). These features collectively indicate volatile-bearing magmatic to hydrothermal activity during the late stages of granite evolution. Additional evidence includes snowball quartz with fayalite rims (Fig. 5l), reflecting volatile-driven crystallization during late stages (Charoy and Raimbault, 1994). However, whole-rock LREE concentrations in KGM (avg. 263 ppm) are lower than in JBK (avg. 428 ppm, Table 3), indicating that metasomatic fluids did not produce net LREE addition. Xenocrystic ~374 Ma zircon (Fig. 10d) records localized crustal assimilation that did not overprint the primary mantle signature, as evidenced by OIB-like zircon trace-element compositions (Fig. 12e–f). Instead, fluid influx redistributed LREEs at the thin-section scale, forming late accessory phases such as fluorite and titanite, without whole-rock enrichment. The petrographic record therefore provides the primary evidence for late-stage fluid activity, whereas the LREE enrichment along the Buji → JBK → KGM differentiation spectrum is best explained by crustal assimilation coupled with feldspar-dominated fractionation.

Using the least differentiated Shira aegirine-arfvedsonite quartz syenite (K3-1; Rb = 62 ppm, Sr = 225 ppm, Rb/Sr = 0.28; Kamaunji et al., 2024) as the parental melt, we modeled whole-rock Sr concentrations and Rb/Sr ratios (Fig. 14b) to track magmatic evolution via fractional crystallization (Ersoy and Helvacı, 2010). The modeling indicates that extracting 40–50 vol% of a crystalline assemblage (~15 vol% K-feldspar, ~13 vol% plagioclase, ~8 vol% amphibole, ~4 vol% fayalite, and ~2 vol% apatite) accounts for the fractional crystallization from JBK (least differentiated) to KGM (highly differentiated) biotite- and arfvedsonite-riebeckite granites (Fig. 14b). This feldspar-dominated fractionation is supported by the systematic depletion of Sr and Ba, coupled with increasing Rb/Sr and strongly negative Eu/Eu* anomalies, all of which are consistent with plagioclase and K-feldspar removal. Importantly, these magmatic trends are preserved despite late-stage fluid influx in KGM, as samples with unambiguous fluid-altered Sr isotopic signatures (< BABI) were excluded from interpretation. We therefore maintain that Sr content and Rb/Sr ratios, when used on samples screened for fluid alteration, are reliable proxies for fractional crystallization.

For JBK, this fractionation is compatible with moderate Pan-African crustal assimilation predicted by the Sr-Nd AFC model. For KGM, however, the same Sr-Nd displacement should be interpreted cautiously because the radiogenic Sr component partly reflects late Rb-Sr disturbance. Thus, AFC processes account for the magmatic differentiation trend, whereas the most radiogenic KGM Sr isotope values record superimposed hydrothermal overprinting rather than proportional increases in bulk crustal assimilation. This feldspar-dominated fractionation (55–65 vol% of total removed material) depletes compatible elements by eliminating mafic/accessory phases, while enriching incompatible elements in the differentiated melt.

5.4. Sn–Nb–Mo mineralization potential: geochemical enrichment signatures

Global enrichment patterns are illustrated in Nb vs. Nb/Ta and Sn vs. Nb plots (Fig. 14c–d). The studied granites exhibit significant Sn (4–126 ppm) and Nb (37–910 ppm) enrichment, exceeding global low-Ca granite (3 ppm Sn, 21 ppm Nb; Turekian and Wedepohl, 1961) (Fig. 14c, d). The JBK biotite-amphibole granite falls within the global range for tin-bearing systems (10–30 ppm Sn; Lehmann, 2021) and approach industrial Nb thresholds (100–150 ppm; Beus and Grigorian, 1977). However, most of the JBK biotite-amphibole granites remain below the regional NYGP tin-fertility benchmark of ≥25 ppm Sn (Olade, 1980; Fig. 14d), indicating weak to moderate Sn enrichment rather than strong Sn mineralization. This contrasts with the more enriched JBK biotite granite reported by Batchelor and Bowden (1986), which contains 126 ppm Sn and ~256 ppm Nb. The comparison highlights the compositional variability within the Jos-Bukuru complex and distinguishes the studied JBK granites from highly evolved NYGP rare-metal granites such as the Ririwai albite-arfvedsonite granite, which contains much higher Nb and Sn concentrations (1160 ppm Nb and 405 ppm Sn; Ogunleye et al., 2006; Fig. 14c; Table S1).

The KGM Mo-arfvedsonite granites are further distinguished by metals (Zn: 654–1326; Pb: 25–1054; Cu: 206–845 ppm; Table 3). Trace-element zoning in KGM granites is captured in Pb vs. Cu and Pb vs. Zn diagrams (Fig. 14e–f). These values exceed those of typical supracrustal Sn-W-Mo granites (Li et al., 2024) but align with global alkaline Sn-Mo-W granites., In Cu-Pb space, KGM samples define a broad high-Cu, high-Pb field, not a linear trend, ruling out simple magmatic differentiation as the sole control on Pb enrichment (Fig. 14e). In Pb-Zn space, Pb varies more widely than Zn, indicating decoupled enrichment (Fig. 14f). This pattern suggests initial magmatic metal concentration followed by Pb remobilization during magmatic-hydrothermal overprint, consistent with trends in Chinese Mo-bearing granites.

A comparative analysis of alkaline-peralkaline granites from key

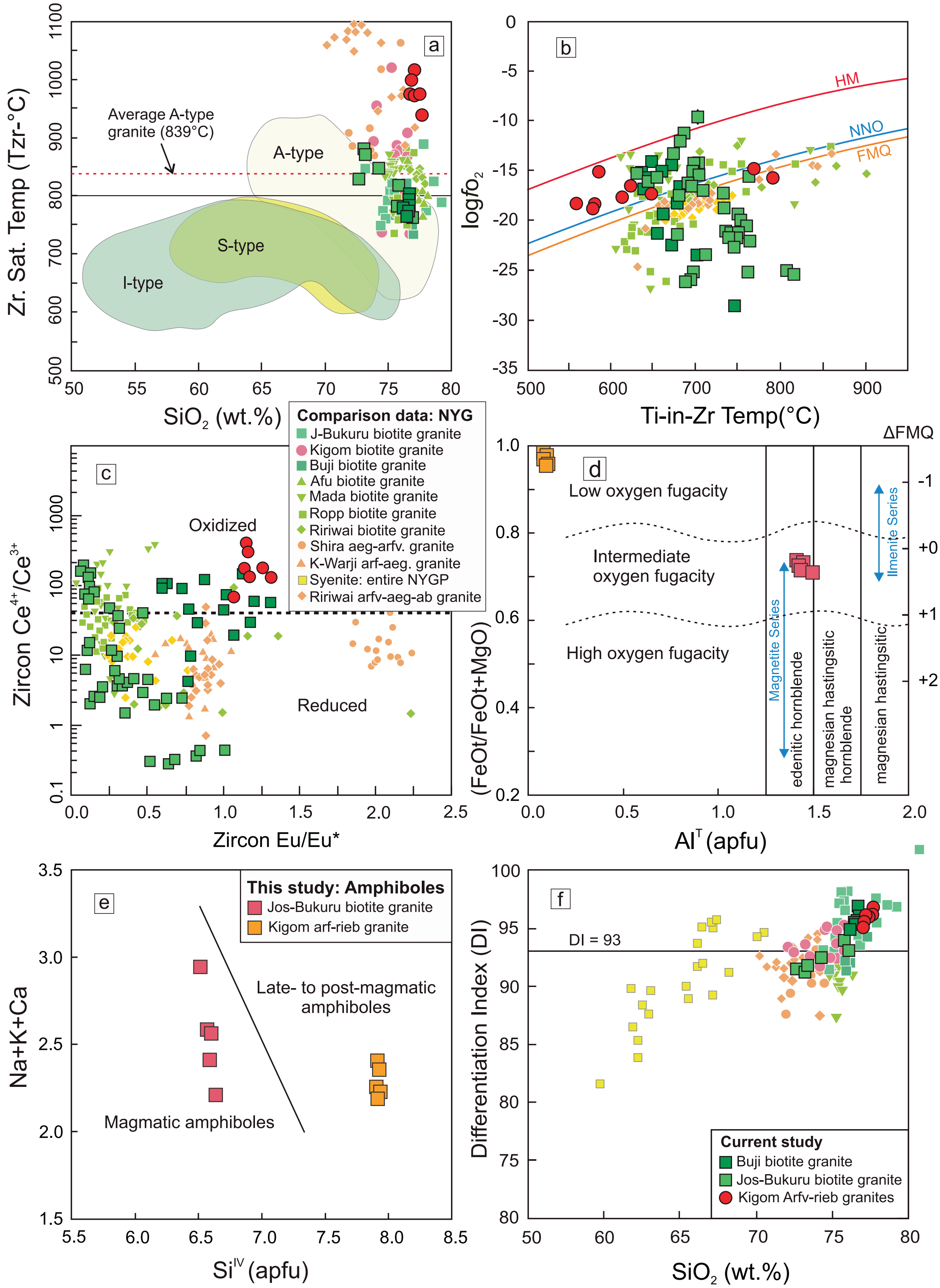

Fig. 13. (a) SiO_2 vs. Zircon Saturation Temperature (TZr); Field for I-, S- and A-type granites are from, and solid line for 800°C line, upper limit for I- and S-type granites are after Collins et al. (2020). Dashed red line represents average TZr (839°C) for A-type granite (after King et al., 1997); (b) Ti-in-Zr temperature vs. $\log fO_2$; (c) Zircon Eu/Eu* vs. Ce^{4+}/Ce^{3+} diagram (after Ballard et al., 2002); (d) Al^T vs Fe# diagram with oxygen fugacity fields of Anderson and Smith (1995); (e) Classification diagram of amphiboles Si^{IV} vs. (Na + K + Ca) with fields defined by Czamanske and Wones (1973); (f) SiO_2 vs. Differentiation index (DI) with highly fractionated field (93) defined by Thornton and Tuttle (1960).FMQ, fayalite-magnetite-quartz buffer (buffer curves after Lindsley and Frost, 1992); HM, haematite–magnetite buffer; NNO, nickel-nickel oxide buffer. Dash line distinguishing reduced and oxidized field was estimated from Ballard et al. (2002). Whole rock comparison data is the same as in Fig. 8.

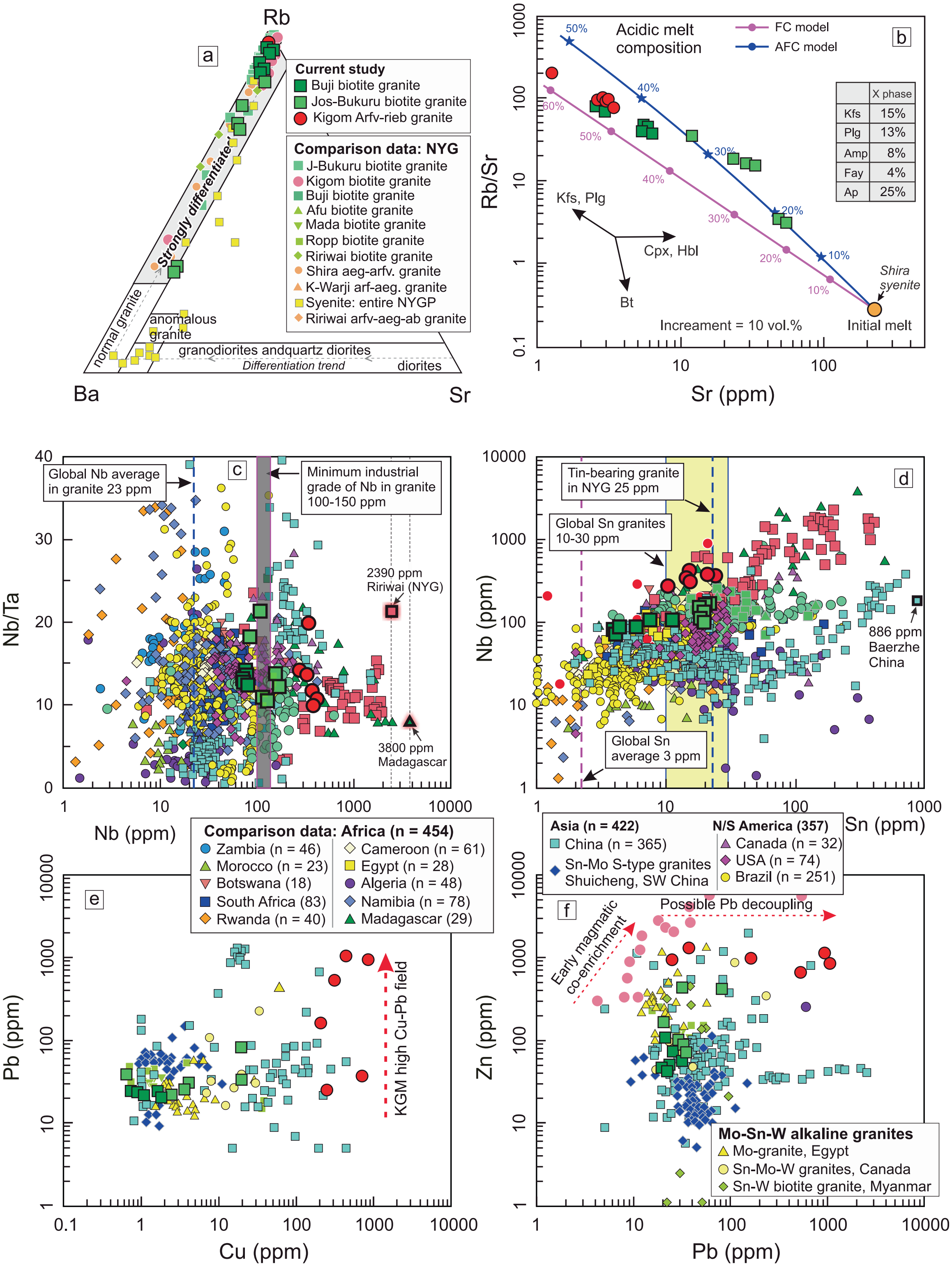

Fig. 14. (a) Ba-Rb-Sr ternary diagram with composition fields and differentiation trends defined by El Bouseily and El Sokkary (1975); (b) Whole-rock Sr vs. Rb/Sr mass-balance modeling for Buji, Jos-Bukuru, and Kigom alkaline granites, showing calculated fractionation trends using the fractional crystallization (FC) model of Ersoy and Helvacı (2010). Solid lines trace melt evolution for FC (pink line) and (2) assimilation-fractional crystallization (AFC; blue line) processes. Ksf = K-feldspar; Plg = plagioclase; Amp = amphibole; Fay = fayalite, Ap = apatite; For Mass-balance Sr-Nd isotope modeling, the initial melt is represented by oceanic island basalt (OIB) from the Benue Trough (Coulon et al., 1996), the intermediate melt by arfvedsonite-aegirine quartz syenite from the Kila-Warji complex (Kamaunji et al., 2023), and the crustal melt by Neoproterozoic Older Granites of eastern and central Nigeria (Dada et al., 1989, 1995; Dickin et al., 1991; Ferré et al., 1998); (c) Nb vs. Nb/Ta variation in the studied granites compared to global mineralized alkaline granites (references in Table S3); (d) Sn vs. Ta variation in the studied granites compared to global mineralized alkaline granites (references in Table S3). Global industrial Nb thresholds (100–150 ppm; Beus and Grigorian, 1977); global Sn-Nb background averages in low-Ca granites (Turekian and Wedepohl, 1961); global tin-granite threshold (Lehmann, 2021); and NYGP tin granite averages (Olade, 1980); (e-f) Metal covariation plots showing: (e) Cu vs. Pb and (f) Pb vs. Zn relationships in the studied granites compared to Sn-Mo-W alkaline granites (Egypt, Canada, Myanmar) and Sn-Mo S-type granites (Shuicheng, SW China; references in Table S3. Whole rock comparison data is the same as in Fig. 8.

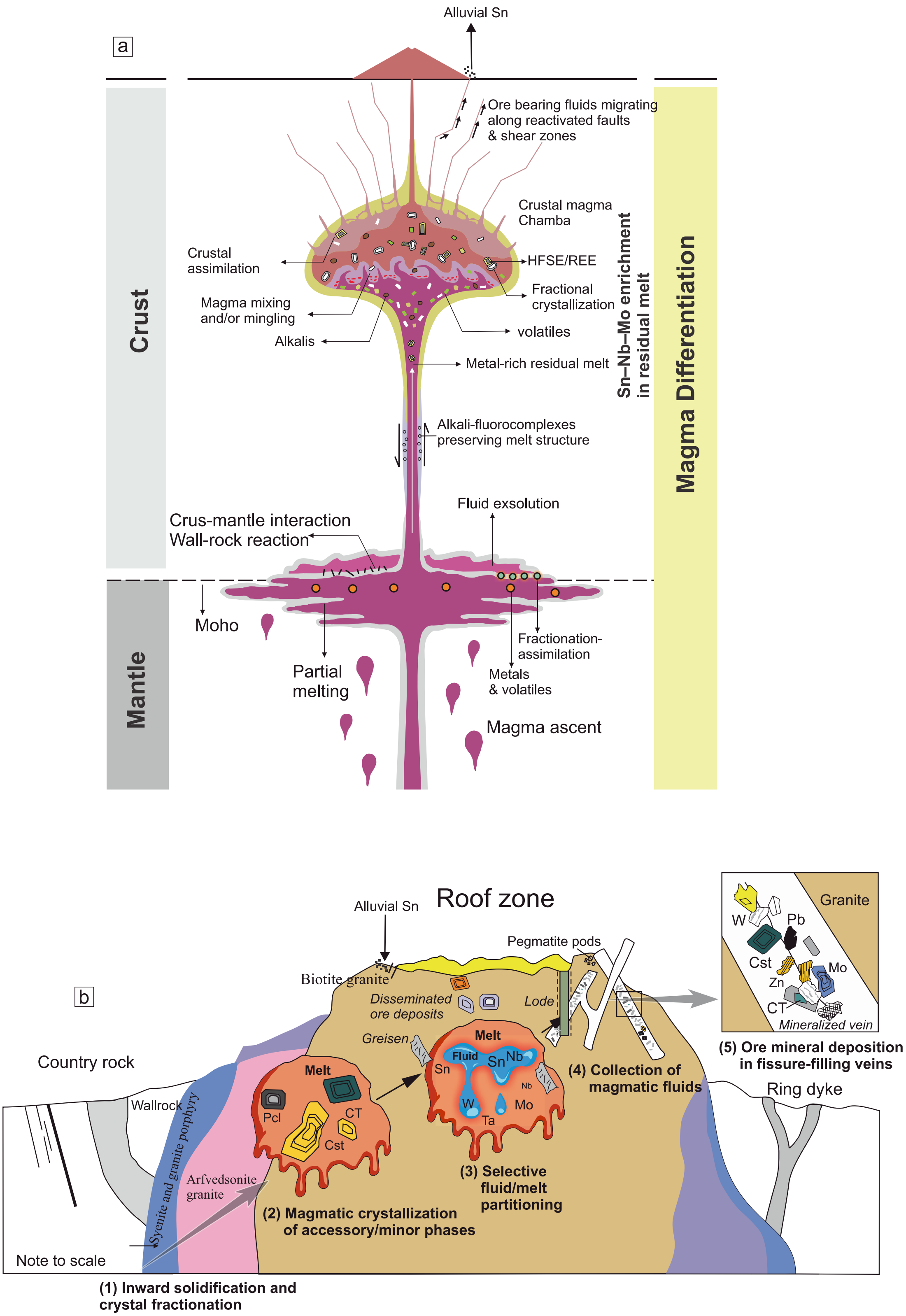

Fig. 15. Metallogenic model for Sn-Nb-Mo enrichment and deposition: **(a)** Conceptual diagram of magma differentiation and metal deposition in the Jos-Plateau Tin Belt showing stages of magma crystallization, fluid exsolution, and metal enrichment. Key processes include the formation of alkali-fluorocomplexes, migration of ore-bearing fluids, and Sn-Nb-Mo deposition along fractures, with fluid-rock interactions leading to ore formation; **(b)** A four-stage metallogenic model for Sn-Nb-Mo mineralization in the Jos-Plateau Tin Belt. The model integrates: (A) Stage I – Magmatic crystallization and early enrichment with inward solidification and source-dependent metal partitioning; (B) Stage II – Magmatic-hydrothermal transition via fluid exsolution, showing early Kigom molybdenite vs. refractory Jos-Bukuru Sn-Nb; (C) Stage III – Hydrothermal veining, contrasting Kigom's molybdenite stockworks with Jos-Bukuru's shear zone-hosted greisen lodes; and (D) Stage IV – Post-mineral placer development, illustrating supergene formation of alluvial Sn-Nb placers and residual Mo in veins.

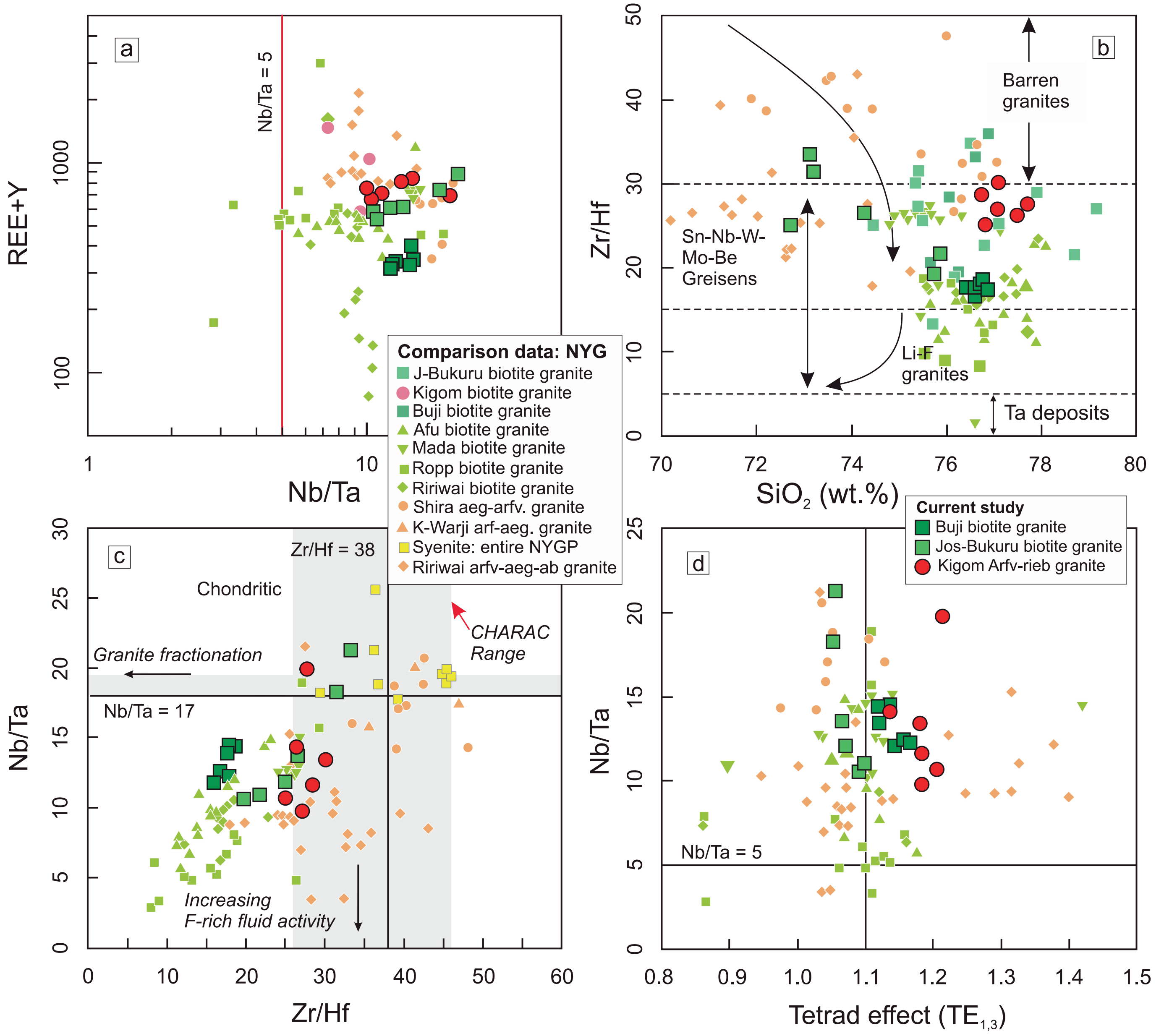

Fig. 16. (a) Nb/Ta vs. REE + Y; (b) SiO_2 vs. Zr/Hf after (Zaraisky et al., 2009); (c) Zr/Hf vs. Nb/Ta; (d) tetrad-effect ($TE_{1,3}$) vs. Nb/Ta. Defined boundaries include: tetrad effect (TE = 1.10; Irber, 1999), CHARAC/non-CHARAC divisions (Bau, 1996; Green and Pearson, 1987); Nb/Ta = 5 (Ballouard et al., 2016). Whole rock comparison data is the same as in Fig. 8.

global provinces (Table S4) reveals distinct enrichment patterns. The pyrochlore-bearing granites of Madagascar represent the world's most Nb-enriched systems (~3800 ppm Nb, Fig. 14c), attributed to extreme fractionation in F-rich melts (Estrade et al., 2014a,b). Nigeria's Ririwai granite shows analogous high-Nb affinity (2390 ppm; Ogunleye et al., 2006; Fig. 14c; Table S1), positioning Nigeria as an emerging Nb province of global significance. Myanmar's Wagone alkaline granites are notable exception, with one of the world's highest reported Sn concentrations (2073 ppm) despite minimal Nb (17 ppm; Li et al., 2018; Table S4). Beyond Africa, the Jos Plateau shares key similarities with the Pitinga Sn–Nb–Ta province (Amazonian Craton, Brazil). Its Paleoproterozoic (ca. 1.82 Ga) Madeira and Água Boa A-type granites host world-class Sn-Nb-Ta-F-(Y-REE-Li) mineralization, with strong incompatible element enrichment and F-rich volatile phases (Costi et al., 2002, 2009; Bastos Neto et al., 2009). Similarities include: (1) a peralkaline cryolite-bearing core and metaluminous fluorite-bearing border (Costi et al., 2009; Hadlich et al., 2024), mirroring the peralkaline-to-metaluminous transition in KGM; (2) extreme enrichment in F, Na, Sn, Nb, Ta, Zr, Th, Y, Rb, REE in Pitinga's albite-rich facies (Costi et al., 2009; Borges et al., 2021), comparable to KGM's extreme Nb (910 ppm), Sn (126 ppm), Zn (1326 ppm), Pb (1054 ppm), low Zr/Hf (<30), and high Nb/Ta (>5); (3) F-rich melt evolution via immiscibility and dense F-rich peralkaline phase (Costi et al., 2009; Bastos Neto et al., 2009), paralleled by KGM's fluorite-astrophyllite assemblages and sodic amphiboles; and (4) hydrothermal alteration of pyrochlore by F-rich fluids causing U enrichment (Hadlich et al., 2024), analogous to fluid-mediated Sr metasomatism and Pb redistribution in KGM. Thus, Pitinga demonstrates that F-rich A-type alkaline granites can host economic critical metals, and the Jos Plateau represents the closest geochemical and metallogenic analogue outside Africa (Costi et al., 2009; Hadlich et al., 2024).

Alluvial cassiterite (Fig. 7i) sourced from Sn-mineralized Daw granite, and hybridized contacts between KGM-Ganawuri/JBK regions indicate significant regional exploration potential. The presence of alluvial cassiterite, despite low bulk-rock Sn concentrations (~19.58 wt %), is explained by a two-stage magmatic-hydrothermal model. Mantle-derived melts first supplied heat and volatiles to drive crustal assimilation and fractional crystallization, establishing an initial Sn endowment (Zhao et al., 2025). Subsequently, late-stage F-rich fluids in apical cupolas scavenged Sn from wall rocks and precipitated cassiterite in veins via Cl/F complexation and P-T-X-controlled deposition (Liu et al., 2023; Mathur et al., 2025).

5.5. Metallogenic model for Sn-Nb-Mo enrichment and deposition

A four-stage genetic model explains the distinct Sn–Nb (JBK) and Mo (KGM) mineralization, integrating contrasting source signatures, fluid pathways, and the key role of fluorine in metal complexing and transport (Fig. 15a, b).

Stage I: Magmatic enrichment

Magmatic enrichment began with the mixing of redox-heterogeneous melts that ponded and interacted at the Moho boundary, where early fractionation and crust-mantle reaction concentrated incompatible elements and volatiles (Fig. 15a). Fluorine was introduced via melting of F-rich mantle amphibole (Manthilake et al., 2021). These enriched melts ascended through a focused transcrustal conduit (Fig. 15a), undergoing progressive differentiation before stalling in upper-crustal chambers. Here, fractional crystallization of the JBK and KGM granites (Fig. 15a) led to inward solidification, concentrating evolved, biotite- and amphibole-rich melts in the apical zones (Fig. 15b). In JBK, magma mingling drove AFC, where mafic melts facilitated crustal assimilation and protracted Sn-Nb fractionation (Vasyukova and Williams-Jones, 2020). This protracted magmatic evolution is reflected in the crystallization of JBK calcic amphiboles at higher temperatures and pressures (768–802°C; 2.45–2.87 kbar) under intermediate oxygen fugacity (FMQ 0 to +1). These conditions are consistent with primary magmatic growth in a deeper, hotter reservoir, analogous to conditions reported for other alkaline magmatic systems (Bonin, 2007; Dall'Agnol et al., 2012).

At KGM, oxidized mantle melts supplied Mo and volatiles via fluxing (Guo and Audétat, 2017), acting as both a metal carrier and a heat source to extend the chamber's lifetime and promote extreme crystallization (Audétat and Li, 2017; Girei et al., 2020). This late-stage, shallow evolution is recorded by KGM sodic amphiboles, which crystallized at lower P–T conditions (658–705°C; 0.87–1.34 kbar) under more reduced conditions (FMQ −1 to +1) (Fig. 13d) and show a stronger F^- preference, marking advanced volatile enrichment. The resulting highly alkaline, F-rich compositions stabilized metal-fluorocomplexes (Ballouard et al., 2020). Ultimately, extreme fractionation formed volatile-rich melt pockets in the apical zone, enabling the early magmatic crystallization of Sn-Nb-bearing accessory minerals (e.g., cassiterite, columbite) directly from the silicate melt (Fig. 15b).

Stage II: Magmatic-hydrothermal transition

Volatile and metal-rich fluids in the JBK and KGM system exsolved from the crystallizing melts during the transition from late magmatic fractionation to hydrothermal activity. This transition reflects volatile saturation in highly evolved residual melts, followed by separation of F-rich, metal-bearing fluids. These fluids accumulated in structural traps beneath the intrusion roof. Localized overpressure from this accumulation promoted the development of pegmatite pods and the initial fracture networks that preconditioned the rock for later vein formation (Fig. 14b).

During this transition, fluorine was preferentially incorporated into fluorite and CaF_2-rich calcic amphiboles relative to other hydrous silicates (Scaillet and Macdonald, 2004; Dolejš and Baker, 2006). Fluorite from the JBK granites has high CaO (66.22–70.77 wt%) and F (54–56 wt %), with negligible SiO_2 and Al_2O_3, consistent with a magmatic-hydrothermal origin and limited silicate contamination. Elevated Na_2O and trace P_2O_5 further indicate interaction with alkali-rich fluids or residual melts, consistent with F complexing with alkalis (Dolejš and Baker, 2004; Shapovalov et al., 2019). Under reduced to moderately oxidized conditions, fluorine formed stable fluoro-complexes with Sn, Nb, and Mo, significantly enhancing their solubility and mobility (Agangi et al., 2010; Williams-Jones and Vasyukova, 2023). This contrasts with the Gindi Akwati Sn system, where a single-stage, chloride-dominated greisenization event liberated Sn from hot, low-moderate salinity fluids exsolving directly from the crystallizing melt (Amuda et al., 2022). In the KGM Mo system, high-temperature, saline, oxidized fluids likely transported Mo as molybdate species (e.g., as $HMoO_4^-$), with deposition in potassic-altered zones driven by cooling, fluid-rock interaction, or redox changes (Audétat and Li, 2017). This stage, also marked by biotite replacement by chlorite and pervasive silicification, contrasts with the JBK Sn-Nb system, where metals remained sequestered in evolved melt and accessory phases, requiring a later or more localized fluid overprint for efficient liberation.

Trace-element systematics (Fig. 16a–d) indicate a progression from magmatic differentiation to magmatic-hydrothermal overprinting. All three suites have Nb/Ta ratios >5, distinguishing them from low-Nb/Ta Ta-deposit trends and showing that Nb remained an important component of the residual melts (Bau, 1996; Claiborne et al., 2006). Their low Zr/Hf ratios, Buji = 16.7–18.5, JBK = 19.3–33.6, and KGM = 25.3–30.1, are below chondritic values of ~36–38 and are consistent with evolved A-type to NYF-type granite systems (Zaraisky et al., 2009). Buji has the lowest Zr/Hf values, JBK shows the widest range, and KGM clusters within the evolved granite to greisen-related field, indicating increasing fluid influence in the most evolved system.

The tetrad-effect data further distinguishes magmatic from fluid-controlled REE fractionation. Buji and KGM both show strong $TE_{1,3}$ values, Buji = 1.11–1.16 and KGM = 1.14–1.21, whereas JBK shows weaker values of 1.05 to 1.10 (Table 3; Fig. 16d). However, Buji lacks hydrothermal assemblages such as fluorite, astrophyllite, sodic amphiboles, and fluid-mediated Sr overprinting. Its strong tetrad effect, together with low Zr/Hf and high Rb/Sr, is therefore interpreted as the product of advanced magmatic fractionation in a highly evolved crustally enriched melt (Irber, 1999; Jahn et al., 2001; Shuai et al., 2021). In contrast, KGM combines strong tetrad effects with fluorite-astrophyllite assemblages, sodic amphiboles, and Sr isotope disturbance, indicating REE modification by late F-rich magmatic-hydrothermal fluids (Bau, 1996; Irber, 1999; Monecke et al., 2011).

JBK occupies an intermediate position. Its weaker tetrad effects and variable Zr/Hf ratios suggest dominantly magmatic control with limited fluid involvement. Although fluorite indicates some fluid activity, the weak tetrad effect and lack of pervasive replacement textures suggest that fluid interaction was restricted. Therefore, JBK LREE enrichment is attributed mainly to assimilation of LREE-rich upper crustal components rather than pervasive metasomatic fluid influx. Overall, the data record a transition from dominantly magmatic HFSE enrichment in Buji, through limited fluid interaction in JBK, to the clearest magmatic-hydrothermal overprint in KGM, where F-rich fluids modified REE behavior, disturbed the Rb-Sr system, and helped prepare the system for later Mo-bearing stockwork mineralization.

Stage III: Hydrothermal veining and stockwork formation

Fluid flow became structurally focused at roof zones (Fig. 15b). The migration of these acidic, F-rich fluids through fractures and shear zones was likely the key mechanism for upgrading mineralization, analogous to pyrochlore deposits in Ririwai complex (Zhu et al., 2024). At KGM, molybdenite deposition progressed to form extensive quartz-molybdenite stockworks, consistent with the greisen-related stockwork veins reported in the Mada Mo system (Girei et al., 2020). At JBK, Sn-Nb mineralization was confined to shear zone-bound greisen lodes, a structural control fundamental to regional Sn deposits like Gindi Akwati, where mineralization is strictly bound to younger shear zones (Amuda et al., 2022). Deposition was likely triggered by fluid-rock interaction and neutralization, where a resultant pH increase destabilized metal-fluoro complexes to precipitate ore minerals in veins and stockworks (Fang et al., 2025). This process is evidenced by chlorite and K-feldspar

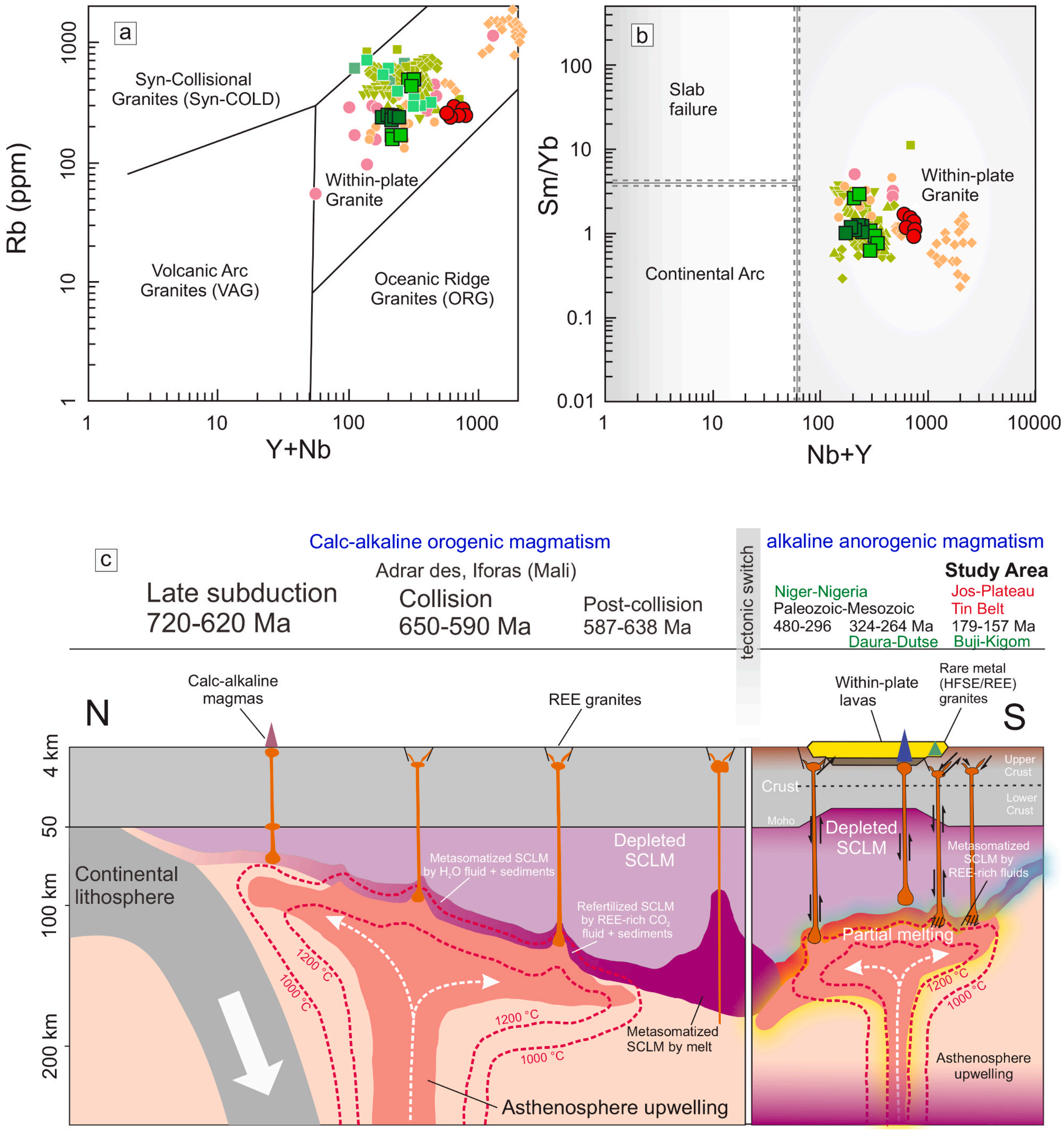

Fig. 17. Tectonic implications (a) Y + Nb vs. Rb (after Pearce et al., 1984), (b) Nb + Y vs. Sm/Yb (after Whalen and Hildebrand, 2019). (c) Regional tectonic model showing the transition from Pan-African orogenic magmatism to Paleozoic-Mesozoic anorogenic alkaline magmatism in the Niger-Nigeria Igneous Province. The model includes subduction (720–620 Ma), collision (650–590 Ma), post-collision magmatism (587–638 Ma), and intraplate alkaline magmatism in Niger (480–296 Ma), Nigeria (324–141 Ma), and the Jos Plateau Tin Belt (179–157 Ma). It also shows the inferred involvement of metasomatized subcontinental lithospheric mantle (SCLM), asthenospheric upwelling, and partial melting in the generation of alkaline granites. The vertical scale indicates depths of 4–200 km, and the adiabatic temperature gradient is 1000–1200°C after Hou et al. (2023).

alteration halos. Structurally controlled dilatant zones likely provided the essential pathways for ore deposition (Chauvet, 2019).

Stage IV: Supergene weathering & placer formation

Supergene weathering formed placer deposits through (1) proximal concentration from eroded high-grade lodes and (2) distal dispersal from weathered disseminated mineralization. This resulted in rich alluvial tin-columbite placers at JBK and localized cassiterite gravels at KGM. In contrast, molybdenum remains in primary bedrock deposits due to its weathering resistance. This is consistent with the inference from Gindi Akwati (Amuda et al., 2022) that surficial redox processes can alter the apparent abundance of oxide versus sulfide ores.

5.6. Tectono-geodynamic implications and metallogenic control

5.6.1. Regional tectonic framework

The Pan-African Orogeny (650–570 Ma) assembled western Gondwana, and established the lithospheric architecture that later controlled Phanerozoic alkaline magmatism in north-central Africa (Veevers, 2003;

Bowden et al., 1987). This evolution involved early rifting, oceanic spreading, subduction and final collision between the West African Craton, Tuareg Shield and Benino-Nigerian Shield between ca. 720 and 590 Ma (Moussine-Pouchkine and Bertrand-Sarfati, 1978; Liégeois et al., 1987; Fowler and Hamimi, 2024). Collision and transpression generated long-lived N-S to NNE-SSW lithospheric shear zones, which became the principal crustal weaknesses subsequently exploited by post-orogenic and anorogenic magmatism.

In East-Central Nigeria, oblique collision and subsequent lithospheric delamination along the Patos-8°30′ shear system promoted syn- to post-collisional magmatism between ca. 638 and 587 Ma, including A2-type and calc-alkaline plutons (Goodenough et al., 2014; Bute et al., 2019). These Pan-African structures did not directly generate the Jurassic Younger Granite complexes, but they provided the inherited structural template for later magma ascent, ring-complex emplacement and mineralization. Later changes in regional stress regime, dyke emplacement and crustal extension enabled the transition from post-collisional magmatism to classical A1-A2 anorogenic alkaline ring complexes (Liégeois et al., 1987).

5.6.2. *West African anorogenic alkaline province*

Across western and north-central Africa, inherited Pan-African shear zones were repeatedly reactivated during intracontinental extension and acted as conduits for alkaline and peralkaline magmatism (Black and Liégeois, 1993; Liégeois et al., 2005). Comparable structural control is recorded in the Aïr Massif, Niger, the Hoggar province, Algeria, and parts of the Nubian Shield, where post-orogenic lithospheric thinning favoured emplacement of anorogenic ring complexes enriched in HFSEs, REEs, Sn, Nb and U (Bowden et al., 1987; Liégeois et al., 1994; Bonin, 2007). The Nigerian Younger Granite Province therefore represents one segment of a broader West African to north-central African belt of post-orogenic alkaline magmatism localized along reactivated Pan-African structures. In the Niger-Nigeria alkaline province, anorogenic magmatism developed mainly during the Paleozoic to Mesozoic, with ages ranging from ca. 487 to 141 Ma (Fig. 1a, b). Following Pan-African collision at ca. 620–590 Ma, prolonged lithospheric stabilization and thermal relaxation prepared the crust and lithospheric mantle for later extension-related magmatism (Liégeois and Black, 1987; Jaupart and Mareschal, 2021). Subsequent reactivation of inherited structures promoted dyke swarms, rhyolitic volcanism and emplacement of alkaline-peralkaline ring complexes at shallow crustal levels (Liégeois and Black, 1987; Liégeois et al., 2013). This tectonic inheritance is central to the metallogenic interpretation because the same structures that focused magma ascent also localized late magmatic-hydrothermal fluid flow.

5.6.3. *Age progression and tectonic control in north-central Nigeria*

After a long interval of post-Pan-African stability, silica-oversaturated alkaline ring complexes were emplaced in an anorogenic setting, as supported by Rb versus Y + Nb and Sm/Yb versus Nb + Y discrimination diagrams (Fig. 17a-b). The province shows a broad age progression from Daura (ca. 324 Ma) to Afu (ca. 141 Ma), with the studied complexes falling within this trend: Buji at 179.3 ± 0.44 Ma, JBK at ca. 168 Ma and KGM at 166.4 ± 6.8 Ma (Fig. 1b).

This age pattern is best explained by episodic magma emplacement along intersecting ENE-WSW and NNW-SSE strike-slip faults linked to older N-S lithospheric shear zones (Rahaman et al., 1984; Black and Liégeois, 1993). A pre-Late Jurassic transition from compression to extension, probably related to changes in plate motion, generated oblique-slip faults that acted as magma conduits (Black et al., 1985; Guiraud et al., 2005). This fault-controlled model accounts for both the spatial clustering and diachronous emplacement of the complexes. The plume model is less consistent with the Nigerian Younger Granite Province because the complexes are concentrated in a narrow 50–100 km belt, show slow apparent age-progression rates of ca. 0.34–0.5 cm/yr, and follow inherited continental structures rather than a broad hotspot track (Wright, 1973; Bowden et al., 1976; Shellnutt et al., 2009; Kamaunji et al., 2020; Vincent et al., 2022a,b). The north–south alignment of progressively younging magmatism is therefore better attributed to reactivation of lithospheric weaknesses along craton-margin structures than to migration over a stationary mantle plume, as summarized in the tectono-magmatic model in Fig. 17c (Rahaman et al., 1984; Bailey and Woolley, 2005; Girei et al., 2019; Amuda et al., 2020; Ahmed et al., 2021; Vincent et al., 2022a,b; Kamaunji et al., 2022b, 2023, 2024; Hassan et al., 2025).

5.6.4. *Magma generation, ascent and control on Sn-Nb-Mo mineralization*

Lithospheric thinning and fault reactivation promoted asthenospheric upwelling, adiabatic decompression melting, and partial melting of metasomatized SCLM beneath the study area (Fig. 17c). The resulting alkaline magmas were enriched in HFSEs and REEs, but volatile enrichment and magmatic-hydrothermal evolution were not uniform across the studied complexes. Buji lacks magmatic fluorite and other F-rich assemblages, which suggests that it did not preserve a well-developed F-rich magmatic-hydrothermal stage. In contrast, JBK records localized fluorite-bearing assemblages and alteration, whereas KGM contains sodic amphiboles, astrophyllite, late fluorite-titanite-zircon assemblages, greisenized zones and molybdenite stockworks. The Buji-JBK-KGM sequence is therefore interpreted as a combined source, fractionation and hydrothermal-evolution trend rather than a simple monotonic increase in volatile content.

Ore formation was controlled by the interaction between magma fertility, fractionation and structural permeability. Transtensional extension and asthenospheric input generated oxidized, mantle-influenced melts capable of transporting Mo in soluble high-valence complexes during fluid exsolution (Kocatürk et al., 2025; Heinrich, 2024). Within fault-bounded magma chambers, prolonged fractional crystallization and assimilation-fractional crystallization concentrated Sn, Nb, Mo and REEs in residual melts and late fluids (Kinnaird, 1985; Yin et al., 2022). Recurrent fault reactivation then promoted episodic fluid exsolution and channelized flow of metal-bearing hydrothermal fluids along fractures, shear zones and cupola margins (Audétat and Edmonds, 2020).

This evolution produced a subvolcanic magmatic-hydrothermal system comparable to classical mineralized ring complexes in the Nigerian Younger Granite Province (Buchannan et al., 1971; Kinnaird, 1984, 1985; Kinnaird et al., 2016). Although the system shares features with highly evolved rare-element pegmatites, including extreme fractionation and F-rich residual fluids (Melcher et al., 2017; London, 2018), it is distinguished by shear-zone-bound greisen lodes, molybdenite stockworks, quartz veins and alluvial placer mineralization (Kinnaird, 1985; Kinnaird et al., 2016). Nigerian examples such as Ririwai, Dutsen Wai-Ropp and Mada show that rare-metal fertility in A-type to peralkaline granites reflects the combined effects of evolved alkaline magmas, variable crustal input and late magmatic-hydrothermal modification (Girei et al., 2019, 2020; Amuda et al., 2022; Kamaunji et al., 2023). Comparable ring-complex systems in the Aïr province, Niger, further show that transtensional shear zones can control both emplacement and mineralization (Moreau et al., 1994; Bowden et al., 1987; Fowler and Hamimi, 2024).

5.6.5. *Global metallogenic analogues and Sn-Nb-Mo mineralization controls in alkaline systems*

The Timedjelalen ring complex in Mali (ca. 600 Ma) is structurally comparable to the Nigerian Younger Granite complexes but lacks significant Sn-Nb-Mo mineralization (Weis et al., 1986). This contrast shows that alkaline magmatism and intracontinental extension are permissive, but not sufficient conditions for ore formation. Fertility requires the convergence of source fertility, favourable redox state, F-Cl-H_2O enrichment, advanced fractional crystallization and assimilation-fractional crystallization, magmatic-hydrothermal fluid exsolution and structural focusing. In this framework, The Jos Plateau therefore represents a mineralized metallogenic end-member. Here, intracontinental

Table 7
Comparison of Sn-Nb-Mo mineralization in alkaline/peralkaline granites from the Jos Plateau (Nigeria) and global analogues, highlighting key tectonic settings, magmatic processes, metal associations, and diagnostic signatures.

S/N	Province / Study	Tectonic Setting	Magma Source	Key Metallogenic Process	Metal Association & Style	Diagnostic Signature
*	Jos-Plateau, Nigeria (This Study)	Intracontinental transtension; reactivated shear zones.	Hybrid mantle-crust: Metasomatized SCLM + crustal assimilation (AFC).	1. Mantle-crust hybridization & AFC. 2. Late-stage, F-rich magmatic-hydrothermal fluid exsolution focused along structures.	Sn-Nb-Mo ± W, Zn, Pb. Styles: Greisen lodes, stockwork veinlets (Mo), quartz veins, and alluvial placers.	Isotopic decoupling (juvenile εNd(t) vs. radiogenic $^{87}Sr/^{86}Sr$ (i)); high Rb/Sr, low Sr/Y; strong REE tetrad effects in most evolved phases; mineralization controlled by shear zones/fractures.
1	Niger Alkaline Province (Bowden et al., 1987)	Anorogenic, sub-volcanic ring complexes.	Mantle-derived, bimodal (basalt + peralkaline rhyolite)	Fractional crystallization in bimodal magma chambers; uranium deposition in coeval sedimentary basins.	U (dominant), Sn, Nb, (Pb-Zn); disseminated & greisen veins; spatially associated with gabbro-anorthosite suites.	Spatial association with Phanerozoic anorthosites; peralkaline ignimbrites; uranium in volcanics & sandstones.
2	Sabaloka (Sudan) (Almond, 1967, 1977)	Anorogenic sub-volcanic ring complex	Not detailed in sources, but complex shows affinities to West African Younger Granites.	Hydrothermal fluids from a biotite-muscovite granite forming stockwork and greisen lenses	Sn-W (dominant), minor Mo, Pb, Zn, etc.; quartz vein stockwork and greisen lenses	Sn-W dominant; dominantly acidic complex with rhyolitic ignimbrites; largely lacking peralkaline rocks
3	Zaaiplaats, South Africa (Vonopartis et al., 2020)	Intraplate (Bushveld Igneous Complex).	Crustal (Extreme in situ fractional crystallization of a parental A-type granite (Nebo) within the crust).	Extreme fractional crystallization forms a volatile-rich cupola, transitioning to F-rich magmatic-hydrothermal fluids causing greisenization and alteration.	Sn (Cassiterite) dominant. Style: Disseminated, in miarolitic cavities, and within large hydrothermal tourmalinized/greisenized pipes in the granite roof.	Low Zr/Hf, anomalous Nb/Ta, high LILE & HFSE, with granophyric texture, microclinization, chloritization, and pipe structures, indicate the magmatic-to-hydrothermal transition in a single pluton.
3	Saudi Arabia (Moghazi et al., 2015; Aseri, 2020; Abuamarah, 2020; Gahlan et al., 2022)	Post-collisional/ within-plate	Juvenile crustal (partial melting) with a mantle heat/fluid contribution	Extreme fractional crystallization enriches the residual melt, and the transition to the hydrothermal stage is key for metal redistribution.	HFSE (Nb, Ta, Zr, Hf), REE, Sn, U, Th. Styles: Disseminated, in pegmatites, quartz veins, and hydrothermally altered (e.g., hematized) granite	Peralkaline to alkaline geochemistry; positive Nb-Ta anomaly; tetrad REE patterns indicating F-rich fluid interaction
4	Climax, USA (Audétat, 2015)	Within-plate, anorogenic.	Predominantly crustal, with evidence of mafic recharge.	Extreme fractionation & efficient apical focusing of F-rich melts/fluids	Mo-dominant; classic porphyry stockwork.	High-F, topaz-rhyolite affinity; melt inclusions with 5–7 μg/g Mo, ~100 μg/g Mo in fluids.
5	Mayo Darlé/Darley, Cameroon (Tantoh et al., 2024; Lavenir et al., 2023)	Within-plate, anorogenic (Cameroon Volcanic Line).	Predominantly mantle-derived (A1-type granite), with multi-stage subsolidus hydrothermal overprint.	High-T (~800°C) crystallization + complex, multi-stage hydrothermal fluid reactions (albitization, greisenization).	Sn-dominant, with Sn–Hf–Zr and Sn–Tl–Nb associations; cassiterite-quartz-muscovite stockwork & greisen.	A1-type granite affinity overlapping with OIB field; complex rock suite (acidic to basic); high-temperature formation.
6	Emeishan, China (Shellnutt et al., 2009)	Mantle plume (intraplate).	Pure mantle: Enriched mantle plume (OIB-like).	Extreme fractional crystallization.	Nb-Zr-REE; magmatic.	High + εHf(t)/+εNd(t); mantle-like trace element ratios.
8	Gattar, Egypt (Feteha et al., 2022)	Post-collisional extension (ANS).	Hybrid crust-mantle: Metasomatized juvenile crust + mantle fluids.	Fractional crystallization-dominated + fluid interaction.	Mo; evolved granite cupola & veins.	High fO_2; decreasing Zr/Hf with fractionation.
9	Duolongqiarou, China (Guo et al., 2022)	Syn-collisional; slab break-off.	Crust-mantle mix: Ancient lower crust + significant mantle input.	Extreme crystal fractionation in hydrous magma.	Mo-dominant; porphyry veins/stockwork.	Coupled, slightly negative εNd (t) & εHf(t); strong negative Eu anomaly.
10	Keivy, Russia (Zozulya et al., 2022)	Anorogenic alkaline province (Archean).	Mantle/Juvenile crust.	Fluid-dominated pegmatite evolution + upper crust assimilation.	Partitioned: Zr-REE-Nb (granite) / Ta-Hf-Y-HREE (pegmatite).	Nb/Ta & Zr/Hf < 1 in pegmatite minerals; agpaitic to miaskitic transition.
11	Rondônia, Brazil (de Almeida et al., 2024)	Intraplate, anorogenic; terminal stages of orogenic cycles.	Predominantly crustal (A2-type): Partial melting of continental crust.	Extreme fractionation of crustal melts + greisenization.	Sn-Nb-Ta-W; classic greisen deposits.	Highly evolved, high Rb signature; intraplate geochemistry.
12	Strange Lake Pluton, Canada (Salvi and Williams-Jones, 1990; Siegel et al., 2017, 2018)	Anorogenic, intracontinental rift extensional setting	Hybrid: Primarily a subcontinental lithospheric mantle source, fertilized by earlier subduction, with significant crustal contamination.	Fractional crystallization enriches the melt in REE, Zr, and Nb, followed by LREE-fluoride melt exsolution and hydrothermal upgrading.	Zr-Nb-REE. Magmatic pre-enrichment with hydrothermal ore zones in pegmatite cores and altered granite.	Hyper-enrichment in HFSE, miaskitic to agpaitic transition negative εNd & elevated δ^{18} indicating crustal input, and complex Ca-Na-REE metasomatic assemblages
13	Bokan Mountain, USA (Dostal et al., 2014, Dostal, 2023)	Anorogenic continental rift (extension-related).	Metasomatized lithospheric source (mantle or lower crust), enriched by prior	Low-degree partial melting and fractional crystallization create a peralkaline melt, with late-stage F-rich fluids	U-Th, HREE-Y-Nb dominant, in structurally-controlled lenses/veinlets in albitized granite, formed by magmatic enrichment	Peralkaline affinity with high Fe, alkalis, HFSE, REE, positive εNd, arfvedsonite, aegirine, and complex REE-HFSE assemblages formed by two-

(*continued on next page*)

Table 7 (*continued*)

S/N	Province / Study	Tectonic Setting	Magma Source	Key Metallogenic Process	Metal Association & Style	Diagnostic Signature
			subduction. Minimal crustal contamination.	remobilizing and concentrating metals into structures.	and hydrothermal mineralization.	stage (magmatic + orthomagmatic-hydrothermal) with strong structural control.

transtension, mantle-influenced volatile-bearing melts, crustal assimilation, extreme fractionation and structural permeability acted together to generate Sn-Nb-Mo mineralization. This integrated architecture has exploration relevance for comparable anorogenic alkaline and rare-metal granite systems in West Africa, including Aïr, Niger and Mayo Darlé, Cameroon, and for global analogues such as Rondônia, Brazil and Bokan Mountain, Alaska (Table 7).

African analogues show that anorogenic ring-complex magmatism can produce rare-metal fertility, but metal association and ore style vary among provinces. The Niger Alkaline Province is characterized by anorogenic subvolcanic ring complexes with U-Sn-Nb associations, whereas Sabaloka, Sudan, is dominated by Sn-W quartz-vein stockworks and greisen lenses (Almond, 1967, 1977; Bowden et al., 1987). These systems are useful regional comparisons, but they do not reproduce the combined Sn-Nb-Mo association and shear-zone-focused architecture of the Jos Plateau. Mayo Darlé, Cameroon, is a closer African analogue because it is a within-plate Sn system linked to A1-type granite, greisenization, albitization and cassiterite-bearing stockworks (Lavenir et al., 2023; Tantoh et al., 2024). However, Mayo Darlé is more closely associated with Cameroon Volcanic Line magmatism and does not document the same transtensional shear-zone control inferred for Jos.

Several non-African examples are best viewed as process analogues rather than direct tectonic equivalents. In fractionation-dominated systems, Zaaiplaats records Sn enrichment through extreme A-type granite differentiation, volatile-rich cupola development and greisenization (Vonopartis et al., 2020, 2021), whereas Saudi Arabian rare-metal granites show comparable HFSE-REE enrichment, REE tetrad effects and F-rich fluid interaction in within-plate to post-collisional settings (Moghazi et al., 2015; Aseri, 2020; Gahlan et al., 2022). Mo-dominant systems provide a second comparison: Climax illustrates apical focusing of F-rich Mo-bearing melts and fluids in a highly evolved magmatic-hydrothermal system (Audétat, 2015), Gattar records oxidized Mo mineralization from a hybrid crust-mantle source in a post-collisional extensional setting (Feteha et al., 2022), and Duolongqiarou shows Mo concentration during hydrous magma fractionation related to slab-breakoff magmatism (Guo et al., 2022). A third group highlights fluid-mediated HFSE-REE redistribution, with Keivy recording fluid-dominated pegmatite evolution and Nb-Ta-Zr-Hf fractionation in an anorogenic alkaline province (Zozulya et al., 2022), and Strange Lake showing REE-Zr-Nb enrichment followed by fluoride melt exsolution and hydrothermal upgrading in an intracontinental rift setting (Salvi and Williams-Jones, 1990; Siegel et al., 2017, 2018).

The closest global comparisons are the Pitinga-Madeira system and Rondônia Tin Province in Brazil, together with Bokan Mountain in Alaska. Pitinga and Rondônia share key features with Jos, including A-type to peralkaline affinity, strong HFSE enrichment, F-rich melt and fluid evolution and late-stage hydrothermal redistribution of Sn-Nb-Ta-W mineralization (Costi et al., 2002, 2009; Bastos Neto et al., 2009; Geraldes, 2018; Guimarães et al., 2022; de Almeida et al., 2024; Hadlich et al., 2024). Bokan Mountain is also relevant because rift-related peralkaline magmatism, a metasomatized lithospheric source, late F-rich fluids and structural control combine to concentrate U-Th-HREE-Y-Nb mineralization (Dostal et al., 2013, 2014; Dostal and Shellnutt, 2016; Dostal, 2023). Together, these analogues show that Jos-style metallogeny is most likely where source fertility, extreme fractionation, volatile saturation, hydrothermal fluid evolution and structural focusing operate together.

By contrast, plume-related or plume-influenced basaltic provinces such as Emeishan, the Macaronesian ocean-island systems and the Deccan Large Igneous Province are poor analogues for Jos-type Sn-Nb-Mo mineralization (Shellnutt et al., 2009; Black et al., 2021; Civiero et al., 2023). These provinces may host other mineral systems, including Fe-Ti-V, Ni-Cu-PGE, Nb-Zr-REE or alkaline-carbonatitic mineralization (Shellnutt, 2014; Deng et al., 2022; Chen et al., 2023). However, they generally lack the evolved peralkaline granite, crustal AFC, F-rich magmatic-hydrothermal evolution and shear-zone-focused architecture required for the Jos model. The Jos Plateau is therefore best defined by four linked controls: (1) a hybrid mantle-crust source, (2) transtensional reactivation of inherited crustal structures, (3) extreme fractional crystallization producing volatile-rich residual melts, and (4) late magmatic-hydrothermal fluid exsolution that generated greisen lodes, stockworks and vein systems. Tectonic reactivation was the principal focusing mechanism, distinguishing the Jos Plateau from barren alkaline complexes such as Timedjelalen and from basalt-dominated plume systems that are not direct analogues for granite-hosted Sn-Nb-Mo metallogeny.

6. Conclusion

This study demonstrates that Sn-Nb-Mo mineralization in the Jos-Plateau Tin Belt resulted from a Jurassic transtensional regime (179–166 Ma) that generated a spatially evolving magmatic-hydrothermal system. Zircon U–Pb ages define a north-to-south younging trend from Buji (~179 Ma) through Jos-Bukuru (JBK; ~168 Ma) to Kigom (KGM; ~166 Ma). Isotopic and geochemical data reveal systematic variations in crustal and mantle influence. Buji barren granites exhibit the most negative $\varepsilon_{Nd}(t)$ (–4.4 to –4.2), highest Neodymium Crustal Index (NCI = 0.31), and least radiogenic $^{87}Sr/^{86}Sr(i)$ (0.7065–0.7066), indicating an enriched mantle source with strong crustal input. JBK Sn–Nb biotite-amphibole granites show intermediate $\varepsilon_{Nd}(t)$ (–3.3 to –3.0), NCI (0.25), and moderately radiogenic $^{87}Sr/^{86}Sr_{(i)}$ (0.7066–0.7173), suggesting moderate crustal input with selective hydrothermal overprint. KGM Mo–Nb arfvedsonite–riebeckite granites exhibit near-chondritic $\varepsilon_{Nd}(t)$ (–1.1 to –0.4), lowest NCI (0.14), and most radiogenic $^{87}Sr/^{86}Sr_{(i)}$ (0.7139–0.7206), reflecting extreme fluid-mediated metasomatism on a mantle-dominated magma.

Decoupled oxygen fugacity distinguishes oxidized JBK Ca-amphiboles from reduced KGM Na-amphiboles that host oxidized zircons. Mass balance modeling indicates ~40–50 vol% feldspar-dominated fractional crystallization coupled with ~30–40 vol% upper crustal assimilation. JBK granites exhibit Sn-Nb enrichment (4–126 ppm Sn; 37–910 ppm Nb), while KGM granites show high Nb with extreme Zn-Pb-Cu concentrations (≤1326, 1054, 845 ppm respectively), consistent with Mo-enriched systems. Fluorite compositions (F = 52–56 wt%) record F-rich reducing fluids that promoted HFSE-REE-Sn-Nb-Mo mobility.

Key trace element trends (Rb/Sr: 53 → 110; LREE/HREE: 2.5 → 1.7; Th/U: 4.3 → 3.3) and fluorite chemistry ($F/Cl > 15$; $FeO/MnO < 0.1$) confirm a terminal transition from melt- to fluid-dominated to fluid-dominated processes. These data underpin a unified four-stage metallogenic model: (I) magmatic enrichment through protracted fractional crystallization and crustal assimilation; (II) magmatic-hydrothermal transition with F-rich fluid exsolution; (III) hydrothermal veining and stockwork formation, with JBK's restricted fluids forming shear zone-hosted Sn-Nb greisen lodes and KGM's pervasive F-rich flux generating extensive molybdenite stockworks; and (IV) supergene weathering liberating alluvial Sn-Nb placers.

The distinct ore styles are the direct product of transtension-driven decompression melting of metasomatized mantle, ascent along reactivated Pan-African shear zones, upper-crustal assimilation, and fluorine-complexed metal transport within shallowly emplaced (2.6–8.7 km) anorogenic alkaline complexes. The Jos Plateau therefore serves as a reference model for Sn-Nb-Mo mineralization in transtensional alkaline granite systems worldwide.

Declaration of competing interest

The authors declare that they have no known competing financial interests or personal relationships that could have appeared to influence the work reported in this paper.

Acknowledgement

The authors sincerely thank the Editor-in-Chief, Prof. Huayong Chen, for handling this manuscript. We gratefully acknowledge the Associate Editor, Prof. Harald G. Dill, for his constructive editorial guidance and insightful comments, which greatly contributed to refining this work. We are deeply grateful to the two anonymous reviewers and to Martin Kubeš for their thorough and perceptive critiques, which greatly strengthened the manuscript's arguments and clarity. This study was financially supported by the China Postdoctoral Science Foundation (No. 2025M770434) and the National Natural Science Foundation of China (No. 42072082). Additional funding was provided by the United Arab Emirates University, UAE (Grants No. G00004980-12S218 and G00005840).

Appendix A. Supplementary data

Supplementary data to this article can be found online at https://doi.org/10.1016/j.oregeorev.2026.107405.

Data availability

Data will be made available on request.

References

Agangi, A., Kamenetsky, V.S., McPhie, J., 2010. The role of fluorine in the concentration and transport of lithophile trace elements in felsic magmas: insights from the Gawler Range Volcanics, South Australia. Chem. Geol. 273 (3–4), 314–325.

Agemar, T., Wörner, G., Heumann, A., 1999. Stable isotopes and amphibole chemistry on hydrothermally altered granitoids in the North Chilean Precordillera: a limited role for meteoric water? Contrib. Miner. Petrol. 136 (4), 331–344.

Ahmed, H.A., Wang, L.X., Ma, C.Q., Abdallsamed, M.I., Girei, M.B., Zhu, Y.X., Vincent, V. I., Kamaunji, V.D., Cao, L., 2021. Contrasting Neoproterozoic and Mesozoic granitoids in Zaranda complex (Nigeria): insights into the distinct origins, tectonic settings and mineralization potential. Int. J. Earth Sci. 110, 1389–1413.

Almond, D.C., 1967. Discovery of a tin-tungsten mineralization in northern Khartoum Province. Sudan. Geol. Mag. 104 (1), 1–12.

Almond, D.C., 1977. The Sabaloka Igneous Complex, Sudan. Philos. Transact. A Math. Phys. Eng. Sci. 287, 595–633.

Alves, A., de Souza Pereira, G., de Assis Janasi, V., Higgins, M., Polo, L.A., Juriaans, O.S., Ribeiro, B.V., 2015. The origin of felsic microgranitoid enclaves: Insights from plagioclase crystal size distributions and thermodynamic models. Lithos 239, 33–44.

Amuda, A.K., Yang, X., Deng, J., Faisal, M., Cao, J., Bute, S.I., Girei, M.B., Elatikpo, S.M., 2020. Petrogenesis of the peralkaline Dutsen Wai and Ropp complexes in the Nigerian younger granites: Implications for crucial metal enrichments: Int. Geol. Rev. 63 (16), 2057–2081.

Amuda, A.K., Li, S., Yang, X., Cao, J., Faisal, M., 2022. Genetic Association between Granites and Mineralization at the Gindi Akwati Cassiterite–Sulfide Deposit, North-Central Nigeria: Insights from Mineralogy, Fluid Inclusions, and Sulfur Isotopes. Minerals, Minerals 12, 761.

Anderson, J.L., Smith, D.R., 1995. The effects of temperature and fO2 on the Al-inhornblende barometer. Am. Mineral. 80, 549–559.

Andersen, T., Elburg, M.A., 2025. Metaluminous to peralkaline syenites and granites in the late Palaeozoic Oslo Rift, Norway, formed by polybaric fractionation and accumulation processes. Geol. Mag. 162, e53.

Aseri, A.A., 2020. Rare-metal alkaline granite from the Arabian Shield, Saudi Arabia. The University of Western Ontario (Canada). Doctoral dissertation.

Audétat, A., 2015. Compositional evolution and formation conditions of magmas and fluids related to porphyry Mo mineralization at Climax. Colorado. J. Petrol. 56 (8), 1519–1546.

Audétat, A., Edmonds, M., 2020. Magmatic-hydrothermal fluids. Elements: an International Magazine of Mineralogy, Geochemistry, and Petrology 16 (6), 401–406.

Audétat, A., Li, W., 2017. The genesis of Climax-type porphyry Mo deposits: Insights from fluid inclusions and melt inclusions. Ore Geol. Rev. 88, 436–460.

Bailey, D.K., Woolley, A.R., 2005. Repeated, synchronous magmatism within Africa: Timing, magnetic reversals, and global tectonics, in Foulger, G.R., Natland, J.H., Presnall, D.C., and Anderson, D.L., eds., Plates, plumes, and paradigms. Geol. Soc. Am. Spec. Pap. 388, p. 365–377.

Baker, J.A., Thirlwall, M.F., Menzies, M.A., 1996. Sr·Nd·Pb isotopic and trace element evidence for crustal contamination of plume-derived flood basalts: Oligocene flood volcanism in western Yemen. Geochim. Cosmochim. Acta 60 (14), 2559–2581.

Ballouard, C., Massuyeau, M., Elburg, M.A., Tappe, S., Viljoen, F., Brandenburg, J.T., 2020. The magmatic and magmatic-hydrothermal evolution of felsic igneous rocks as seen through Nb-Ta geochemical fractionation, with implications for the origins of rare-metal mineralizations. Earth Sci. Rev. 203, 103115.

Ballouard, C., Poujol, M., Boulvais, P., Branquet, Y., Tartèse, R., Vigneresse, J.L., 2016. Nb-Ta fractionation in peraluminous granites: a marker of the magmatic-hydrothermal transition. Geology 44 (3), 231–234.

Barbarin, B., 2005. Mafic magmatic enclaves and mafic rocks associated with some granitoids of the central Sierra Nevada batholith, California: nature, origin, and relations with the hosts. Lithos 80 (1–4), 155–177.

Bastos Neto, A.C., Pereira, V.P., Ronchi, L.H., de Lima, E.F., Frantz, J.C., 2009. The world-class Sn, Nb, Ta, F (Y, REE, Li) deposit and the massive cryolite associated with the albite-enriched facies of the Madeira A-type granite, Pitinga mining district, Amazonas State. Brazil. Can. Mineral. 47 (6), 1329–1357.

Batchelor, R.A., Bowden, P., 1986. Major and trace element analysis of volcanic and sub-volcanic igneous rocks for the Nigerian-Niger anorogenic complex: Overseas Development Administration Research Scheme, R2679, 33p.

Bau, M., 1996. Controls on the fractionation of isovalent trace elements in magmatic and aqueous systems: evidence from Y/Ho, Zr/Hf, and lanthanide tetrad effect. Contrib. Miner. Petrol. 123 (3), 323–333.

Bea, F., 1996. Residence of REE, Y, Th and U in granites and crustal protoliths; implications for the chemistry of crustal melts. J. Petrol. 37 (3), 521–552.

Beard, C.D., Goodenough, K.M., Borst, A.M., Wall, F., Siegfried, P.R., Deady, E.A., Pohl, C., Hutchison, W., Finch, A.A., Waler, B.F., Elliott, H., Brauch, K., 2023. Alkaline-silicate REE-HFSE systems. Econ. Geol. 118 (1), 177–208.

Bénard, A., Ionov, D.A., 2013. Melt–and fluid–rock interaction in supra-subduction lithospheric mantle: evidence from andesite-hosted veined peridotite xenoliths. J. Petrol. 54 (11), 2339–2378.

Beus, A.A., Grigorian, S.V., 1977. Geochemical exploration methods for mineral deposits (A. A. Levinson, Trans.; A. A. Levinson, Ed.). Applied Publishing Ltd. x + 287 pp. Wilmette, Illinois USA.

Ballard, J.R., Palin, J.M., Campbell, I.H., 2002. Relative oxidation states of magmas inferred from Ce (IV)/Ce (III) in zircon: application to porphyry copper deposits of northern Chile. Contrib. Miner. Petrol. 144 (3), 347–364.

Bennett, J.N., Turner, D.C., Ike, E.C., Bowden, P., 1984. The geology of some northern Nigerian anorogenic ring complexes: HMS. British Geological Survey: Overseas Geology and Mineral Resources 61, 1–65.

Black, B.A., Karlstrom, L., Mather, T.A., 2021. The life cycle of large igneous provinces. Nat. Rev. Earth Environ. 2 (12), 840–857.

Black, R., Liégeois, J.P., 1993. Cratons, mobile belts, alkaline rocks and continental lithospheric mantle: the Pan-african testimony. J. Geol. Soc. 150 (1), 89–98.

Black, R., Lameyre, J., Bonin, B., 1985. The structural setting of alkaline complexes. J. Afr. Earth Sc. 3 (1–2), 5–16.

Borges, R.M.K., Amorim, L.E.D., Rios, F.J., Santos, G.C.S., Freitas, M.E., Lima, T.A.F., Santos, A., Pedrosa, T.A., 2021. Melt-melt immiscibility and implications for the origin of Madeira albite-rich granite, Pitinga mine, Amazonas, Brazil: a melt inclusion study. Braz. J. Geol. 51 (4), e20210003.

Bonin, B., 2007. A-type granites and related rocks: evolution of a concept, problems and prospects. Lithos 97 (1–2), 1–29.

Borst, A.M., Waight, T.E., Finch, A.A., Storey, M., Roux, P.L., 2019. Dating agpaitic rocks: a multi-system (U/Pb, Sm/Nd, Rb/Sr and 40Ar/39Ar) isotopic study of layered nepheline syenites from the Ilímaussaq complex, Greenland. Lithos 324, 74–88.

Bowden, P., Black, R., Martin, R.F., Ike, E.C., Kinnaird, J.A., Batchelor, R.A., 1987. Niger-Nigerian alkaline ring complexes: a classic example of African Phanerozoic anorogenic mid-plate magmatism. Geol. Soc. Spec. Publ. 30 (1), 357–379.

Bowden, P., Kinnaird, J.A., 1984. The petrology and geochemistry of alkaline granites from Nigeria. Phys. Earth Planet. Inter. 35, 199–211.Bowden, P., Van Breemen, O., Hutchinson, J., Turner, D. C., 1976. Palaeozoic and Mesozoic age trends for some ring complexes in Niger and Nigeria. Nature, 259(5541), 297–299.

Bowden, P., Van Breemen, O., Hutchinson, J., Turner, D.C., 1976. Palaeozoic and Mesozoic age trends for some ring complexes in Niger and Nigeria. Nature 259 (5541), 297–299.

Buchannan, M.S., Macleod, W.N., Turner, D.C., 1971. The geology of the Jos Plateau. Geological Survey of Nigeria Bulletin 32 (2), 107–119.

Bute, S.I., Yang, X., Cao, J., Liu, L., Deng, J., Vela Haruna, I.V., Girei, M.B., Abubakar, U., Akhtar, S., 2019. Origin and tectonic implications of ferroan alkali-calcic granitoids from the Hawal Massif, east-eastern Nigeria terrane: clues from geochemistry and zircon U-Pb-Hf isotopes. Int. Geol. Rev. 62 (2), 129–152.

Cao, L., Wang, L.X., Zhu, Y.X., Vincent, V.I., Kamaunji, V.D., Ahmed, H.A., 2024. Termination of anorogenic alkaline magmatism in Nigerian Younger Granite province: insights from Afu A-type granite complex. Int. J. Earth Sci. 113(4), 1029–1052.Charoy, B., Raimbault, L., 1994. Zr-, Th-, and REE-rich biotite differentiates in the A-type granite pluton of Suzhou (Eastern China): the key role of fluorine. Journal of petrology, 35(4), 919–962.

Charles, R.W., 1975. The phase equilibria of richterite and ferrorichterite. Am. Mineral. 60, 367–374.

Charoy, B., Raimbault, L., 1994. Zr-, Th-, and REE-rich biotite differentiates in the A-type granite pluton of Suzhou (Eastern China): the key role of fluorine. J. Petrol. 35 (4), 919–962.

Chauvet, A., 2019. Structural control of ore deposits: the role of pre-existing structures on the formation of mineralised vein systems. Minerals 9 (1), 56.

Chen, X.D., Li, Y.G., Luo, Z.H., Fei, G.C., Luo, W., Zhang, T.J., Zou, Y.S., 2023. Formation of Fe-Ti oxide and Ni-Co sulfide ores by concentric tube flow and hydrous metal-rich melt recharge into the cooling crystal mush: example from the Hongge intrusion in Panxi region, SW China. Ore Geol. Rev. 160, 105594.

Civiero, C., Carvalho, J., Silveira, G., 2023. Mantle structure beneath the Macaronesian volcanic islands (Cape Verde, Canaries, Madeira and Azores): a review and future directions. Front. Earth Sci. 11, 1126274.

Claiborne, L.L., Miller, C.F., Walker, B.A., Wooden, J.L., Mazdab, F.K., Bea, F., 2006. Tracking magmatic processes through Zr/Hf ratios in rocks and Hf and Ti zoning in zircons: an example from the Spirit Mountain batholith, Nevada. Mineral. Mag. 70 (5), 517–543.

Collins, W.J., Huang, H. Q., Bowden, P., Kemp, A.I S., 2020. Repeated S–I–A-type granite trilogy in the Lachlan Orogen and geochemical contrasts with A-type granites in Nigeria: implications for petrogenesis and tectonic discrimination. In Post-Archean Granitic Rocks: Petrogenetic Processes and Tectonic Environments Janoušek, V., Bonin, B., Collins, W. J., Farina, F. & Bowden, P. (eds) Geol. Soc. Lond. Spec. Publ. 491.

Costi, H.T., Dall'Agnol, R., Borges, R.M.K., Minuzzi, O.R.R., Teixeira, J.T., 2002. Tin-bearing sodic episyenites associated with the Proterozoic, A-type Água Boa granite, Pitinga mine, Amazonian Craton, Brazil. Gondwana Res. 5 (2), 435–451.

Costi, H.T., Dall'Agnol, R., Pichavant, M., Ramo, O.T., 2009. The peralkaline tin-mineralized Madeira cryolite albite-rich granite of Pitinga, Amazonian craton, Brazil: petrography, mineralogy and crystallization processes. Can. Mineral. 47 (6), 1301–1327.

Coulon, C., Vidal, P., Dupuy, C., Baudin, P., Popoff, M., Maluski, H., Hermitte, D., 1996. The Mesozoic to early Cenozoic magmatism of the Benue Trough (Nigeria); geochemical evidence for the involvement of the St Helena plume. J. Petrol. 37 (6), 1341–1358.

Crisp, L.J., Berry, A.J., 2022. A new model for zircon saturation in silicate melts. Contrib. Miner. Petrol. 177 (7), 71.

Czamanske, G.K., Wones, D.R., 1973. Oxidation during magmatic differentiation, Finnmarka complex, Oslo area, Norway: part 2, the mafic silicates1. J. Petrol. 14 (3), 349–380.

Dada, S.S., Briqueu, L., Harms, U., Lancelot, J.R., Matheis, G., 1995. Charnockitic and monzonitic Pan-African series from north-central Nigeria: trace-element and Nd, Sr, Pb isotope constraints on their petrogenesis. Chem. Geol. 124 (3–4), 233–252.

Dada, S.S., Lancelot, J.R., Briqueu, L., 1989. Age and origin of the annular charnockitic complex at Toro, Northern Nigeria: U-Pb and Rb-Sr evidence. J. Afr. Earth Sc. 9 (2), 227–234.

Dall'Agnol, R., Frost, C.D., Rämö, O.T., 2012. IGCP Project 510 "A-type Granites and Related Rocks through Time": Project vita, results, and contribution to granite research. Lithos 151, 1–16.

de Almeida, E.C., Galé, M.G., Souza, M.V., da Silva, M.M., 2024. A review of geochemical evolution and mineralization events in A-type granites of the Rondônia tin province, Amazonian Craton. J. S. Am. Earth Sci. 133, 104732.

De Campos, C.P., Perugini, D., Ertel-Ingrisch, W., Dingwell, D.B., Poli, G., 2011. Enhancement of magma mixing efficiency by chaotic dynamics: an experimental study. Contrib. Miner. Petrol. 161, 863–881.

Deng, W., Wen, H.J., Du, S.J., Ling, K.Y., Fan, H.F., Zhu, C.W., Yang, Y., 2022. Provenance of late Permian Nb-Zr-REE-Ga enrichment in western Guizhou: Implications for the waning volcanism of Emeishan large igneous province. Ore Geol. Rev. 150, 105160.

DePaolo, D.J., 1979. Implications of correlated Nd and Sr isotopic variations for the chemical evolution of the crust and mantle. Earth Planet. Sci. Lett. 43 (2), 201–211.

DePaolo, D.J., 1981. Trace element and isotopic effects of combined wallrock assimilation and fractional crystallization. Earth Planet. Sci. Lett. 53 (2), 189–202.

DePaolo, D.J., Perry, F.V., Baldridge, W.S., 1992. Crustal versus mantle sources of granitic magmas: a two-parameter model based on Nd isotopic studies. Earth Environ. Sci. Trans. R. Soc. Edinb. 83 (1–2), 439–446.

Dickin, A.P., Halliday, A.N., Bowden, P., 1991. A Pb, Sr and Nd isotope study of the basement and Mesozoic ring complexes of the Jos Plateau, Nigeria. Chem. Geol. 94 (1), 23–32.

Dolejš, D., Baker, D.R., 2006. Fluorite solubility in hydrous haplogranitic melts at 100 MPa. Chem. Geol. 225, 40–60.

Dolejš, D., Baker, D.R., 2004. Thermodynamic analysis of the system Na2O-K2O-CaO-Al2O3-SiO2-H2O-F2O− 1: stability of fluorine-bearing minerals in felsic igneous suites. Contrib. Miner. Petrol. 146 (6), 762–778.

Dorado, O., Wolff, J.A., Ramos, F.C., Martí, J., 2023. Ba, Sr, and Rb feldspar/melt partitioning in recent eruptions from Teide-Pico Viejo volcanic complex, Tenerife: New insights into pre-eruptive processes. Front. Earth Sci. 11, 1155724.

Dostal, J., 2023. Jurassic uranium-thorium deposit of peralkaline granitic rocks, Bokan Mountain, Prince of Wales Island, southeastern Alaska. Minerals 13 (8), 1032.

Dostal, J., 2016. Rare metal deposits associated with alkaline/peralkaline igneous rocks. In: Verplanck, P.L., Hitzman, M.W. (Eds.), Rare Earth and Critical Elements in Ore Deposits. Society of Economic Geologists, pp. 33–54.

Dostal, J., Karl, S.M., Keppie, J.D., Kontak, D.J., Shellnutt, J.G., 2013. Bokan Mountain peralkaline granitic complex, Alexander terrane (southeastern Alaska): evidence for Early Jurassic rifting prior to accretion with North America. Can. J. Earth Sci. 50 (6), 678–691.

Dostal, J., Kontak, D.J., Karl, S.M., 2014. The Early Jurassic Bokan Mountain peralkaline granitic complex (southeastern Alaska): Geochemistry, petrogenesis and rare-metal mineralization. Lithos 202, 395–412.

Dostal, J., Shellnutt, J.G., 2016. Origin of peralkaline granites of the Jurassic Bokan Mountain complex (southeastern Alaska) hosting rare metal mineralization. Int. Geol. Rev. 58 (1), 1–13.

Drake, M.J., Weill, D.F., 1975. Partition of Sr, Ba, Ca, Y, Eu2+, Eu3+, and other REE between plagioclase feldspar and magmatic liquid: an experimental study. Geochim. Cosmochim. Acta 39 (5), 689–712.

Eby, G.N., 1992. Chemical subdivision of the A-type granitoids: petrogenetic and tectonic implications. Geology 20 (7), 641–644.

El Bouseily, A.M., El Sokkary, A.A., 1975. The relation between Rb, Ba and Sr in granitic rocks. Chem. Geol. 16 (3), 207–219.

Ernst, W.G., 1968. Amphiboles: Crystal chemistry, phase relations, and occurrence (Minerals, Rocks and Inorganic Materials, Vol. 1). Pp. x + 125. New York: Springer-Verlag.

Ersoy, Y., Helvacı, C., 2010. FC–AFC–FCA and mixing modeler: a Microsoft® Excel© spreadsheet program for modeling geochemical differentiation of magma by crystal fractionation, crustal assimilation and mixing. Comput. Geosci. 36 (3), 383–390.

Estrade, G., Salvi, S., Béziat, D., Rakotovao, S., Rakotondrazafy, R., 2014a. REE and HFSE mineralization in peralkaline granites of the Ambohimirahavavy alkaline complex, Ampasindava peninsula, Madagascar. J. Afr. Earth Sci. 94, 141–155.

Estrade, G., Béziat, D., Salvi, S., Tiepolo, M., Paquette, J.L., Rakotovao, S., 2014b. Unusual evolution of silica-under-and-oversaturated alkaline rocks in the Cenozoic Ambohimirahavavy complex (Madagascar): Mineralogical and geochemical evidence. Lithos 206, 361–383.

Etsu, F.B., 2025. Genesis and timing of anorogenic alkaline magmatism in Afu complex, North-Central Nigeria. Unpublished Masters Dissertation, China University of Geosciences, Wuhan. 88p.

Fang, J., Audétat, A., Dolejš, D., 2025. Molybdenum speciation in magmatic-hydrothermal fluids: Constraints from molybdenite solubility experiments and thermodynamic modeling. Geochim. Cosmochim. Acta 395, 95–111.

Ferré, E.C., Caby, R., Peucat, J.J., Capdevila, R., Monié, P., 1998. Pan-African, post-collisional, ferro-potassic granite and quartz–monzonite plutons of Eastern Nigeria. Lithos 45 (1–4), 255–279.

Feteha, B.F., Lentz, D.R., El Bouseily, A.M., Khalil, K.I., Khamis, H.A., Moghazi, A.K.M., 2022. Petrogenesis of Neoproterozoic Mo-bearing A-type granites in the Gattar area, northern Eastern Desert, Egypt: implications for magmatic evolution and mineralization processes. Ore Geol. Rev. 148, 105007.

Frost, C.D., Frost, B.R., 2011. On ferroan (A-type) granitoids: their compositional variability and modes of origin. J. Petrol. 52 (1), 39–53.

Frost, B.R., Barnes, C.G., Collins, W.J., Arculus, R.J., Ellis, D.J., Frost, C.D., 2001. A geochemical classification for granitic rocks. J. Petrol. 42 (11), 2033–2048.

Fowler, A.R., Hamimi, Z., 2024. The Tuareg Shield and Trans-Saharan Orogenic Belt of Central Part of Northwest Africa: an overview. In: Hamimi, Z., Chabou, M.C., Errami, E., Fowler, A.-.-R., Fello, N., Masrouhi, A., Leprêtre, R. (Eds.), The Geology of North Africa. Regional Geology Reviews, Springer, Cham, pp. 69–108.

Gahlan, H.A., Azer, M.K., Al-Hashim, M.H., Heikal, M.T.S., 2022. Highly evolved rare-metal bearing granite overprinted by alkali metasomatism in the Arabian Shield: a case study from the Jabal Tawlah granites. J. Afr. Earth Sc. 192, 104556.

Gamal-Adeen, I., Shahien, M.G., Zayed, A.M., Bakhit, B.R., Sanislav, I.V., Sharib, A.A., 2023. Sequential deuteric and hydrothermal alterations in the Late Neoproterozoic Um Naggat rare metal-bearing granite, Central Eastern Desert, Egypt. J. Afr. Earth Sci. 203, 104932.

Geraldes, M.C. (2018). Rondonia Tin Province: A review. In Proceedings of the 49. Brazilian congress of geology; 7. Symposium on volcanism and associated environments; 9. Symposium of cretaceous from Brazil (pp. 1880-1880).

Girei, M.B., Li, H., Algeo, T.J., Bonin, B., Ogunleye, P.O., Bute, S.I., Ahmed, H.A., 2019. Petrogenesis of A-type granites associated with Sn–Nb–Zn mineralization in Ririwai complex, north-Central Nigeria: Constraints from whole-rock SmNd and zircon Lu-Hf isotope systematics. Lithos 340, 49–70.

Girei, M.B., Li, H., Vincent, V.I., Algeo, T.J., Elatikpo, S.M., Bute, S.I., Ahmed, H.A., Amuda, A.K., 2020. Genesis and timing of Mo mineralization in the Mada Ring complex, north-central Nigeria: insights from whole-rock geochemistry, Nd-Sr isotopes, zircon U-Pb-Hf isotopes, and molybdenite Re-Os systematics. Miner. Depos. 57, 601–620.

Giret, A., Bonin, B., Leger, J.M., 1980. Amphibole compositional trends in oversaturated and undersaturated alkaline plutonic ring-composition. Can. Mineral. 18 (4), 481–495.

Glodny, J., Grauert, B., 2009. Evolution of a hydrothermal fluid-rock interaction system as recorded by Sr isotopes: a case study from the Schwarzwald, SW Germany. Mineral. Petrol. 95 (3), 163–178.

Goodenough, K.M., Lusty, P.A.J., Roberts, N.M.W., Key, R.M., Garba, A., 2014. Post-collisional Pan-African granitoids and rare metal pegmatites in western Nigeria: Age, petrogenesis, and the 'pegmatite conundrum'. Lithos 200, 22–34.

Green, T.H., 1995. Significance of Nb/Ta as an indicator of geochemical processes in the crust-mantle system. Chem. Geol. 120 (3–4), 347–359.

Green, T.H., Pearson, N.J., 1987. An experimental study of Nb and Ta partitioning between Ti-rich minerals and silicate liquids at high pressure and temperature. Geochim. Cosmochim. Acta 51 (1), 55–62.

Grimes, C.B., Wooden, J.L., Cheadle, M.J., John, B.E., 2015. "Fingerprinting" tectono-magmatic provenance using trace elements in igneous zircon. Contrib. Miner. Petrol. 170, 1–26.

Guimarães, F.S., Zhang, R., Lehmann, B., Raphael Cabral, A., Rios, F.J., 2022. Cassiterite U-Pb geochronology of the Santa Barbara tin district, Rondonia tin province. Brazil. Econ. Geol. 117 (3), 719–729.

Guiraud, R., Bosworth, W., Thierry, J., Delplanque, A., 2005. Phanerozoic geological evolution of Northern and Central Africa: an overview. J. Afr. Earth Sc. 43 (1–3), 83–143.

Guo, H., Audétat, A., 2017. Transfer of volatiles and metals from mafic to felsic magmas in composite magma chambers: an experimental study. Geochim. Cosmochim. Acta 198, 360–378.

Guo, X., Zhou, T., Jia, Q., Li, J., Kong, H., 2022. Highly differentiated felsic granites linked to Mo mineralization in the East Kunlun Orogenic Belt, NW China: Constrains from geochemistry, and Sr-Nd-Hf isotopes of the Duolongqiarou porphyry Mo deposit. Ore Geol. Rev. 145, 104891.

Hadlich, I.W., Bastos Neto, A.C., Pereira, V.P., Dill, H.G., Botelho, N.F., 2024. The radioactive rare metal mineralization in the world-class Sn-Nb-Ta-U-Th-REE-deposit Madeira (Pitinga, Amazonas State, Brazil): with special reference to the complex alteration of pyrochlore-group minerals. Minerals 14 (9), 895.

Hassan, J.I., Li, H., Algeo, T.J., Wang, R., Umar, I.H., Ibrahim, A., Sajid, A., 2025. Geochemistry and geochronology of magmatic rocks from Kofayi complex, north-central Nigeria: Insights into their petrogenesis and geodynamic settings. Lithos 108275.

Hawthorne, F.C., Oberti, R., Harlow, G.E., Maresch, W.V., Martin, R.F., Schumacher, J. C., Welch, M.D., 2012. Nomenclature of the amphibole supergroup. Am. Mineral. 97 (11–12), 2031–2048.

Heinrich, C.A., 2024. The chain of processes forming porphyry copper deposits—An invited paper. Econ. Geol. 119 (4), 741–769.

Henderson, C.M.B., Pierozynski, W.J., 2012. An experimental study of Sr, Ba and Rb partitioning between alkali feldspar and silicate liquid in the system nepheline–kalsilite–quartz at 0.1 GPa P (H2O): a revisitation and reassessment. Mineral. Mag. 76 (1), 157–190.

Hoskin, P.W., Schaltegger, U., 2003. The composition of zircon and igneous and metamorphic petrogenesis. Rev. Mineral. Geochem. 53 (1), 27–62.

Hou, Z.Q., Xu, B., Zhang, H., Zheng, Y.C., Wang, R., Liu, Y., Miao, Z., Gao, L., Zhao, Z., Griffin, W.L., O'Reilly, S.Y., 2023. Refertilized continental root controls the formation of the Mianning–Dechang carbonatite-associated rare-earth-element ore system. Commun. Earth Environ. 4 (1), 293.

Icenhower, J., London, D., 1996. Experimental partitioning of Rb, Cs, Sr, and Ba between alkali feldspar and peraluminous melt. Am. Mineral. 81 (5–6), 719–734.

Imeokparia, E.G., 1981. Fluorine in biotites from the AFU younger granite complex (central Nigeria). Chem. Geol. 32 (1–4), 247–254.

Imeokparia, E.G., 1984. Geochemistry of intrusive rocks associated with molybdenite mineralization (Kigom Complex, northern Nigeria). Chem. Geol. 47 (3–4), 261–283.

Imeokparia, E.G., 1980. Ore-bearing potential of granitic rocks from the Jos—Bukuru Complex, northern Nigeria. Chem. Geol. 28, 69–77.

Irber, W., 1999. The lanthanide tetrad effect and its correlation with K/Rb, Eu/Eu*, Sr/Eu, Y/Ho, and Zr/Hf of evolving peraluminous granite suites. Geochim. Cosmochim. Acta 63 (3–4), 489–508.

Jackson, M.G., Dasgupta, R., 2008. Compositions of HIMU, EM1, and EM2 from global trends between radiogenic isotopes and major elements in ocean island basalts. Earth Planet. Sci. Lett. 276 (1–2), 175–186.

Jain, C., Sobolev, S., Sobolev, A., Vezinet, A., 2024. Thermochemical models of early Earth evolution constrained by geochemical data. European Geosciences Union General Assembly 2024 (EGU24), 9734.

Jahn, B.M., Wu, F., Capdevila, R., Martineau, F., Zhao, Z., Wang, Y., 2001. Highly evolved juvenile granites with tetrad REE patterns: the Woduhe and Baerzhe granites from the Great Xing'an Mountains in NE China. Lithos 59 (4), 171–198.

Jaupart, C., Mareschal, J.C., 2021. Lithosphere, continental: thermal structure. In: Encyclopedia of Solid Earth Geophysics. Springer International Publishing, Cham, pp. 872–884.

Jung, S., Berndt, J., Stracke, A., Hauff, F., Kastek, N., 2014. Anatexis of juvenile mafic to intermediate crust–constraints from major and trace element and Sr, Nd, Pb isotopes of diorites to granites (Damara Orogen, Nambia). S. Afr. J. Geol. 117 (1), 149–171.

Kamaunji, V.D., Wang, L.X., Ahmed, H.A., Zhu, Y.X., Vincent, V.I., Girei, M.B., 2020. Coexisting A1 and A2 granites of Kudaru Complex: implications for genetic and tectonic diversity of A-type granite in the Younger Granite province, north-central Nigeria. Int. J. Earth Sci. 109, 511–535.

Kamaunji, V.D., Wang, L.X., Chen, W., Girei, M.B., Ahmed, H.A., Zhu, Y.X., Vincent, V.I., Cao, L., 2023. Petrogenesis and rare-metal mineralization of the Ririwai alkaline granitoids, north-central Nigeria: mineralogical and geochemical constraints. Int. Geol. Rev. 66 (13), 2409–2439.

Kamaunji, V.D., Wang, L., Girei, M.B., Zhu, Y., Li, L., Vincent, V.I., Amuda, A.K., 2022a. Petrogenesis and tectonic implication of the alkaline ferroan granites from Ropp complex, north-central Nigeria: Clues from zircon chemistry, U–Pb dating, and Lu–Hf isotope. Geol. J. 58 (1), 21–50.

Kamaunji, V.D., Kamaunji, D.Z., Gana, V., Ntekim, E.E., Ukaomah, C.F., Madaki, A.I., 2022b. Integrated Landsat multispectral imagery and airborne geophysical data for enhanced litho-structural mapping: a case study of Adamawa Massif, north-eastern Nigeria. J. Afr. Earth Sc. 195, 104677.

Kamaunji, V.D., Wang, L.X., Murphy, D.T., Girei, M.B., Ahmed, H.A., Etsu, F.B., Sami, M., 2024. Petrogenesis and tectonic implications of peralkaline-metaluminous magmatism in Kila and Shira ring complexes, north-central Nigeria. Int. Geol. Rev. 67 (10), 1279–1305.

King, P.L., White, A.J.R., Chappell, B.W., Allen, C.M., 1997. Characterization and origin of aluminous A-type granites from the Lachlan Fold Belt, southeastern Australia. J. Petrol. 38 (3), 371–391.

Kinnaird, J.A., 1984. Contrasting styles of Sn-Nb-Ta-Zn mineralization in Nigeria. J. Afr. Earth Sc. 2 (2), 81–90.

Kinnaird, J. A., 1981. Geology of the Nigerian Anorogenic Ring Complexes. Map Scale 1: 500,000. John Bartholomew, Edinburgh.

Kinnaird, J.A., 1985. Hydrothermal alteration and mineralization of the alkaline anorogenic ring complexes of Nigeria. J. Afr. Earth Sc. 3 (1–2), 229–251.

Kinnaird, J., Bowden, P., 1987. African anorogenic alkaline magmatism and mineralization—a discussion with reference to the Niger-Nigerian Province. Geol. J. 22 (S2), 297–340.

Kinnaird, J.A., Nex, P.A., Milani, L., 2016. Tin in Africa. Episodes 39 (2), 361–380.

Kocatürk, H., Kumral, M., Sendir, H., Kaya, M., Creaser, R.A., Abdelnasser, A., 2025. Magmatic Redox Evolution and Porphyry–SKARN transition in Multiphase Cu-Mo-W-Au Systems of the Eocene Tavşanlı Belt, NW Türkiye. Minerals 15 (8), 792.

Kovalenko, V.I., Tsaryeva, G.M., Goreglyad, A.V., Yarmolyuk, V.V., Troitsky, V.A., Hervig, R.L., Farmer, G., 1995. The peralkaline granite-related Khaldzan-Buregtey rare metal (Zr, Nb, REE) deposit, western Mongolia. Econ. Geol. 90 (3), 530–547.

Lavenir, N.M.J., Fuh, N.E., Junior, E.E.M., 2023. Petrogenesis of the Mayo-Darley tin formations, anorogenic complex of the Cameroon Line: implication for tin deposit. Acta Geochim. 42 (4), 704–725.

Leake, B.E., Woolley, A.R., Arps, C.E., Birch, W.D., Gilbert, M.C., Grice, J.D., Youzhi, G., 1997. Nomenclature of amphiboles; report of the subcommittee on amphiboles of the International Mineralogical Association, Commission on New Minerals and Mineral Names. Can. Mineral. 35 (1), 219–246.

Lehmann, B., 2021. Formation of tin ore deposits: A reassessment. Lithos, 402, 105756. Li, H., Zhou, J., Ouyang, L., Algeo, T. J., Sun, W., Xie, Y., Li, X., Wang, Z., 2024. Multi-stage magmatism and Sn-polymetallic mineralization in the Shuicheng Region, SW China. Lithos, 478, 107624.

Li, H., Myint, A.Z., Yonezu, K., Watanabe, K., Algeo, T.J., Wu, J.H., 2018. Geochemistry and U–Pb geochronology of the Wagone and Hermyingyi A-type granites, southern Myanmar: Implications for tectonic setting, magma evolution and Sn–W mineralization. Ore Geol. Rev. 95, 575–592.

Li, H., Zhou, J., Ouyang, L., Algeo, T.J., Sun, W., Xie, Y., Wang, Z., 2024. Multi-stage magmatism and Sn-polymetallic mineralization in the Shuicheng Region, SW China. Lithos 478, 107624.

Li, X.C., Harlov, D.E., Zhou, M.F., Hu, H., 2022a. Metasomatic modification of Sr isotopes in apatite as a function of fluid chemistry. Geochim. Cosmochim. Acta 323, 123–140.

Li, X.C., Harlov, D.E., Zhou, M.F., Hu, H., 2022b. Experimental investigation into the disturbance of the Sm-Nd isotopic system during metasomatic alteration of apatite. Geochim. Cosmochim. Acta 330, 191–208.

Liégeois, J.P., Abdelsalam, M.G., Ennih, N., Ouabadi, A., 2013. Metacraton: nature, genesis and behavior. Gondw. Res. 23 (1), 220–237.

Liégeois, J.-P., Benhallou, A., Azzouni-Sekkal, A., Yahiaoui, R., Bonin, B., 2005. The Hoggar swell and volcanism: Reactivation of the Precambrian Tuareg shield during Alpine convergence and West African Cenozoic volcanism. In G. R. Foulger, J. H. Natland, D. C. Presnall, & D. L. Anderson (Eds.), Plates, plumes, and paradigms (Geol. Soc. Am. Spec. Pap. 388, pp. 379–400). Geol. Soc. Am.

Liégeois, J.P., Bertrand, J.M., Black, R., 1987. The subduction-and collision-related Pan-African composite batholith of the Adrar des Iforas (Mali): a review. Geol. J. 22 (S2), 185–211.

Liégeois, J.P., Black, R., 1987. Alkaline magmatism subsequent to collision in the Pan-African belt of the Adrar des Iforas (Mali). Geol. Soc. Lond. Spec. Publ. 30 (1), 381–401.

Liégeois, J.P., Black, R., Navez, J., Latouche, L., 1994. Early and late Pan-African orogenies in the Aïr assembly of terranes (Tuareg shield, Niger). Precambr. Res. 67 (1–2), 59–88.

Lindsley, D.H., Frost, B.R., 1992. Equilibria among Fe-Ti oxides, pyroxenes, olivine, and quartz: Part I. Theory. Am. Mineral. 77(9–10), 987–1003.Lin, H., Xu, X., Yang, J., 2022. Effect of fault extension relevant to unconformity on hydrothermal fluid flow, mass transport, and uranium deposition. Water, 14(7), 1097.

Locock, A.J., 2014. An Excel spreadsheet to classify chemical analyses of amphiboles following the IMA 2012 recommendations. Comput. Geosci. 62, 1–11.

Loiselle, M.C., Wones, D.R., 1979. Characteristics and origin of anorogenic granites. Geol. Soc. Am. Abstr. Programs 11, 468.

London, D., 2018. Ore-forming processes within granitic pegmatites. Ore Geol. Rev. 101, 349–383.

Liu, X., Yu, P., Xiao, C., 2023. Tin transport and cassiterite precipitation from hydrothermal fluids. Geosci. Front. 14 (6), 101624.

Ma, Y., Liu, C., 2001. Sr isotope evolution during chemical weathering of granites: —Impact of relative weathering rates of minerals. Sci. China Series A: Earth Sci. 44 (8), 726–734.

Macdonald, R., Scaillet, B., 2006. The central Kenya peralkaline province: insights into the evolution of peralkaline salic magmas. Lithos 91 (1–4), 59–73.

MacLeod, W.N., Turner, D.C., Wright, E.P., 1971. The geology of the Jos Plateau. Geological Survey of Nigeria Bulletin (GSN) 32, 110.

Manthilake, G., Koga, K.T., Peng, Y., Mookherjee, M., 2021. Halogen bearing amphiboles, aqueous fluids, and melts in subduction zones: insights on halogen cycle from electrical conductivity. J. Geophys. Res. Solid Earth 126, e2020JB021339.

Marks, M.A., Hettmann, K., Schilling, J., Frost, B.R., Markl, G., 2011. The mineralogical diversity of alkaline igneous rocks: critical factors for the transition from miaskitic to agpaitic phase assemblages. J. Petrol. 52 (3), 439–455.

Marks, M., Vennemann, T., Siebel, W., Markl, G., 2003. Quantification of magmatic and hydrothermal processes in a peralkaline syenite–alkali granite complex based on textures, phase equilibria, and stable and radiogenic isotopes. J. Petrol. 44 (7), 1247–1280.

Marshall, A., Macdonald, R., Rogers, N.W., Fitton, J.G., Tindle, A.G., Nejbert, K., Hinton, R.W., 2009. Fractionation of peralkaline silicic magmas: the greater Olkaria volcanic complex, Kenya Rift Valley. J. Petrol. 50 (2), 323–359.

Mathur, R., Powell, W., Yao, J., Guimaraes, F., Cheng, Y., Godfrey, L., Lehmann, B., 2025. Global Sn isotope compositions of cassiterite identify the magmatic–hydrothermal evolution of tin ore systems. Geosciences 15 (1), 28.

Melcher, F., Graupner, T., Oberthür, T., Schütte, P., 2017. Tantalum-(niobium-tin) mineralisation in pegmatites and rare-metal granites of Africa. S. Afr. J. Geol. 120 (1), 77–100.

Migdisov, A.A., Williams-Jones, A.E., Wagner, T., 2009. An experimental study of the solubility and speciation of the Rare Earth Elements (III) in fluoride-and chloride-bearing aqueous solutions at temperatures up to 300 C. Geochim. Cosmochim. Acta 73 (23), 7087–7109.

Moghazi, A.K.M., Iaccheri, L.M., Bakhsh, R.A., Kotov, A.B., Ali, K.A., 2015. Sources of rare-metal-bearing A-type granites from Jabel Sayed complex, Northern Arabian Shield, Saudi Arabia. J. Asian Earth Sci. 107, 244–258.

Monecke, T., Kempe, U., Trinkler, M., Thomas, R., Dulski, P., Wagner, T., 2011. Unusual rare earth element fractionation in a tin-bearing magmatic-hydrothermal system. Geology 39 (4), 295–298.

Moreau, C., Demaiffe, D., Bellion, Y., Boullier, A.M., 1994. A tectonic model for the location of Palaeozoic ring complexes in Aïr (Niger, West Africa). Tectonophysics 234 (1–2), 129–146.

Moussine-Pouchkine, A., Bertrand-Sarfati, J., 1978. Le Gourma; un aulacogene du Precambrien superieur? Bull. Soc. Géol. France 7 (6), 851–855.

Moyen, J.F., 2009. High Sr/Y and La/Yb ratios: the meaning of the “adakitic signature”. Lithos 112 (3–4), 556–574.

Ngako, V., Njonfang, E., Aka, F.T., Affaton, P., Nnange, J.M., 2006. The North–South Paleozoic to Quaternary trend of alkaline magmatism from Niger–Nigeria to Cameroon: complex interaction between hotspots and Precambrian faults. J. Afr. Earth Sc. 45 (3), 241–256.

Ni, X., Cao, T., Wang, B., Cluzel, D., Sun, Y., Chen, Y., Faure, M., 2025. Triassic intracontinental crustal reworking of the Eastern Tianshan: new insights from Late Triassic Adakitic and low-Sr/Y granitoids in the Bogda Range. Geochem. Geophys. Geosyst. 26 (10), e2025GC012428.

Oberti, R., Cannillo, E., Toscani, G., 2012. How to name amphiboles after the IMA2012 report: rules of thumb and a new PC program for monoclinic amphiboles. Period. Mineral. 81 (2).

Ogunleye, P.O., Garba, I., Ike, E.C., 2006. Factors contributing to enrichment and crystallization of niobium in pyrochlore in the Kaffo albite arfvedsonite granite, Ririwai Complex, Younger Granites province of Nigeria. J. Afr. Earth Sc. 44 (3), 372–382.

Olade, M.A., 1980. Geochemical characteristics of tin-bearing and tin-barren granites, northern Nigeria. Econ. Geol. 75 (1), 71–82.

Omada, J.I., 2000. Hydrothermal alterations associated with Molybdenite mineralization in the Kigom Younger Granites Complex, Nigeria. Global J. Pure Appl. Sci. 6 (4), 675–684.

Omada, J., Martins, R., Abaa, S., 2003. The Kigom Peralkaline Granite Pluton of the Nigerian Younger Granite Suite. Glob. J. Geol. Sci. 1 (1), 1–12.

Pearce, J.A., Harris, N.B., Tindle, A.G., 1984. Trace element discrimination diagrams for the tectonic interpretation of granitic rocks. J. Petrol. 25 (4), 956–983.

Peccerillo, A., Barberio, M.R., Yirgu, G., Ayalew, D., Barbieri, M., Wu, T.W., 2003. Relationships between mafic and peralkaline silicic magmatism in continental rift settings: a petrological, geochemical and isotopic study of the Gedemsa volcano, Central Ethiopian Rift. J. Petrol. 44 (11), 2003–2032.

Pfänder, J.A., Münker, C., Stracke, A., Mezger, K., 2007. Nb/Ta and Zr/Hf in ocean island basalts—implications for crust–mantle differentiation and the fate of Niobium. Earth Planet. Sci. Lett. 254 (1–2), 158–172.

Poitrasson, F., Chenery, S., Bland, D.J., 1996. Contrasted monazite hydrothermal alteration mechanisms and their geochemical implications. Earth Planet. Sci. Lett. 145, 79–96.

Rahaman, M.A., Van Breemen, O., Bowden, P., Bennett, J.N., 1984. Age migrations of anorogenic ring complexes in Northern Nigeria. J. Geol. 92 (2), 173–184.

Ridolfi, F., Renzulli, A., Puerini, M., 2010. Stability and chemical equilibrium of amphibole in calc-alkaline magmas: an overview, new thermobarometric formulations and application to subduction-related volcanoes. Contrib. Miner. Petrol. 160, 45–66.

Rogers, N., 2015. The composition and origin of magmas. In: The Encyclopedia of Volcanoes. Academic Press, pp. 93–112.

Romano, P., Andújar, J., Scaillet, B., Romengo, N., Di Carlo, I., Rotolo, S.G., 2018. Phase equilibria of Pantelleria trachytes (Italy): constraints on pre-eruptive conditions and on the metaluminous to peralkaline transition in silicic magmas. J. Petrol. 59(3), 559–588. Rudnick, R.L., Gao, S., 2003. The Composition of the Continental Crust. In: Holland, H.D. and Turekian, K.K., Eds., Treatise on Geochemistry, Vol. 3, The Crust, Elsevier-Pergamon, Oxford, 1–64.

Salvi, S., Williams-Jones, A.E., 1990. The role of hydrothermal processes in the granite-hosted Zr, Y, REE deposit at Strange Lake, Quebec/Labrador: evidence from fluid inclusions. Geochim. Cosmochim. Acta 54 (9), 2403–2418.

Salvi, S., & Williams-Jones, A.E., 2005. Alkaline granite-syenite deposits, in Linnen, R.L., and Samson, I.M., eds., Rare-Element Geochemistry and Mineral Deposits: Geological Association of Canada, GAC Short Course Notes 17, 315–341.

Scaillet, B., Macdonald, R.A.Y., 2003. Experimental constraints on the relationships between peralkaline rhyolites of the Kenya Rift Valley. J. Petrol. 44 (10), 1867–1894.

Scaillet, B., Macdonald, R., 2004. Fluorite stability in silicic magmas. Contrib. Miner. Petrol. 147 (3), 319–329.

Schmidt, M.W., 1992. Amphibole composition in tonalite as a function of pressure: an experimental calibration of the Al-in-hornblende barometer. Contrib. Miner. Petrol. 110 (2), 304–310.

Schönenberger, J., Marks, M., Wagner, T., Markl, G., 2006. Fluid–rock interaction in autoliths of agpaitic nepheline syenites in the Ilímaussaq intrusion, South Greenland. Lithos 91 (1–4), 331–351.

Shapovalov, Y.B., Chevychelov, V.Y., Korzhinskaya, V.S., Kotova, N.P., Redkin, A.F., Konyshev, A.A., 2019. Physical and chemical parameters of processes producing rare-metal deposits in granitoid systems with fluorine: experimental data. Petrology 27 (6), 567–584.

Shellnutt, J.G., 2014. The Emeishan large igneous province: a synthesis. Geosci. Front. 5 (3), 369–394.

Shellnutt, J.G., Wang, C.Y., Zhou, M.F., Yang, Y., 2009. Zircon Lu–Hf isotopic compositions of metaluminous and peralkaline A-type granitic plutons of the Emeishan large igneous province (SW China): constraints on the mantle source. J. Asian Earth Sci. 35 (1), 45–55.

Shuai, X., Li, S.M., Zhu, D.C., Wang, Q., Zhang, L.L., Zhao, Z., 2021. Tetrad effect of rare earth elements caused by fractional crystallization in high-silica granites: an example from central Tibet. Lithos 384, 105968.

Siegel, K., Williams-Jones, A.E., Stevenson, R., 2017. A Nd-and O-isotope study of the REE-rich peralkaline Strange Lake granite: implications for Mesoproterozoic A-type magmatism in the Core Zone (NE-Canada). Contrib. Miner. Petrol. 172 (7), 54.

Siegel, K., Vasyukova, O.V., Williams-Jones, A.E., 2018. Magmatic evolution and controls on rare metal-enrichment of the Strange Lake A-type peralkaline granitic pluton, Québec-Labrador. Lithos 308, 34–52.

Smythe, D.J., Brenan, J.M., 2016. Magmatic oxygen fugacity estimated using zircon-melt partitioning of cerium. Earth Planet. Sci. Lett. 453, 260–266.

Sparks, R.S.J., 1986. The role of crustal contamination in magma evolution through geological time. Earth Planet. Sci. Lett. 78 (2–3), 211–223.

Su, Z.K., Zhao, X.F., Wang, C.Y., Zhu, Z.M., Song, W.L., Spandler, C., 2023. Survival of whole-rock Sm–Nd isotope system from REE redistribution and mineral-scale isotopic resetting amid hydrothermal alteration in REE-rich Fe-Cu deposit. Geochim. Cosmochim. Acta 348, 9–26.

Sun, S.S., McDonough, W.F., 1989. Chemical and isotopic systematics of oceanic basalts: implications for mantle composition and processes. Geol. Soc. Lond. Spec. Publ. 42 (1), 313–345.

Tantoh, S.B., Lehmann, B., Suh, C.E., Ngatcha, R.B., Zhang, R., Cottle, J., Goldmann, S., 2024. Zircon and cassiterite U-Pb geochronology and petrochemical characteristics of early Tertiary tin mineralization at Mayo Darlé, Cameroon Volcanic Line. J. Geochem. Explor. 257, 107369.

Thornton, C.P., Tuttle, O.F., 1960. Chemistry of igneous rocks–[Part] 1. Differentiation Index. Am. J. Sci. 258 (9), 664–684.

Tu, C., Gao, X.Y., Chen, X.Q., Safonov, O.G., 2025. Stable strontium isotopes reveal magma-fluid interaction during the evolution of granitic magma. Geochem. Perspect. Lett. 36, 54–60.

Turekian, K.K., Wedepohl, K.H., 1961. Distribution of the elements in some major units of the earth's crust. Geol. Soc. Am. Bull. 72 (2), 175–192.

Turner, D.C., 1968. Volcanic and intrusive structures in the Kila-Warji ring-complex, northern Nigeria. Quart. J. Geol. Soc. London 124 (1–4), 81–89.

Van Breemen, O., Hutchinson, J., Bowden, P., 1975. Age and origin of the Nigerian Mesozoic granites: a Rb-Sr isotopic study. Contrib. Miner. Petrol. 50, 157–172.

Vasyukova, O., Williams-Jones, A.E., 2020. Partial melting, fractional crystallisation, liquid immiscibility and hydrothermal mobilisation–a ‘recipe’ for the formation of economic A-type granite-hosted HFSE deposits. Lithos 356, 105300.

Veevers, J.J., 2003. Pan-african is Pan-Gondwanaland: oblique convergence drives rotation during 650–500 Ma assembly. Geology 31 (6), 501–504.

Vincent, V.I., Wang, L.X., Kamaunji, V.D., Zhu, Y.X., Cao, L., 2022a. New geochronological and geochemical constraints on the Banke, Dutsen Wai, Guraka, and Zuku alkaline granite complexes from the northcentral Nigerian younger granite province. Int. Geol. Rev. 65, 416–441.

Vincent, V.I., Wang, L.X., Zhu, Y.X., Kamaunji, V.D., Ahmed, H.A., Ntekim, E.E., Cao, L., 2022b. Onset of the anorogenic alkaline magmatism in the Nigerian Younger Granite province: Constraints from the Daura and Dutse complexes. Lithos 410, 106561.

Vonopartis, L.C., Kinnaird, J.A., Nex, P.A., Robb, L.J., 2021. African A-Type granites: a geochemical review on metallogenic potential. Lithos 396, 106229.

Vonopartis, L., Nex, P., Kinnaird, J., Robb, L., 2020. Evaluating the changes from endogranitic magmatic to magmatic-hydrothermal mineralization: the Zaaiplaats tin granites, Bushveld Igneous Complex, South Africa. Minerals 10 (4), 379.

Walraven, F., Strydom, J.H., Strydom, N., 1990. Rb-Sr open system behaviour and its application as a pathfinder for Sn mineralisation in granites of the Bushveld complex, South Africa. J. Geochem. Explor. 37, 333–350.

Weis, D., Liégeois, J.P., Javoy, M., 1986. The Timedjealen alkaline ring-complex and related N/1bS dyke swarms (Adrar des Iforas, Mali)—A Pb/1bSr/1bO isotopic study. Chem. Geol. 57 (1–2), 201–215.

Whalen, J.B., Currie, K.L., Chappell, B.W., 1987. A-type granites: geochemical characteristics, discrimination and petrogenesis. Contrib. Miner. Petrol. 95, 407–419.

Whalen, J.B., Hildebrand, R.S., 2019. Trace element discrimination of arc, slab failure, and A-type granitic rocks. Lithos 348, 105179.

Williams-Jones, A.E., Vasyukova, O.V., 2023. Niobium, critical metal, and progeny of the mantle. Econ. Geol. 118 (4), 837–855.

Wright, J.B., 1973. Continental drift, magmatic provinces and mantle plumes. Nature 244 (5418), 565–567.

Yin, R., Huang, X.L., Wang, R.C., Sun, X.M., Tang, Y., Wang, Y., Xu, Y.G., 2022. Rare-metal enrichment and Nb–Ta fractionation during magmatic–hydrothermal processes in rare-metal granites: evidence from zoned micas from the Yashan pluton, South China. J. Petrol. 63 (10), egac093.

Zaraisky, G.P., Aksyuk, A.M., Devyatova, V.N., Udoratina, O.V., Chevychelov, V.Y., 2009. The Zr/Hf ratio as a fractionation indicator of rare-metal granites. Petrology 17, 25–45.

Zen, E.A., 1986. Aluminum enrichment in silicate melts by fractional crystallization: some mineralogic and petrographic constraints. J. Petrol. 27 (5), 1095–1117.

Zhang, J., Wang, T., Castro, A., Zhang, L., Shi, X., Tong, Y., Zhang, Z., Guo, L., Yang, Q., Laccheri, M.L., 2016. Multiple mixing and hybridization from magma source to final emplacement in the Permian Yamatu pluton, the Northern Alxa Block, China. J. Petrol. 57 (5), 933–980.

Zhao, H., Romer, R.L., Zhao, P., Liu, M., Wang, X., Yuan, S., 2025. Role of mantle material in the formation of Sn mineralization–Noble gas constraints from the giant Jiepailing Sn-Be-F deposit, Nanling region, South China. Ore Geol Rev, 106539.

Zhu, Y., Wang, L., Pan, Y., Zhang, C., Almeev, R.R., She, Z., Holtz, F., 2024. Pyrochlore composition and SmNd isotope signature as indicators of magmatic-hydrothermal processes: the case of Ririwai complex, north-Central Nigeria. Chem. Geol. 652, 122021.

Zindler, A., Hart, S., 1986. Chemical Geodynamics. Annu. Rev. Earth Planet. Sci. 14, 493–571.

Zozulya, D., Macdonald, R., Bagiński, B., Jokubauskas, P., 2022. Nb/Ta, Zr/Hf and REE fractionation in exotic pegmatite from the Keivy province, NW Russia, with implications for rare-metal mineralization in alkali feldspar granite systems. Ore Geol. Rev. 143, 104779.